TAMPEREEN TEKNILLINEN YLIOPISTO
TAMPERE UNIVERSITY OF TECHNOLOGY

Venla Manninen

Molecular Modifications of Active and Anode Buffer Layers of Bulk Heterojunction Solar Cell

Julkaisu 1214 • Publication 1214

Tampere 2014

Tampereen teknillinen yliopisto. Julkaisu 1214
Tampere University of Technology. Publication 1214

Venla Manninen

Molecular Modifications of Active and Anode Buffer Layers of Bulk Heterojunction Solar Cell

Thesis for the degree of Doctor of Science in Technology to be presented with due permission for public examination and criticism in Festia Building, Auditorium Pieni Sali 1, at Tampere University of Technology, on the 23rd of May 2014, at 12 noon.

Tampereen teknillinen yliopisto - Tampere University of Technology
Tampere 2014

ISBN 978-952-15-3293-1 (printed)
ISBN 978-952-15-3299-3 (PDF)
ISSN 1459-2045

Abstract

In this work, new photoactive materials were tested in the active and anode buffer layers of the inverted ITO|ZnO|donor:$PC_{60/70}BM$|Buffer|Au/Ag organic bulk heterojunction (BHJ) solar cell. The molecular properties of the materials synthesized for this work were designed in order to improve the efficiency of the inverted solar cell structure. In addition to testing the materials in the cells, their effect on the cell function was investigated. The work aimed to understand the effects of the studied buffer and active layer materials in the cell function and photovoltaic performance.

Organometallic n-type tris-(8-hydroxyquinoline)aluminum (Alq_3) derivatives, p-type aryl end-capped quaterthiophenes, and a combined p- and n-type Alq_3 end-capped hexathiophene were tested as hole transporting anode buffer layer materials. As the various different materials provided a diverse buffer material selection, the properties of the materials for improved cell function were investigated by spectroscopic, electrochemical, computational and thermoanalytical methods.

The studied Alq_3 derivatives have electron donating amino substituents, either piperidine, pyrrolidine or morpholine rings, on the 5-position of the 8-hydroxyquinoline ligands, which ease the oxidation of the complexes and elevate the highest occupied molecular orbital (HOMO) energy levels. The higher HOMO levels of the derivatives, compared to that of Alq_3, reduce the hole extraction barrier in the cell. Therefore, the cells with the derivatives as buffer layers had a higher short circuit current (I_{sc}) compared to that with Alq_3. Simultaneously, due to higher hole injection barrier, the cells with the derivatives as buffer layers had lower open circuit voltage (V_{oc}) than the cell with Alq_3. The derivative with the morpholine ring has ideal energy levels with respect to the created energy barriers. Thus, the cell with the morpholine derivative as buffer layer performed better than the cell with Alq_3.

The quaterthiophenes studied in this work have cyanophenyl or methoxyphenyl end-groups and methyl or hexyl side chains attached to the thiophene backbone. These structural differences affect their electronic distribution, absorption profile, energy levels and molecular packing, especially in the solid state. The use of *p*-cyano end-capped quaterthiophene with hexyl side chains as an anode buffer layer resulted in a better cell power conversion efficiency compared to that with Alq_3. The use of the Alq_3 end-capped hexathiophene as an anode buffer layer decreased the cell serial resistance (R_s) and increased I_{sc}. Photoinduced reactions, such as energy or electron transfer, between the Alq_3 or aryl end-capped oligothiophene buffer materials and photoactive layer partly explain the improved I_{sc}.

A synthesized benzodithiophene-benzotriazole donor-acceptor (D-A) copolymer was compared as donor material with three previously studied fluorine-benzotriazole D-A copolymers. The relation between donor polymer structural properties and photovoltaic performance was studied by combining computational and experimental methods. The cell with the benzodithiophene-benzotriazole copolymer as donor material had better efficiency than the cells with the fluorine-benzotriazole copolymers. Calculations on the molecular geometry, energy levels, molecular orbitals, and lowest energy excitations provided an additional perspective to understand the polymer's function as donor material. Based on the calculations, the benzodithiophene-benzotriazole copolymer had a more planar backbone, continuous LUMO electron density, longer

conjugation and better exciton and charge transport properties compared to those of the fluorine-benzotriazole copolymers. Bulky side groups in the fluorine-benzotriazole copolymers caused steric hindrance and twisting or bending of the backbone. As a result, the electron density concentrates in parts of the polymer structure and π-conjugation weakens or is broken. As the delocalization does not cover the whole polymer structure, excitons or charges are trapped in the gaps of the discontinuous molecular orbitals.

Alq_3, aryl and 8-phenoxyquinoline end-capped oligothiophenes were used as dopant materials in the P3HT:$PC_{60}BM$ BHJ photoactive layer. In the ternary blend of the dopant, P3HT and $PC_{60}BM$ molecules, intermolecular interactions are likely as the molecules are in close proximity in the solid photoactive layer. The effect of dopant molecules on the cell function was studied by solar cell experiments. To investigate the intermolecular interaction of the dopant molecules with the active layer components, P3HT donor and $PC_{60}BM$ acceptor, steady state and time resolved spectroscopic measurements were carried out in chloroform solutions. Based on the measurements, Alq_3 end-capped hexathiophene donates an electron to $PC_{60}BM$. Photoinduced energy transfer was observed between the cyanophenyl end-capped quaterthiophene and $PC_{60}BM$.

The cell absorption increases with doping. Thus, dopant molecules function as additional light absorbers in the photoactive layer. After excitation, the dopant molecules transfer electrons or energy to $PC_{60}BM$, which increases the cell I_{sc} and power conversion efficiency. When a cyanophenyl end-capped oligothiophene with diketopyrrolopyrrole (DPP) core was used as dopant, the cell emission decreased. DPP-group inclusion broadens the dopant absorption to the near IR-region. Therefore, the absorption of the dopant overlaps with P3HT emission and the dopant molecules can reabsorb the light emitted by P3HT. In this case, the cell I_{sc} and power conversion efficiency increased further.

Preface

Most of all, I want to express my deepest gratitude to my supervisor, Prof. Helge Lemmetyinen, for giving me the opportunity to join and work in the Supramolecular Photochemistry Group. I especially appreciate his will and belief in my advance as researcher from my starting point. Thanks to his international connections and cooperation, colleagues from different countries and several visits abroad have extended my perspectives in science and life. Without Helge´s support, especially in the latest time of the work, the thesis would not be completed in this time.

I am greatly thankful for Dr. Juha Heiskanen for the fruitful collaboration and synthetic efforts. His experience in photoactive material synthesis and will to synthesize new organic molecules for solar cell materials, was a prerequisite for this thesis. Also, his enthusiasm in research and belief in the results motivated me greatly.

I want thank my office-mate, Dr. Paola Vivo, for teaching me the organic solar cell preparation and sharing the office and thoughts. Thanks go to Dr. Antti Tolkki for his help and profound instruction, when I started my work in the group. I am grateful to Prof. Nikolai Tkachenko, Dr. Vladimir Chukharev and Dr. Kimmo Kaunisto for their theoretical and practical advices related to optical spectroscopy. I greatly appreciate the work of lecturers, Raija Mikkonen, Marja Asp-Lehtinen, Terttu Hukka, Elina Vuorimaa-Laukkanen, Riikka Lahtinen and Aleksander Efimov, who inspired me to study chemistry further. I am grateful to Dr. Simo Ali-Löytty for his advices in the statistical analysis of the solar cell results.

For the pleasant and encouraging working atmosphere I am thankful for all the colleagues in the Chemistry Department. I am much obliged to our lunch group members for the relaxing company.

I want to dedicate my special thanks to Helena Mäkinen, who helped and encouraged me to start studying chemistry and mathematics instead of work in a restaurant. Due to her teaching I got into the university of technology and had a change to enter the academic world.

My limitless source of energy has been dancing between the work days. My ballet teacher, Elwa Molin, taught me to never give up and learn today, not tomorrow.

I am truly grateful to my parents, Raija and Rauno, sister, Elina, and brother, Ossi, for always supporting me. My warmest thanks go to Pasi for sharing the love and life.

This work was carried out at the Department of Chemistry and Bioengineering, Tampere University of Technology between September 2011 and March 2014. The National Graduate School of Nanoscience (NGS-NANO) is gratefully acknowledged for funding.

Tampere, March 2014

Venla Manninen

List of publications

The thesis is based on the work contained in the following publications, which will hereafter be referred by their Roman numerals:

I **Synthesis and characterization of tris-(5-amino-8-hydroxyquinoline)aluminum complexes and their use as anode buffer layers in inverted organic solar cells**

Venla M. Manninen, Walaa A. E. Omar, Juha P. Heiskanen, Helge J. Lemmetyinen and Osmo E. O. Hormi

J. Mater. Chem. **2012**, 22, 22971–22982.

II **Conjugated donor-acceptor (D-A) copolymers in inverted organic solar cells – a combined experimental and modelling study**

Venla Manninen, Mika Niskanen, Terttu I. Hukka, Felix Pasker, Simon Claus, Sigurd Höger, Jinseok Baek, Tomokazu Umeyama, Hiroshi Imahori and Helge Lemmetyinen

J. Mater. Chem. A, **2013**, 1, 7451–7462.

III **Spectroscopic study of a synthesized Alq_3 end-capped oligothiophene applied in organic solar cells**

Venla M. Manninen, Juha P. Heiskanen, Kimmo M. Kaunisto, Osmo E. O. Hormi and Helge J. Lemmetyinen

RSC Adv. **2014**, 4, 8846–8855.

IV **Synthesis of Aryl End-Capped Quaterthiophenes Applied as Anode Interfacial Layers in Inverted Organic Solar Cells**

Juha P. Heiskanen, Venla M. Manninen, Dmitri Pankov, Walaa A. E. Omar, Tuuva Kastinen, Terttu I. Hukka, Helge J. Lemmetyinen and Osmo E. O. Hormi

Submitted to *ACS Appl. Mater. Interfaces*

V **The effect of diketopyrrolopyrrole (DPP) group inclusion in *p*-cyanophenyl end-capped oligothiophene used as dopant in P3HT:PCBM BHJ solar cells**

Venla M. Manninen, Juha P. Heiskanen, Dmitri Pankov, Tuuva Kastinen, Terttu I. Hukka, Osmo E. O. Hormi and Helge J. Lemmetyinen

Submitted to *Photochem. Photobiol. Sci.*

Author´s contribution

Venla Manninen prepared and analyzed the solar cells, carried out the spectroscopic, electrochemical, profilometer and part of DSC measurements, wrote publications I – III and V and participated in writing publication IV.

Abbreviations and symbols

A	absorbance, absorption
Alq_3	tris-(8-hydroxyquinoline)aluminum
AM 1.5	universal air mass coefficient for solar cell characterization
BHJ	bulk heterojunction
CRU	constitutional repeating unit
CTC	charge transfer complex
D-A	donor-acceptor
DCB	1,2-dichlorobenzene
DFT	density functional theory
DPP	diketopyrrolopyrrole
DSC	differential scanning calorimetry
ΔOD	change in optical density *ie*. absorbance
EPCE	external photon to current efficiency
eV	electron volt, 1 eV = $1.60217657 \times 10^{-19}$ J
FF	fill factor
ICT	intramolecular charge transfer
ICTS	intramolecular charge transfer state
I_{sc}	short circuit current
ITO	indium tin oxide
HOMO	highest occupied molecular orbital
HTL	hole transporting layer
LBG	low band gap
LUMO	lowest unoccupied molecular orbital
OLED	organic light emitting diode
$PC_{60}BM$	[6,6]-phenyl-C_{61}-butyric acid methyl ester
$PC_{70}BM$	[6,6]-phenyl-C_{71}-butyric acid methyl ester

P3HT	poly(3-hexylthiophene)
R_s	serial resistance
R_{sh}	shunt resistance
s	sample standard deviation
TCSPC	time correlated single photon counting
V_{oc}	open circuit voltage
ZnO	zinc oxide
α	absorption coefficient
Φ_{PL}	fluorescence emission quantum yield
λ	wavelength
η	power conversion efficiency
τ	lifetime

Contents

1 Introduction

Humans have changed Earth's atmosphere in dramatic ways over the past two centuries. The burning of fossil fuels, coal, oil, and gasoline, has increased the concentration of greenhouse gases in the atmosphere, especially CO_2. Greenhouse gases act like a blanket, absorbing IR-radiation and preventing it from escaping into outer space. The net effect is the gradual heating of Earth's atmosphere and surface, a process known as global warming. If global warming continues, it will cause significant climate change, a rise in sea levels, increasing ocean acidification, extreme weather events and other severe natural and societal impacts.

In 2012, the total world energy consumption was 125×10^8 tonnes oil equivalent (toe), which corresponds to 17 terawatts (TW) average power. The year 2012 saw a slowdown in the growth of energy consumption globally, partly as a result of the economic downturn, but also because individuals and businesses have responded to high prices by becoming more efficient in their use of energy. At the same time, the supply of energy is coming from an increasing diversity of sources as the world's energy market continues to adapt, innovate and evolve. By 2035, global energy consumption is expected to increase by 41% relative to the current level, which equals to a 24 TW consumption. Our mission is to find and produce forms of energy needed to meet the growing demand of energy safely and sustainably.[1]

Sunlight provides the largest carbon neutral energy source. In one hour the Sun shines on Earth the energy needed for the annual worldwide consumption.[2] 31 gigawatts (GW) of solar photovoltaics (PV) were installed worldwide in 2012, which was an all-time annual record that raised the global PV capacity above 100 GW. PV technologies have grown rapidly during the last decade. In 2006, only a handful of countries could provide solar capacity of 100 megawatts or more. Now 30 countries are on that list, which will be doubled by 2018. [3]

A great challenge and motivation in energy research is to exploit the inexhaustible solar energy more efficiently for human benefit. As an alternative for the robust silicon solar cells, organic solar cells have evolved as low-cost, easy-production and sustainable solar cell technology. Large-area and flexible organic cells can be fabricated by fast roll-to-roll production. Generally, in the bulk heterojunction (BHJ) structure, p-type organic semiconducting polymers function as electron donors and fullerene derivatives are used as acceptor materials. Significant improvements in the power conversion efficiency of the organic cells, up to 12 %[4], have been achieved by designing effective photoactive materials, device architectures, and processing techniques.

In addition to the conjugated polymers, small molecule donor materials have been investigated in organic cells.[5] Small molecule donors possess advantages over conjugated polymers such as well-defined molecular structures, precise molecular weights and high purity.[6] Recently, solution processed small molecule BHJ cells have achieved the efficiency of 9 %.[7]

In this work, new photoactive materials were tested the inverted organic ITO|ZnO|donor:$PC_{60/70}BM$|Alq_3|Au/Ag BHJ solar cell structure. The molecular properties of the materials synthesized for this work were designed in order to improve the efficiency of the inverted solar cell structure. In addition to testing the materials in the cells, their effect on the cell function

was investigated. Electrochemical, spectroscopic, thermal, and computational methods were applied to analyze the function of the prepared solar cells, properties of the used materials and possible photoinduced intra- and intermolecular interactions. The work aimed to understand the effects of the studied buffer and active layer materials in the cell function and photovoltaic performance.

First, organometallic Alq_3 derivatives and Alq_3 and aryl end-capped oligothiophenes were applied as small molecule hole transporting anode buffer layer materials.[I,III,IV] The properties of the materials to improve the cell efficiency, when used as an interfacial layer between the P3HT:PC_{60}BM photoactive layer and metal anode, were investigated. The relation between conjugated benzodithiophene/fluorine-benzotriazole donor-acceptor copolymers structural properties and photovoltaic performance was studied by combining computational and experimental methods.[II] Calculations on the molecular geometries, energy levels, molecular orbitals, and lowest energy excitations provided an additional perspective to understand the polymers' function as donor materials. Finally, Alq_3, aryl and 8-phenoxyquinoline end-capped oligothiophenes were used as additional light-absorbing dopant materials in the P3HT:PC_{60}BM BHJ photoactive layer.[III,V] In the ternary blend of the dopant, P3HT and PC_{60}BM molecules, intermolecular interactions become possible. Photoinduced intra- and intermolecular interactions of the dopant molecules with P3HT and PC_{60}BM were studied in chloroform by spectroscopic methods.

2 Background

This chapter first introduces the structure and function principles of the inverted organic solar cell configuration used in this work. After that the photovoltaic parameters and cell efficiency analysis are presented. Comparison of the organic cells is based on the cell power conversion efficiency and the photovoltaic parameters. In this work, standard deviations of the measured photovoltaic parameters are presented to demonstrate their variation. At the end of this chapter, the typical variation of the parameters between the solar cell samples is shown by an example table.

2.1 Structure of the inverted organic solar cell

Organic solar cells studied in this work were built on glass substrates covered with a patterned conducting indium tin oxide (ITO) layer. A schematic structure and energy levels of the cell configuration are shown in Figure 2.1. A zinc oxide (ZnO) interlayer between ITO and the photoactive layer efficiently collects electrons from the photoactive P3HT:PC_{60}BM bulk heterojunction (BHJ) photoactive layer to the ITO direction. This provides an inverted cell[8] *i.e.* electrons flow to the direction of the ITO cathode and holes to the metal anode. Inverted organic solar cell structure is air-stable due to the high stability of the ZnO layer and Au anode. The cells can be prepared and measured in ambient air without encapsulation. In addition to Au, Ag was also used as metal anode material.[IV,V] The work function of pure Ag, 4.3 eV, is changed in air as Ag is oxidized and the work function of the formed silver oxide (AgO) is close to 5.0 eV.[8] Therefore, both Au and Ag are applicable as stable anode materials in the inverted cell structure.

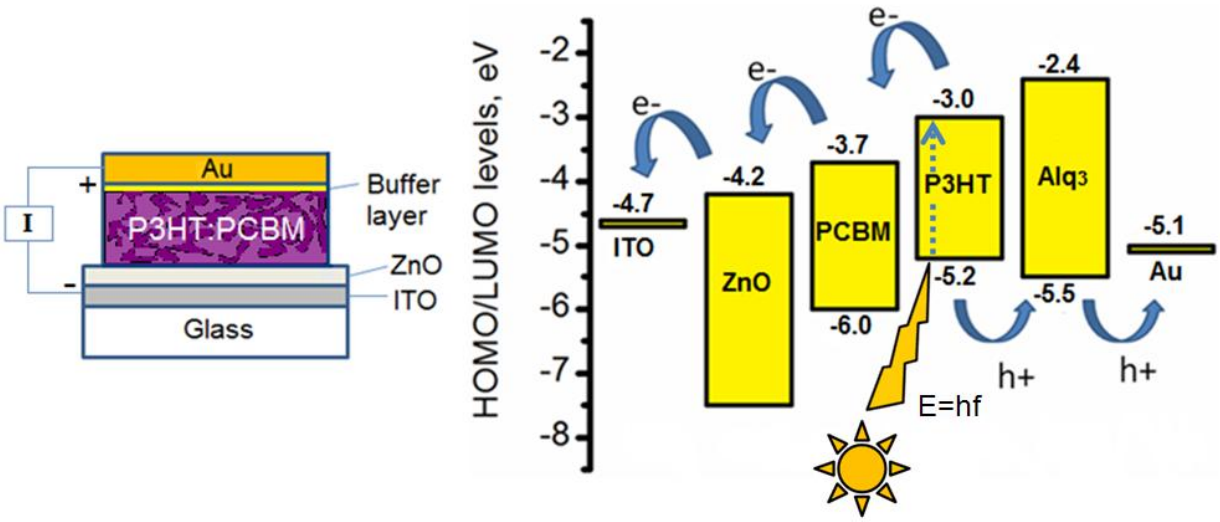

Figure 2.1 Schematic structure and energy levels[9] of the inverted organic solar cell.

2.2 Function principles of the inverted organic solar cell

The function of organic solar cells is based on the photovoltaic effect. The solar cells are illuminated through the glass substrate in a solar simulator. The solar simulator light is produced by Xe-lamp, which provides a spectrum very close to that of sunlight. The illuminated light passes through the transparent glass, ITO and ZnO layers and is absorbed by the *ca.* 100 nm thick P3HT:PC_{60}BM BHJ photoactive layer.

The BHJ photoactive layer has a heterogeneous structure of donor and acceptor molecules (Figure 2.2), which provides a large interfacial area between donor and acceptor phases. As the energy of the light is absorbed, thiophene units in the donor polymer, P3HT, are excited and electrons shift from the highest occupied molecular orbital (HOMO) to the lowest unoccupied molecular orbital (LUMO) (Figure 2.1). A positive charge remains in HOMO and together with the negative electron in LUMO they form an exciton. It is a bound state of the electron and the hole, which are attracted to each other by the electrostatic Coulombic force. Excitons are free to move in the semiconducting P3HT as long as they exist. If the exciton reaches the interface of the donor and acceptor materials during its lifetime, the positive and negative charges are separated (Figure 2.2). The hole stays in P3HT and starts to diffuse in the polymer phase. Since the holes are constantly extracted to the external circuit at the metal electrode, they start to diffuse towards the metal electrode, where their concentration is lower. Likewise, electrons are donated from the P3HT LUMO to $PC_{60}BM$ acceptor LUMO and diffuse in $PC_{60}BM$ phase to ITO. When the cell is connected to an external circuit, electric current is produced under illumination.

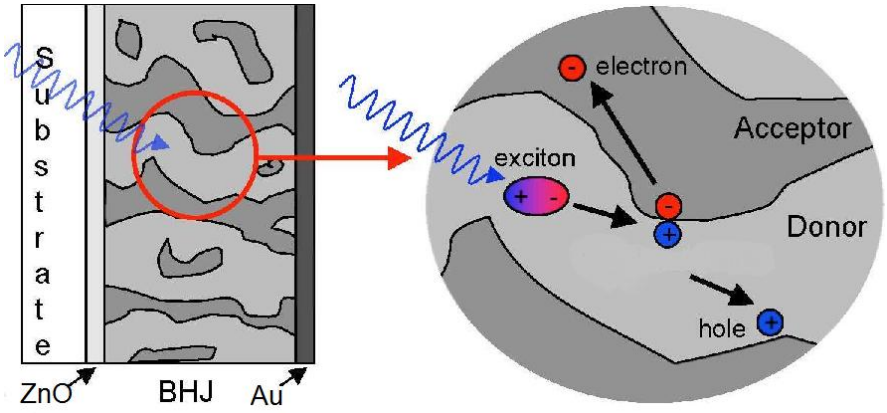

Figure 2.2 Exciton dissociation and charge separation in the inverted organic solar cell BHJ layer.[10]

Light absorption does not always lead to production of electric current due to several loss mechanisms in the cells. Excitons created beyond the diffusion length from the donor-acceptor interface recombine before reaching the interface and their energy is emitted as photons. Therefore, the lifetime (τ) of the excited state restricts partly the diffusion length of the exciton. As excitons move along the polymer backbone, conjugation length in the backbone and exciton hopping between the polymer chains also affect the diffusion. If the conjugation is broken, excitons can be trapped, and they recombine back to the ground state. If the exciton reaches the donor-acceptor interface, the Coulombic binding energy has to be overcome through the differences in the chemical potentials of the donor and acceptor materials to separate the hole and electron. Also, migration of the separated charges to the electrodes is highly dependent on the morphology of the interpenetrating network of donor and acceptor phases in the BHJ layer. Finally, charges should be transferred efficiently through the buffer layers and collected at the electrodes.

2.3 Photovoltaic parameters and cell efficiency analysis

Efficiencies of organic solar cells were measured under simulated global (G) sunlight illumination with an air mass coefficient (AM) 1.5. The solar spectrum at top of the atmosphere and an AM 1.5 G spectrum are shown in Figure 2.3. The air mass coefficient defines the direct optical path length

through the Earth's atmosphere, expressed as a ratio relative to the path length vertically upwards, *i.e.* at the zenith. The air mass coefficient is used to characterize the solar spectrum after solar radiation has traveled through the atmosphere. The air mass coefficient 1.5 is commonly used to characterize the performance of solar cells under standardized conditions.

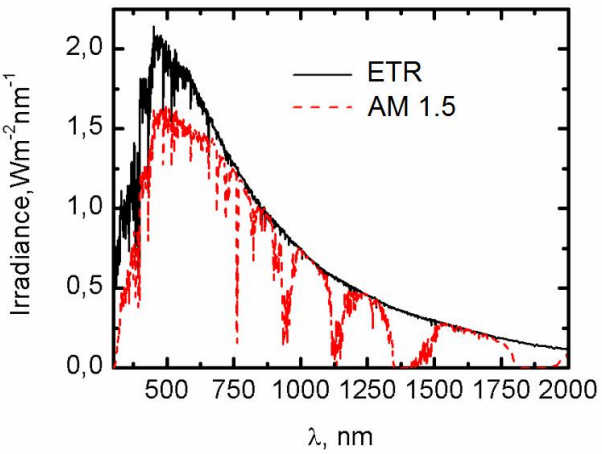

Figure 2.3 Extraterrestial radiation (ETR) = solar spectrum at top of the atmosphere, AM 1.5 = Solar spectral global irradiance at air mass 1.5 for a 37° tilted surface.[11]

The photovoltaic parameters are obtained and calculated from a current-voltage (*I-V*) curve, which presents the current produced by the cell as a function of a voltage applied to the cell. *I-V* curves of the inverted ITO|ZnO|P3HT:$PC_{60}BM$|Alq_3|Ag cell in the dark (dashed red curve) and under illumination (solid black curve) are shown together with photovoltaic parameters in Figure 2.4a.

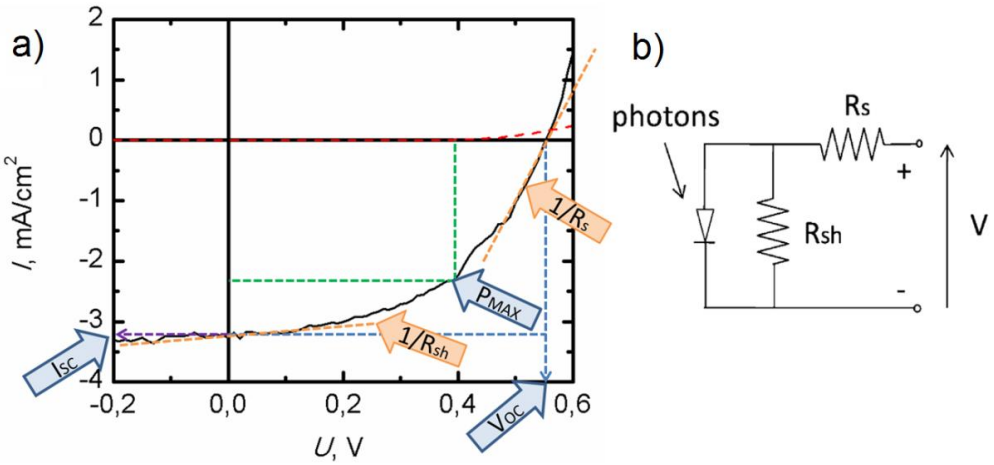

Figure 2.4 *I-V* curves of the inverted ITO|ZnO|P3HT:$PC_{60}BM$|Alq_3|Ag cell in the dark (dashed red) and under illumination (black solid) with photovoltaic parameters shown by the arrows (a) and electric circuit of the cell[12] (b).

Short circuit current (I_{sc}) is the cell current, when 0 V voltage is applied, and the cell is in short circuit conditions. Open circuit voltage (V_{oc}) is the voltage, when the cell current is 0 A, and the cell is in open circuit conditions. As shown in Figure 2.4, fill factor (*FF*) is the ratio of the maximum power (P_{MAX}, green rectangle) produced by the cell and the theoretical maximum power ($V_{oc} \times I_{sc}$, blue rectangle) according to Eq. 1:

$$FF = \frac{P_{MAX}}{V_{oc} \times I_{sc}} = \frac{V_{MAX} \times I_{MAX}}{V_{oc} \times I_{sc}} . \quad (1)$$

Power conversion efficiency (η) is calculated from the photovoltaic parameters as a ratio of the maximum power produced by the cell and the illumination (lamp) power according to Eq. 2:

$$\eta = \frac{P_{MAX}}{P_{LAMP}} = \frac{FF \times V_{oc} \times I_{sc}}{E_{TOT} A} . \quad (2)$$

An external photon to current efficiency (EPCE) spectrum presents the current produced by the cell as a function of the illumination wavelength. The cell is illuminated by monochromatic light and the produced photocurrent is measured. Efficiency is calculated according to Eq. 3:

$$\Phi_{ext} = \frac{N_e}{N_{phot}^{in}} = \frac{I_{sc} / q}{P_{in}(\lambda) / E_{phot}} = \frac{I_{sc} hc}{P_{in}(\lambda) q \lambda} . \quad (3)$$

The external photon to current spectrum is an alternative way to present the cell efficiency used also in this work.[II]

Serial resistance (R_s) and shunt resistance (R_{sh}) of the cell electric circuit (Figure 2.4b) are calculated as inverse slopes of the tangential linear fits along the *I-V* curve (Figure 2.4a).[12] Defining R_s this way is an approximation, since the tangent is never vertical. Even though R_s would approach the value of zero, a slope based on the diode equation is left. R_s is the cell current limiting factor and it should be as small as possible. R_{sh} is considered as a factor that inhibits recombination, and it should be as large as possible.

2.4 Experimental variation of the photovoltaic parameters

In this work, the experimental variation of the photovoltaic parameters is presented in the tables as a sample standard deviation value (*s*) after the measured (V_{oc} and I_{sc}) and calculated (*FF* and η) values. The value of *s* is calculated according to Eq. 4:

$$s = \sqrt{\frac{\sum_{i=1}^{n} (x_i - \bar{x})^2}{n-1}} , \quad (4)$$

where x_i is the value of the measured quantity, $\bar{x}$ is the average of the measured values and *n* is the number of the measured samples.Table 2.1 shows the photovoltaic parameters and their standard deviations for the ITO|ZnO|P3HT:$PC_{60}BM$|Alq_3|Au reference cell structure. The parameters of the best measured sample are presented in the tables and *s* values are calculated from the number of samples shown in the table. Also the average efficiency of the measured samples is shown in tables.

Table 2.1 Photovoltaic parameters and their standard deviations for the reference cell structure.

Sample	Number of cells	$I_{sc,best}$ (mA/cm^2)	$V_{oc,best}$ (V)	FF_{best} (%)	η_{best} (%)	η_{avg} (%)
Reference	10	-2.62 ± 0.15	0.55 ± 0.005	60 ± 1.6	2.42 ± 0.14	2.25

The typical experimental variation in the photovoltaic parameters of the cell structure used in this work is less than 10 % of the measured values. Variation of the parameters in the buffer layer experiments is within the 10 % range. Photoactive layer modification results in larger deviations especially in the case of doping experiments. Comparison of the cells is based on all the photovoltaic parameters. The best cell efficiency and the average efficiency values are considered the most important parameters.

3 Materials and methods

This chapter briefly presents the studied materials and solar cell preparation and analysis. In addition, the optical, electrochemical, and thermal techniques used for material characterization are briefly introduced. More detailed descriptions about the experimental techniques and instrumental configurations are given in the referred publications.[I-V]

3.1 5-amino substituted tris-(8-hydroxyquinoline)aluminum (Alq_3) derivatives

Alq_3 has been studied as a light emitting and electron transporting material since Tang and VanSlyke reported for the first time on its use in organic light emitting diodes (OLEDs).[13] The molecule is an organometallic complex, which consists of three 8-hydroxyquinoline ligands coordinated to aluminum (Figure 3.1). The properties of the complex, such as solubility, fluorescence emission color, quantum yield (Φ) and HOMO and LUMO energy levels, can be modified by attaching different electron-withdrawing or -donating substituents on the 8-hydroxyquinoline ligands.[14] The highest HOMO electron density is allocated on the 5-position of the 8-hydroxyquinoline ligand.[15] Therefore specific modification of HOMO level is possible by attaching different substituents to the 5-position.

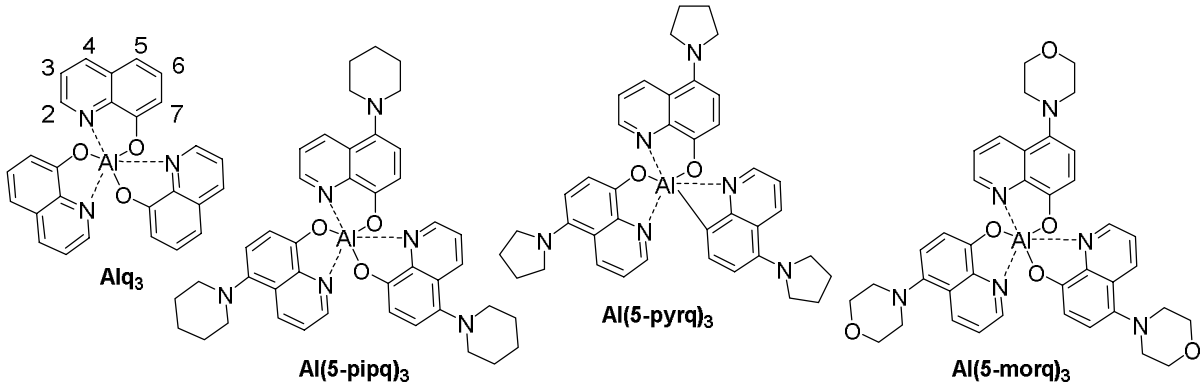

Figure 3.1 Chemical structures and abbreviations of the parent Alq_3 and its 5-amino substituted derivatives **Al(5-pipq)$_3$**, **Al(5-pyrq)$_3$** and **Al(5-morq)$_3$**. Numbering of the possible substituent positions is shown around the 8-hydroxyquinoline ligand in the parent Alq_3.

The Alq_3 derivatives studied in this work, **Al(5-pipq)$_3$**, **Al(5-pyrq)$_3$** and **Al(5-morq)$_3$**, (Figure 3.1) have electron donating[16] amino substituents, either piperidine, pyrrolidine or morpholine rings, on 5-position, which ease the oxidation of the complexes and elevate the HOMO energy levels compared to the parent Alq_3. The properties of the derivatives aimed for the reduction of the hole extraction barrier when used as anode buffer layers in the inverted organic solar cell structure. The derivatives were characterized and used as hole transporting buffer layers. Performance of the cells with the derivatives as buffer layers was compared with that of the cell with the parent Alq_3 as buffer material.[I] The compounds were synthesized at the Department of Chemistry and Bioengineering, Tampere University of Technology, in cooperation with the Department of Chemistry, University of Oulu. Alq_3 was commercially available.

3.2 Conjugated benzodithiophene/fluorine-benzotriazole donor-acceptor (D-A) copolymers

In polymer solar cells, copolymers with electron rich and electron deficient moieties alternating in the polymer backbone have performed well as electron donating materials. The redox and structural properties of the polymers are controlled by attaching different substituents to the polymer backbone, which enables tailoring of low band gap (LBG) polymers. Benzodithiophene derivatives have been used as tunable electron donors[17] and benzotriazole with various substituents as electron acceptor[18] moieties in LBG D-A copolymers. Tailored LBG copolymers based on alternating benzodithiophene and benzotriazole moieties have demonstrated excellent photovoltaic properties in inverted organic solar cells due to their intramolecular charge transfer (ICT) properties.[19]

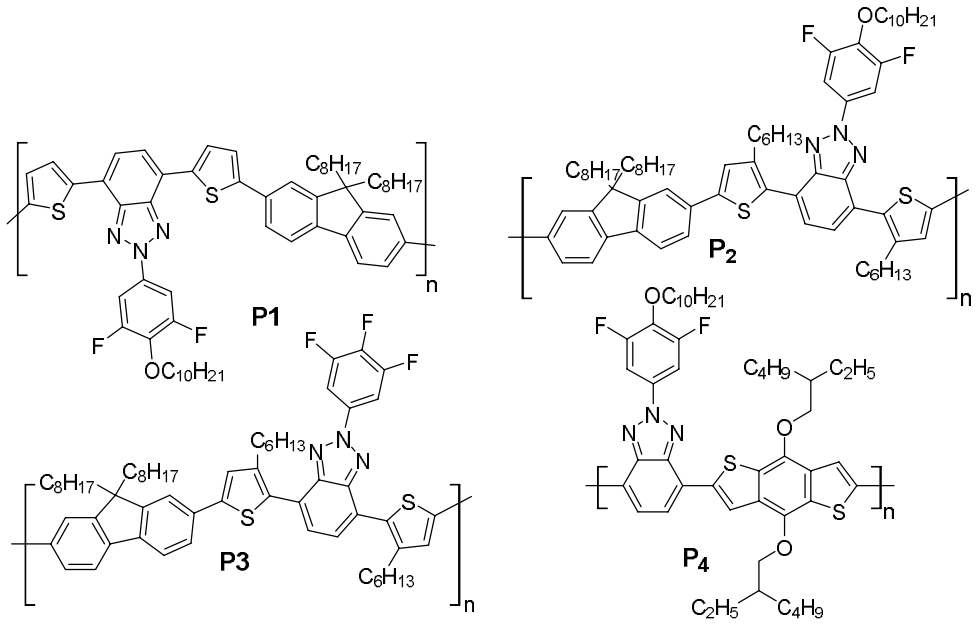

Figure 3.2 Chemical structures of the benzodithiophene/fluorine-benzotriazole D-A copolymers **P1-P4**.

Benzodithiophene-benzotriazole LBG D-A copolymer, **P4** (Figure 3.2), was synthesized for this work in order to compare its performance as a donor material in inverted organic solar cells with three previously studied fluorine-benzotriazole D-A copolymers, **P1-P3** (Figure 3.2). The experimental data was combined with computed results of the molecular geometries, energy levels, molecular orbitals and lowest energy excitations to better understand the relationship between photovoltaic performance and molecular structures.[II] The polymers were synthesized in Kekulé-Institut für Organische Chemie und Biochemie, Rheinische Friedrich-Wilhelms-Universitet Bonn.

3.3 Aryl, Alq_3, and 8-phenoxyquinoline end-capped oligothiophenes

Oligothiophenes with different substituents and end-groups have been used as hole transporting layers (HTL) in OLEDs,[20] organic light emitting transistors (OLETs),[21] organic thin film transistors (TFTs)[22], and small molecule donor materials in organic solar cells.[23]

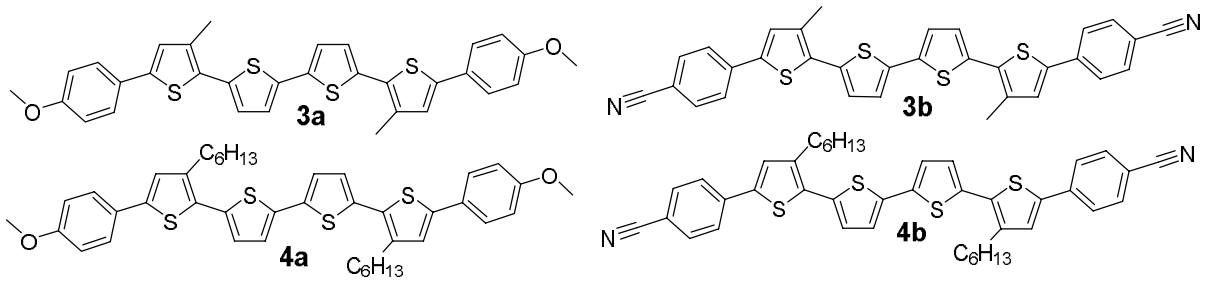

Figure 3.3 Chemical structures of the aryl end-capped quaterthiophenes **3a**, **3b**, **4a** and **4b**.

In this work, four different aryl end-capped quaterthiophenes, **3a**, **3b**, **4a** and **4b** (Figure 3.3), and an Alq_3 end-capped hexathiophene, **$(Alq_3)_2$-OT** (Figure 3.4) were used as anode buffer layers in the inverted organic solar cell structure.[III,IV] The *p*-type aryl end-capped materials, together with the *n*-type 5-amino substituted Alq_3 derivatives and combined *p*-and *n*-type **$(Alq_3)_2$-OT**, provided a diverse buffer material selection. The properties of the different buffer materials for improved cell function were investigated.

A diketopyrrolopyrrole (DPP) group was included in the center of **4b** molecular structure, which produced an aryl end-capped oligothiophene with DPP-group, **DPP-(2TPhCN)$_2$** (Figure 3.4). **4b** was compared with **DPP-(2TPhCN)$_2$** as electron donor material and additional dopant molecule blended with P3HT and $PC_{60}BM$ (Figure 3.5) in the BHJ photoactive layer of the cell.[V] The effect of DPP-group in the properties and function of the *p*-cyanophenyl end-capped oligothiophene dopant material was investigated.

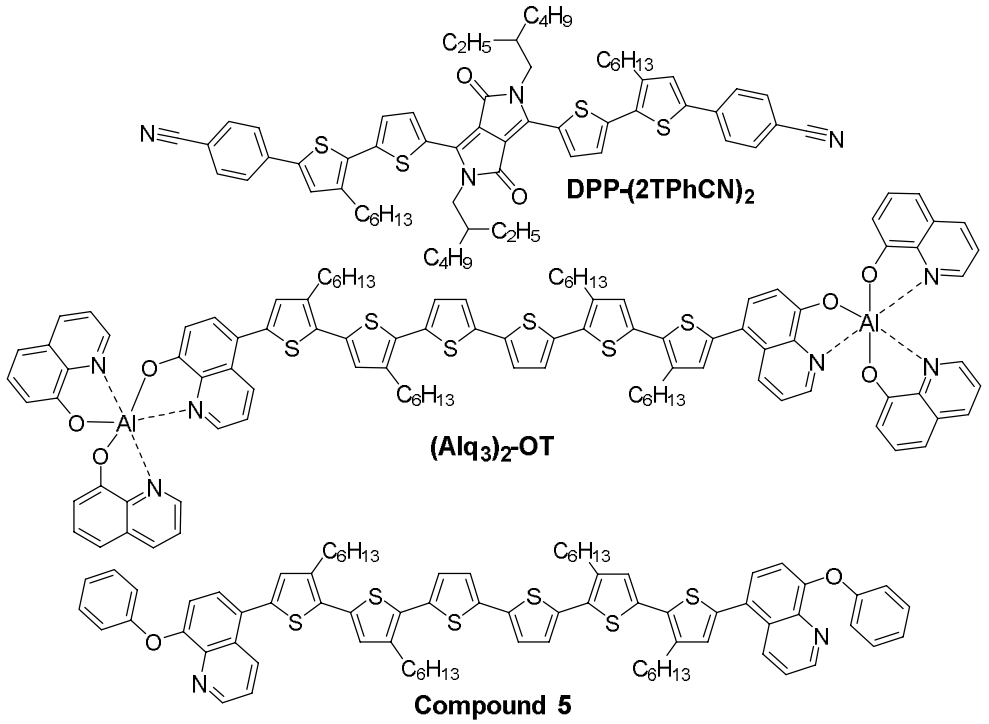

Figure 3.4 Chemical structures of the aryl end-capped oligothiophene with DPP-group (**DPP-(2TPhCN)$_2$**), Alq_3 end-capped hexathiophene (**$(Alq_3)_2$-OT**), and 8-phenoxyquinoline end-capped hexathiophene (compound **5**).

Also **$(Alq_3)_2$-OT** was used as a dopant material. 8-phenoxyquinoline end-capped hexathiophene, compound **5** (Figure 3.4), and Alq_3 (Figure 3.5) were used as reference materials in the solar cell and spectroscopic studies of **$(Alq_3)_2$-OT.** The doping experiments aimed to understand the effect of the dopant molecules in the cell function and photovoltaic performance. Spectroscopic studies on the interaction of the dopant molecules with P3HT and $PC_{60}BM$ were carried out by using steady state and time resolved spectroscopic methods. The studied oligothiophenes were synthesized in the Department of Chemistry, University of Oulu.

3.4 Photoactive layer components P3HT, $PC_{60}BM$ and $PC_{70}BM$

In the field of polymer based photovoltaic cells, poly(3-hexylthiophene) (P3HT) and [6,6]-phenyl-C_{61}-butyric acid methyl ester ($PC_{60}BM$) have been the most studied active layer materials for the bulk hetero junction (BHJ) structure.[24] Commercially available P3HT was used as primary donor polymer and fullerene derivatives $PC_{60}BM$ and $PC_{70}BM$ (Figure 3.5) as acceptor materials in this work. The selection of the acceptor material was done by testing and optimizing the cells using both acceptor materials, $PC_{60}BM$ and $PC_{70}BM$, with the used donor materials. The testing and optimization series are left out of the thesis and only the results of the best performing series are presented.

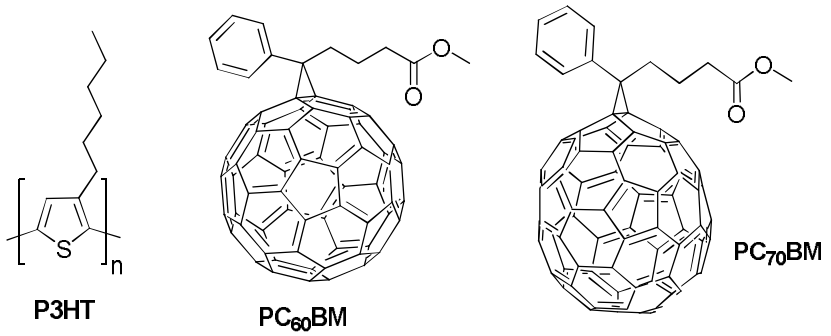

Figure 3.5 Chemical structures of the photoactive layer materials P3HT, $PC_{60}BM$ and $PC_{70}BM$.

3.5 Solar cell preparation and analysis

The studied compounds were applied as dopant molecules, donor materials, and/or buffer layers in the inverted ITO|ZnO|donor:$PC_{60/70}BM$|buffer|Au/Ag solar cells. The cells were constructed on commercial ITO covered glass substrates. The ITO layer was taped and lacquered for *aqua regia* etching to achieve a patterned ITO. The etched plates were cleaned by sonicating in acetone, chloroform, SDS solution (20 mg sodium dodecyl sulphate in 500 mL Milli-Q H_2O), Milli-Q H_2O, and 2-propanol, 30 min in each, respectively, and dried under vacuum at 150 ºC for one hour. After a 10 min N_2 plasma cleaning procedure, a 20 nm ZnO layer was deposited by 1 min spin-coating from 50 g L^{-1} zinc-acetate in 96 % 2-methoxyethanol and 4 % ethanolamine solution following the literature process.[8]

The photoactive layer compounds, P3HT, $PC_{60/70}BM$ and in the case of doped cells also the dopant molecules, were dissolved in 1,2-dichlorobenzene[I,II,IV,V] (DCB) or DCB:$CHCl_3$ (2:1 V-%) solvent mixture[III] and stirred (250 rpm) overnight at 50 ºC. Spin-coating of the BHJ photoactive layer from the P3HT:PCBM:dopant blend took from 30 s to 5 minutes (600

rpm) in the spin-coater under N_2 flow. The spin-coated films were annealed under vacuum at 110 ºC for 10 min. Buffer layer and metal anode were evaporated in the vacuum evaporator under ~ 3×10^{-6} mbar pressure. The evaporation rate and film thickness were controlled with evaporator crystals to deposit the desired thickness of the buffer and ~50 nm thick metal anode layers on top of the photoactive layer. The cells were stored in the ambient atmosphere in the dark before measurements and analysis.

The photovoltaic parameters were obtained and calculated from the *I-V* curves, which were measured under simulated AM 1.5 G sunlight illumination (50 mW cm^{-2}) using a source/monitor unit (Agilent E5272A). A voltage between -0.2 and 0.6 V was applied in 10 mV steps and the measurements were carried out in air at room temperature (20 °C) without encapsulation of the devices. The illumination was produced by filtered Xe-lamp (Oriel Corporation & Lasertek) in the solar simulator (Zuzchem LZC-SSL). The cell areas were from 1 mm^2 to 2 mm^2 measured by an optical microscope (MBS-10). The illumination power density was measured by using a power meter (Coherent Fieldmax II LM10). Because a certified measuring system could not be employed, the absolute efficiency values are not directly comparable with the other published results. However, the reported efficiencies and the relative efficiency changes are comparable within the presented devices.

3.6 Steady state absorption and fluorescence measurements

Steady state absorption measurements were used to determine the ground state absorption properties of the compounds in solutions and solid films. Absorption profiles of the compounds used as solar cell photoactive materials should match with the solar spectrum (Figure 2.3), whose maximum irradiance is between 470 nm and 750 nm, to harvest the sunlight and produce current efficiently.[II,III,V] Absorption profiles of the materials were used to determine excitation wavelengths for emission and time resolved measurements.[I-V]

Steady state fluorescence emission spectra of the pure compounds in solutions and solid samples were measured for Stokes shift calculations, material characterization and selecting the monitoring wavelengths of time resolved fluorescence measurements.[I-V] Quenching of the donor material emission as a function of acceptor concentration enabled studying intermolecular interactions and quenching dynamics in steady state.[III,V]

3.7 Time resolved fluorescence and absorption measurements

Time resolved fluorescence emission measurements were performed to calculate excited state lifetimes in nanosecond and sub-nanosecond scale for liquid and solid samples employing the time correlated single photon counting (TCSPC) method.[I-V] A decrease in the donor material lifetime as a function of the quencher concentration provided a tool to study quenching dynamics in their mixed solution.[V] Ultrafast time resolved transient absorption measurements using pump-probe set-up were carried out to study the picosecond time scale photoinduced processes, such as energy or electron transfer, in solutions. Function of dopant molecules in the solar cell photoactive layer was considered based on the photoinduced intra- or intermolecular interactions of the dopant molecules with $PC_{60}BM$.[III,V]

3.8 TCSPC

Fluorescence emission decays of the samples were measured using the TCSPC system (Figure 3.6). The excitation source generates a pulsed laser light beam, which is split into two by quartz beam splitter (M1). A part of the laser light is used to excite the sample and the other part is used for triggering, which is the “start” laser pulse in the time diagram. Emission from the excited sample is directed to a monochromator, which passes on the light of selected monitoring wavelength. Because each detected photon generates an electric pulse at the photomultiplier tube (PMT), the method is called single photon counting. The triggering light pulse generates an electric pulse at the photodiode (PD). Both the triggering pulse and pulse from PMT are directed to the constant fraction discriminators (CFD) to equalize the shape and amplitude of the pulses. In the time-to-amplitude converter (TAC) the triggering pulse starts operation of the linearly rising voltage generator and the first emitted photon detected in the PMT stops the generator (the first photon “stop”). The output voltage of the generator depends on the time delay between the “start” and “stop” pulses. Multichannel analyzer (MCA) analyzes the voltage output of the generator. The MCA memory is divided into channels that correspond to voltage intervals. The voltage from TAC increases the value of the matching channel by one. As the voltage from the TAC is proportional to the time delay, the MCA channels correspond to the time intervals and the decay profile of the sample is recorded by counting the photons arriving at each time delay after excitation.[25]

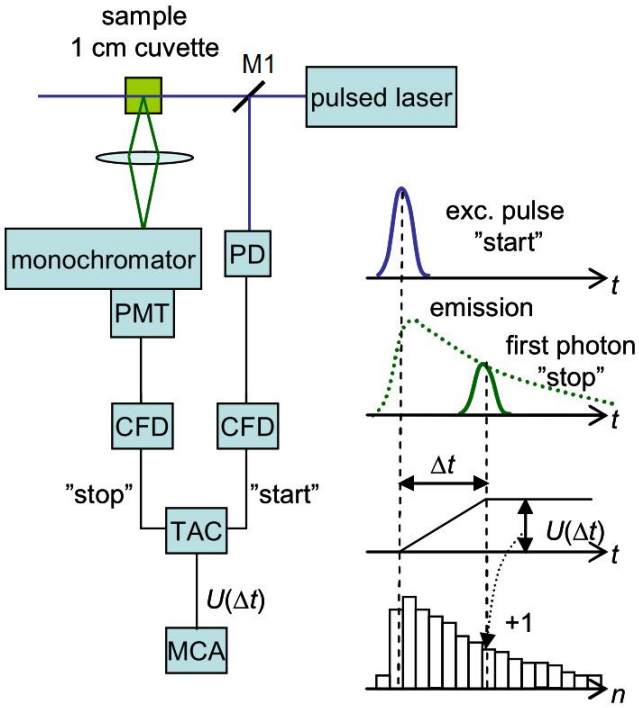

Figure 3.6 A scheme (left) and time diagram (right) of TCSPC measuring system.[26]

3.9 Pump-probe

In the transient absorption measurements, the excitation laser pulse of chosen wavelength (pump) and continuous or pulsed white light (probe) are directed through the sample to detect the absorption changes as a function of time after excitation. Two different pump-probe instruments were used to measure the picosecond time-scale transient absorption measurements. A simplified

scheme of one of the pump-probe instruments is in Figure 3.7 to exemplify the function principles of the method.

A Ti:sapphire laser generates a ~800 nm, 100 fs excitation base pulse beam, which is split in two with a semi-transparent mirror. A part of the beam is directed through a second harmonic generator (SHG) forming the pump-pulses and the other part is directed to a water cuvette, which generates a white continuum for probing the absorbance changes in a wide spectral region. The probe beam is further split into a signal beam and a reference beam, which are focused on the sample cuvette. The pump-beam is directed through a delay line with a moving right angle reflector, which is used to tune the optical path length of the pump pulse relative to the probe pulse, and focused on the signal beam in the sample cuvette. Depending on the delay line length, the pump pulse arrives at the sample at a certain time before the probe pulse and sample absorption at the known time after excitation is measured. Changes in absorption are detected from before the excitation, at negative delay times, until the upper time limit after excitation, which is dependent on the length of the delay line.[25]

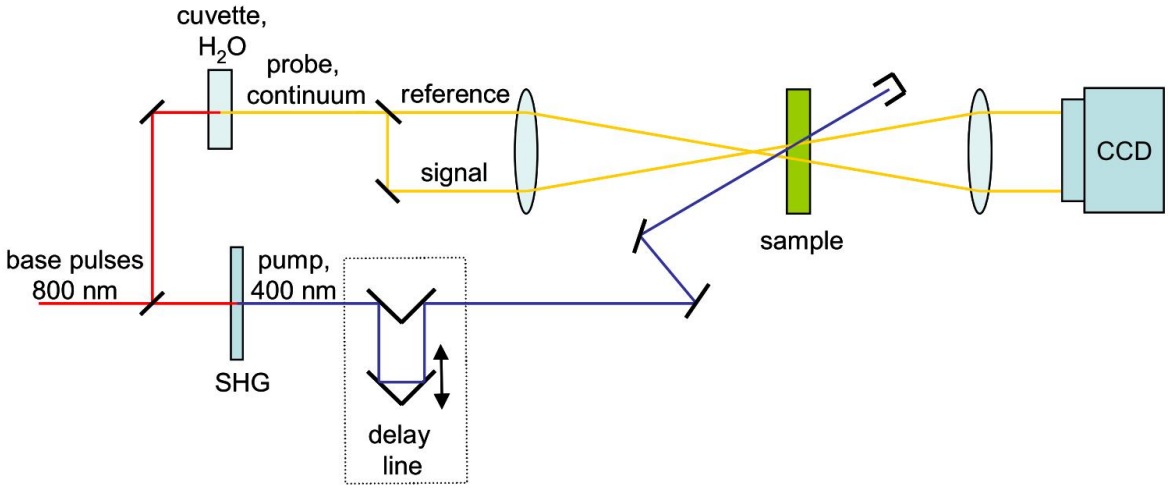

Figure 3.7 Simplified scheme of the pump-probe method.[26]

The transient species formed after the excitation of the sample are identified from the detected absorption changes. This provides direct information about the order and dynamics of the photoinduced reaction. The raw data obtained from the measurements consist of the differential transient spectra at different delay times. Transient absorption decay curves at different delay times are drawn from the raw data. Decay curves are fitted globally as a sum of exponential functions, which gives the change in absorption as function of wavelength and time:

$$\Delta A(\lambda,t) = \Sigma a_i(\lambda)\exp\left(-\frac{t}{\tau_i}\right), \qquad (5)$$

where a_i is the amplitude and τ_i is the lifetime of the component i. The number of different transient species produced in the photoinduced reaction should correspond to the number of components needed for fitting the data.[25]

The results of the transient absorption measurements are presented[III,V] as decay component spectra, where each component amplitude is plotted as a function of wavelength. In addition, time resolved sum spectra calculated from Eq. 5 are presented[III] to follow the reaction at selected times.

3.10 Differential pulse voltammetry (DPV)

DPV measurements were carried out to determine the HOMO and LUMO energy levels of the studied compounds. A potentiostat (Iviumstat Compactstat IEC 61326 Standard) and a three-electrode cell configuration were employed. 0.1 M tetrabutylammonium hexafluorophosphate ($TBAPF_6$) in dichloromethane (DCM) was used as a supporting electrolyte, a glass platinum electrode as a working electrode, a graphite rod as a counter electrode and platinum wire as a pseudo reference electrode. For each sample, the background was measured for 2.5 ml of the electrolyte solution after 20 min deoxygenation by purging N_2. 100 µl of 0.5 mM sample in DCM was inserted in the reaction vial and the system was stabilized again by purging N_2. Each sample was measured between -2.5 V and 2.0 V scanning in both directions with 2.5 mV steps. Ferrocene (Acros Organics, 98 %) was used as an internal standard reference to scale the measured potentials against vacuum level.[27] HOMO and LUMO level calculations were based on the oxidation and reduction potentials observed in the DPV curves according to Eq. 6 and 7:

$$E_{HOMO} = -(4.8 + E_{dif,ox})eV \text{ and} \quad (6)$$

$$E_{LUMO} = (-E_{dif,red} + 4.8)eV, \quad (7)$$

where 4.8 eV is the oxidation energy of ferrocene. $E_{\mathrm{dif,ox}}$ is the difference in volts between the oxidation potential of ferrocene and the oxidation potential measured for the sample. $E_{\mathrm{dif,red}}$ is the difference in volts between the oxidation potential of ferrocene and the reduction potential of the sample.

3.11 Optical profilometry

To determine the thicknesses of the spin-coated photoactive layers and vacuum evaporated buffer layers, an optical profilometer (Veeco Wyko NT-1100) was employed. A narrow strip of the sample film was removed with a cotton stick dipped in chloroform and the created step was measured using a phase shifting interferometry (PSI) mode. The profilometer monitors the phase shift between two monochromatic light beams reflected from the surfaces of the substrate and the sample film and calculates the step hight. The profilometer data were recorded from an area of 230 × 300 μm^2. The vertical resolution of this method is close to 1 Å and the horizontal resolution of the objective (20-fold magnification) is 0.75 µm.

3.12 Differential scanning calorimetry (DSC)

DSC is a thermal method used for monitoring the physical transformations such as phase transitions or degradation of the sample. The difference in the amount of heat required for increasing the temperature of a sample and reference with well-defined heat capacity over the range of scanned temperatures is measured as a function of temperature. Both the sample and reference are

maintained at nearly the same temperature throughout the experiment. The temperature program of the DSC instrument increases the sample holder temperature linearly as a function of time.

A thermo analyzer (Mettler Toledo DSC821e) was applied for DSC measurements to analyze the thermal properties of the compounds.[I-IV] Crystallinity and thermal stability of the samples were determined based on the observed glass transition steps, endothermic melting peaks or exothermic degradation and oxidation signals. Samples were heated at a rate of 20 ^{o}C/min in a standard 40 μL perforated Al crucible with a 60 mL/min N_2 flow.

3.13 Computational modelling

The computational density functional theory (DFT) calculations on the molecular geometries and electronic structure related properties were conjoined for material characterization and solar cell performance analysis. The calculations were carried out at the Department of Chemistry and Bioengineering, Tampere University of Technology. The modelling of the D-A copolymers **P1**-**P4** and $PC_{60/70}BM$ acceptors [II] was carried out by Mika Niskanen and the calculations for the aryl end-capped quaterthiophenes, **3a**, **3b**, **4a** and **4c**,[IV] and (**DPP-(2TPhCN)$_2$**[V] were performed by Tuuva Kastinen.

4 Results and discussion

In this chapter, the most significant results of the publications I-V are summarized. First, the use of 5-amino substituted Alq_3 derivatives, Alq_3 end-capped oligothiophene, and aryl end-capped quaterthiophenes as anodic hole transporting buffer layers in the inverted organic solar cell is presented. The effect of the used buffer material on the solar cell performance is rationalized by means of their HOMO and LUMO energy levels[I,III,IV] relative to those of the cell structure. The distributions of the computed molecular frontier orbitals provided additional understanding on the buffer properties.[IV] Also, the possible photoactivity of the buffer layer is considered. The relationship between the photovoltaic performance of the conjugated benzodithiophene/fluorine-benzotriazole donor-acceptor (D-A) copolymers with the DFT calculations on their molecular properties is discussed.[II] Finally, the results of the solar cell experiments using Alq_3 and aryl end-capped oligothiophenes as dopants in the photoactive layer of the organic cell are presented.[III,V] Interaction of the dopant molecules with P3HT and $PC_{60}BM$ was studied in detail by steady state and time resolved spectroscopic methods. The effect of the dopant molecules on the cell function and efficiency are discussed based on the performed spectroscopic measurements.

4.1 Solar cell experiments varying the hole transporting buffer layer material

Three different 5-amino substituted Alq_3 derivatives, four aryl end-capped quaterthiophenes, and an Alq_3 end-capped hexathiophene were tested as anodic hole transporting buffer layers in the inverted cell structure. The solar cell performance using the materials as buffer layers was compared with that of the reference cell with an Alq_3 buffer layer. The material types used in the buffer layer experiments differ in their characteristics and the applications where they have been used before. Organometallic Alq_3 derivatives are electron transporting materials and used as photoluminescent materials in OLEDs. Instead, oligothiophenes are hole transporting in nature and have been used as donor materials in different types of organic solar cells. Testing these different material types as hole transporting buffer layers provided information about the shared material properties required to improve the solar cell efficiency.

4.1.1 Organometallic 5-amino substituted Alq_3 derivatives as buffer layers

The organic solar cell with **Al(5-morq)$_3$** as a buffer layer had better efficiency, 2.63 %, compared to that, 2.36 %, of the cell with the reference material, Alq_3, measured one day after the cell preparation (Table 4.1). The cell using **Al(5-morq)$_3$** buffer layer had increased I_{sc}, -3.20 mA/cm^2, and *FF*, 64 %, compared to those, -2.91 mA/cm^2 and 60 %, of the reference cell. V_{oc}, 0.48 V, of the cell with **Al(5-morq)$_3$** was not improved compared that, 0.51 V, of the reference cell as shown by the *I-V* curves (Figure 4.1a).

Efficiencies of all the cells were increased when remeasured 5 months after the cell preparation compared to those measured one day after the cell preparation (Table 4.2). Improvements in the cell efficiency over time are possible for the inverted cells, as the oxidation degree and work function of the ZnO layer change.[28] This improves particularly the cell V_{oc}, but increases also I_{sc} and *FF* as shown by the *I-V* curves of the cells measured one month after the cell preparation (Figure 4.1b).

Table 4.1 Photovoltaic parameters, their standard deviations and resistances of the solar cells with Alq_3 and the 5-amino substituted derivatives as buffer layers measured one day after the cell preparation.[I]

Buffer layer (thickness, nm)	**Cells**	$I_{sc,best}$ (mA/cm^2)	$V_{oc,best}$ (V)	FF_{best} (%)	η_{best} (%)	η_{avg} (%)	R_s (Ω cm^2)	R_{sh} (Ω cm^2)
Alq_3 (4.30)	4	-2.91 ± 0.10	0.51 ± 0.00	60 ± 1.4	2.36 ± 0.06	2.31	17.94	1797
Al(5-pipq)$_3$ (4.00)	10	-3.33 ± 0.32	0.45 ± 0.01	50 ± 3.6	2.02 ± 0.20	1.78	19.65	600
Al(5-pyrq)$_3$ (3.60)	8	-3.01 ± 0.18	0.45 ± 0.02	55 ± 4.2	1.99 ± 0.20	1.76	20.04	820
Al(5-morq)$_3$ (3.66)	10	-3.20 ± 0.36	0.48 ± 0.01	64 ± 6.9	2.63 ± 0.27	2.23	25.72	564

Table 4.2 Photovoltaic parameters, their standard deviations and resistances of the solar cells with Alq_3 and the 5-amino substituted derivatives as buffer layers measured 5 months after the cell preparation.[I]

Buffer layer	**Cells**	$I_{sc,best}$ (mA/cm^2)	$V_{oc,best}$ (V)	FF_{best} (%)	η_{best} (%)	η_{avg} (%)	R_s (Ω cm^2)	R_{sh} (Ω cm^2)
Alq_3	4	-2.89 ± 0.14	0.55 ± 0.15	62 ± 2.3	2.62 ± 0.16	2.41	28.03	2824
Al(5-pipq)$_3$	9	-3.52 ± 0.59	0.53 ± 0.01	56 ± 9.9	2.76 ± 0.41	2.23	30.67	1031
Al(5-pyrq)$_3$	8	-3.46 ± 0.24	0.52 ± 0.01	54 ± 4.3	2.59 ± 0.21	2.31	24.72	752
Al(5-morq)$_3$	10	-3.56 ± 0.22	0.53 ± 0.00	56 ± 5.1	2.80 ± 0.31	2.34	28.70	1161

The best cell with **Al(5-morq)$_3$** as a buffer layer had better efficiency, 2.80 %, than those, 2.62 %, 2.76 % and 2.59 %, of the cells with Alq_3, **Al(5-pipq)$_3$** and **Al(5-pyrq)$_3$**, respectively, also after 5-month storage. The cell with **Al(5-morq)$_3$** had highly improved R_{sh}, 1161 Ωcm^2, measured 5 months after the cell preparation compared to that, 564 Ω cm^2, measured one day after the cell preparation. R_s of the cell with **Al(5-pipq)$_3$** had increased only slightly during the 5-month storage, which resulted in increased I_{sc}, -3.56 mA/cm^2, of the cell.

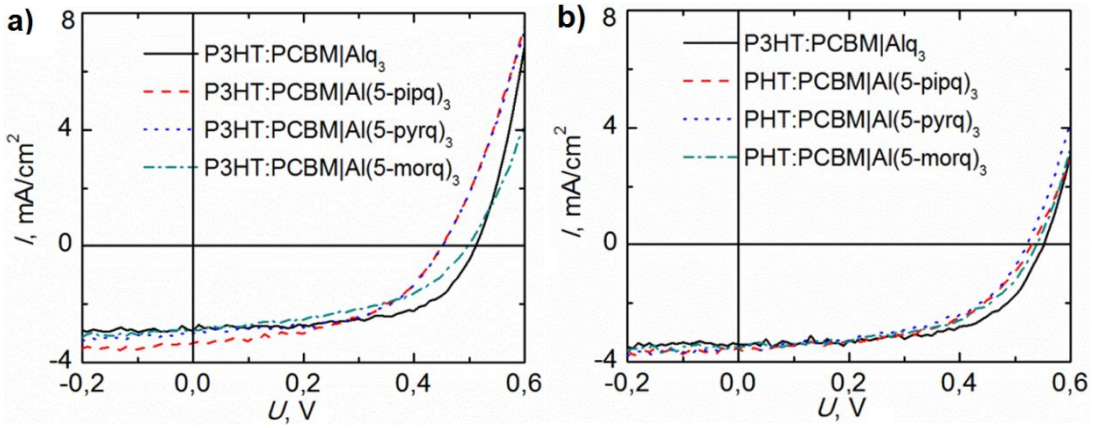

Figure 4.1 *I-V* curves of the solar cells with Alq_3 and the 5-amino substituted derivatives as buffer layers measured one day (a) and 5 months (b) after the cell preparation.[I]

The effect of the buffer material on the cell function can be explained based on the measured HOMO and LUMO energy levels of the derivatives and their positions relative to the those of the adjacent materials in the cell structure. In the inverted cell the anode buffer layer is deposited between the photoactive layer and the Au anode. Energy levels of the parent Alq_3, the 5-amino substituted derivatives and the adjacent P3HT and Au are presented in Figure 4.2. The derivatives have electron donating[16] amino substituents, piperidine, pyrrolidine, or morpholine rings, on 5-position, which ease the oxidation of the complexes and elevate the HOMO energy levels compared to the parent Alq_3.

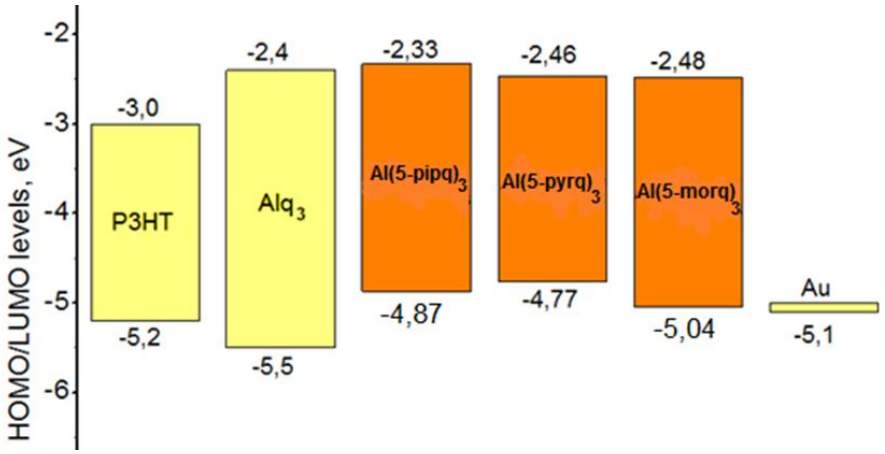

Figure 4.2 Energy levels of the 5-amino substituted derivatives and the parent Alq_3 positioned between the gold electrode and P3HT in the inverted cell structure.[I]

The difference between HOMO of P3HT and that of the buffer layer affects the cell V_{oc}. An injection barrier for holes is formed if HOMO of the buffer material lies higher than that of the P3HT layer. The extraction force for the photogenerated charge carriers decreases due to the diminished built-in field caused by the injection barrier and V_{oc} is decreased.[29] **Al(5-pyrq)$_3$** has the HOMO level higher than those of **Al(5-pipq)$_3$**, **Al(5-morq)$_3$** and the parent Alq_3. Therefore the cell with the **Al(5-pyrq)$_3$** buffer layer has the highest injection barrier and lowest V_{oc}. The device with Alq_3 as an anode buffer layer produced the highest V_{oc}, because the HOMO level of Alq_3 lies lower than that of P3HT and an injection barrier is not created.

An extraction barrier for the photogenerated holes to escape the cell is created if HOMO of the buffer material lies lower than that of P3HT. The HOMO level of Alq_3 is lower than that of P3HT and extraction barrier is created, which decreases the cell I_{sc}. The HOMO levels of all the 5-amino substituted derivatives are higher than that of P3HT and extraction barriers are not created. Therefore the cells with the derivatives as buffer layers produced higher I_{sc} than the reference cell with Alq_3 buffer layer.

Photoactivity of the organometallic Alq_3 buffer layers is considered insignificant to the cell function, because the buffer layers are very thin (Table 4.1). Alq_3 has an absorption maximum at 385 nm (Table 4.3), where solar emission intensity (Figure 2.3) is much weaker than around 430 nm, where the 5-amino substituted derivatives have their absorption maxima (Table 4.3) in solid state. Therefore, the possible cell current improving photoinduced reactions, such as exciton formation, initiated in the 5-amino substituted derivatives would affect the cell function more than those intitiated in Alq_3. The effect of possible photoinduced reactions is questionable, since the cell with **Al(5-morq)$_3$** produced the highest current. **Al(5-morq)$_3$** has a larger absorption coefficient (α) in solid films but significantly shorter average lifetime (τ_{avg}) measured in chloroform solution than **Al(5-pipq)$_3$** and **Al(5-pyrq)$_3$** (Table 4.3).

Table 4.3 Absorption maxima and absorption coefficients in solid films and lifetimes, percentages (amplitudes) of the lifetimes and average lifetimes of the two exponential fits for the derivatives and one exponential fit for the parent Alq_3.[I]

Complex	λ_{film}[a] (nm)	α[b] (μm^{-1})	τ_1[c] (ns)	τ_2[c] (ns)	τ_{avg}[c] (ns)
Al(5-pipq)$_3$	426	1.4	3.54 (56 %)	0.15 (44 %)	2.05
Al(5-pyrq)$_3$	429	1.3	4.83 (87 %)	0.51 (13 %)	4.27
Al(5-morq)$_3$	427	1.8	0.50 (94 %),	5.83 (6 %)	0.82
Alq$_3$	385	2.1[30]	16.62[30]	-	-

[a]Absorption maximum in a solid film, [b]Absorption coefficient in a solid film at 430 nm for the derivatives and at 398 nm for Alq_3, [c] Lifetimes of the components and their average lifetime = $(A_1\tau_1+A_2\tau_2)/2$ (λ_{ex} = 405 nm, λ_{mon} = 560 nm) in chloroform solution

The cell absorption spectra (Figure 4.3) do not show increased absorption of the cells at 430 nm, where the derivatives absorb. However, the cells with the derivatives as buffer layers produced higher current than the cells with Alq_3. Thus, the effect of photoinduced reactions is considered minor to that of the energy level alignment also in the case of the derivatives. Based on the DSC measurements, the 5-amino substituted derivatives are amorphous, whereas Alq_3 is crystalline. Therefore, morphological properties of the derivatives in the solid state differ from those of Alq_3, which might also explain in part the improved hole transporting properties of the derivatives.

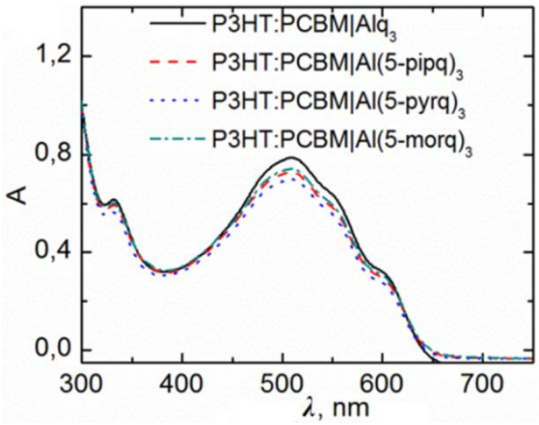

Figure 4.3 Absorption spectra of the cells with Alq_3 and the 5-amino substituted derivatives as buffer layers.[I]

4.1.2 Alq$_3$ and aryl end-capped oligothiophenes as buffer layers

Photovoltaic parameters of the cells with vacuum evaporated **(Alq$_3$)$_2$-OT** anode buffer layers and reference cells with Alq_3 buffer layers measured one day, 4 weeks, and 12 weeks after the cell preparation are shown in Table 4.4. Vacuum evaporation of the relatively large molecular weight **(Alq$_3$)$_2$-OT** molecules was successful, as shown by the reference quartz plate absorption spectra of the films (Figure 4.4). Evaporation was carried out between 185 – 285 °C and the thermal degradation of **(Alq$_3$)$_2$-OT** molecules takes place at around 400 °C based on performed DSC measurements.[III]

Efficiencies of the cells with the **(Alq$_3$)$_2$-OT** anode buffer layer were not improved compared to the reference cell with the Alq_3 buffer layer when measured one day after the cell preparation. The best cell with the Alq_3 buffer layer had higher V_{oc}, 0.55 V, and *FF*, 60 %, than those of the best

cell with **$(Alq_3)_2$-OT** buffer, 0.46 V and 55 %. The best cell of those with the **$(Alq_3)_2$-OT** buffer layer had a lower R_s, 29.19 Ω cm^2, and a higher I_{sc}, -2.84 mA/cm^2, than those of the reference cell, 39.64 Ω cm^2 and -2.62 mA/cm^2.

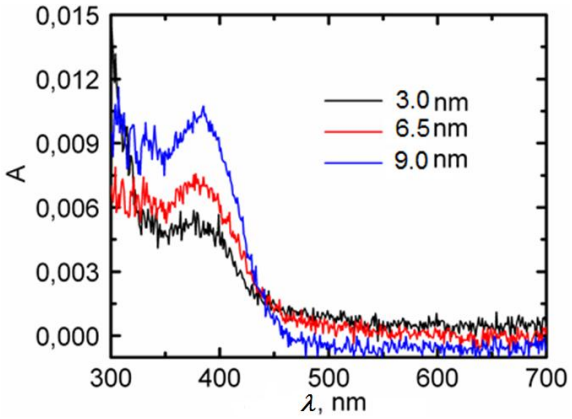

Figure 4.4 Absorption spectra of the thermally vacuum evaporated (185 – 285 °C) 3.0 nm, 6.5 nm and 9.0 nm thick **$(Alq_3)_2$-OT** films.[III]

Table 4.4 Photovoltaic parameters, their standard deviations and resistances of the cells with different buffer layers: 5 nm Alq_3 (9 cells), 6.5 nm **$(Alq_3)_2$-OT** (10 cells) or 9 nm **$(Alq_3)_2$-OT** (10 cells).[III]

Buffer layer (thickness, nm)	**Time**	$I_{sc,best}$ **(mA/cm^2)**	$V_{oc,best}$ **(V)**	FF_{best} **(%)**	η_{best} **(%)**	η_{avg} **(%)**	R_s **(Ω cm^2)**	R_{sh} **(Ω cm^2)**
Alq_3 (5)	One	-2.62 ± 0.15	0.55 ± 0.005	60 ± 1.6	2.42 ± 0.14	2.25	39.64	1499
$(Alq_3)_2$-OT(6.5)	day	-2.71 ± 0.34	0.50 ± 0.011	58 ± 4.9	2.18 ± 0.28	1.93	28.72	1385
$(Alq_3)_2$-OT (9.0)		-2.84 ± 0.22	0.46 ± 0.014	55 ± 6.6	1.99 ± 0.33	1.86	29.19	931.1
Alq_3 (5)	4	-2.54 ± 0.23	0.54 ± 0.006	61 ± 5.6	2.33 ± 0.27	2.05	45.12	1998
$(Alq_3)_2$-OT (6.5)	weeks	-2.85 ± 0.52	0.53 ± 0.009	58 ± 1.9	2.45 ± 0.41	2.22	29.62	1310
$(Alq_3)_2$-OT (9.0)		-3.11 ± 0.36	0.51 ± 0.010	56 ± 1.9	2.47 ± 0.29	2.06	33.43	1494
Alq_3 (5)	12	-2.32 ± 0.25	0.55 ± 0.005	61 ± 3.0	2.28 ± 0.20	2.03	46.20	2098
$(Alq_3)_2$-OT (6.5)	weeks	-2.76 ± 0.52	0.52 ± 0.009	61 ± 2.0	2.54 ± 0.47	2.10	29.44	1545
$(Alq_3)_2$-OT (9.0)		-2.81 ± 0.34	0.54 ± 0.004	56 ± 4.9	2.45 ± 0.34	2.13	35.84	2453

As the cells were remeasured 4 weeks after the cell preparation, the efficiencies of the best cells with **$(Alq_3)_2$-OT** buffer layers were better than those of the reference cells. The cells with **$(Alq_3)_2$-OT** had an improved V_{oc}, only a slightly increased R_s, and therefore a higher I_{sc} compared to those measured one day after the cell preparation. The R_s of the reference cell with the Alq_3 buffer layer had increased during the 4 four-week storage up to 45.12 Ω cm^2. Thus, the cell produced a lower I_{sc}, -2.54 mA/cm^2, than that measured one day after the cell preparation, which caused the decrease in the cell efficiency. The cells were measured once more 12 weeks after the cell preparation and the photovoltaic parameters corresponded to those measured 4 weeks after the cell preparation.

Energy levels of **$(Alq_3)_2$-OT** are suitably aligned with those of the cell materials (Figure 4.5). The HOMO level of **$(Alq_3)_2$-OT** is higher than that of Alq_3. The extraction barrier for the photogenerated holes to escape the cell is not created when **$(Alq_3)_2$-OT** is used as a buffer material instead of Alq_3. This may explain the reduced R_s values of the cells with **$(Alq_3)_2$-OT** compared to those with Alq_3. Photoactivity of the **$(Alq_3)_2$-OT** buffer layers is considered minor, as the

absorptions of the layers are as low as 0.005 – 0.010 (Figure 4.4) and they absorb at wavelengths beyond the solar intensity maxima (Figure 2.3).

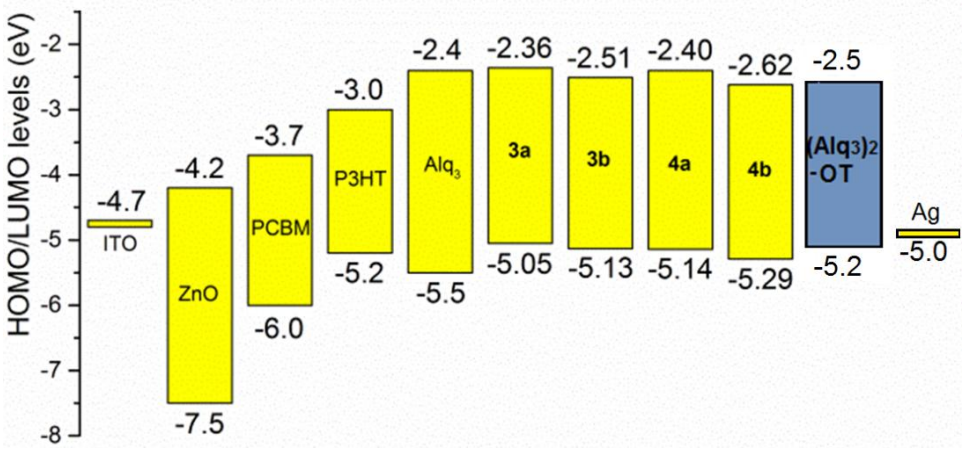

Figure 4.5 Energy levels of the inverted solar cell structure[9] and HOMO and LUMO levels measured for **3a**, **3b**, **4a**, **4b** and **$(Alq_3)_2$-OT**.[III, IV]

The photovoltaic parameters of the cells using aryl end-capped quaterthiophenes as anode buffer layers are in Table 4.5. The use of *p*-cyanophenyl end-capped quaterthiophene, **4b,** as the hole transporting buffer layer improved the cell efficiency up to 3.27 %, compared to that of the reference cell with an Alq_3 buffer layer, 2.76 %. Furthermore, one cell out of ten, using **4a** a as buffer layer, had improved efficiency, 3.00 %, compared to the reference cell. However, the average efficiencies, 2.51 %, 2.50 % and 2.52 %, of the cells with **3a**, **3b** or **4a**, respectively, were only slightly improved compared to that of the reference cells, 2.46 %. The best cell, with **4b** as the buffer layer, had a higher I_{sc}, -3.17 mA/cm^2, than that of the reference cell, -2.72 mA/cm^2. V_{oc}, 0.53 V, and *FF*, 62 %, of the best cell with **4b** remained nearly the same as those of the best reference cell, 0.55 V and 61 % (Figure 4.6a). The HOMO level of **4b** (Figure 4.5) lies in the optimal position relative to that of P3HT and remarkable extraction or injection barrier for the hole transport are not created, which explains the improved current production partly.

Table 4.5 Photovoltaic parameters and their standard deviations of the cells with Alq_3 and aryl end-capped derivatives as buffer layers.[IV]

Buffer (thickness)*	**Number of cells**	$I_{sc,best}$ **(mA/cm^2)**	$V_{oc,best}$ **(V)**	FF_{best} **(%)**	η_{best} **(%)**	η_{avg} **(%)**
Alq_3 (5 nm)	10	-2.72 ± 0.18	0.55 ± 0.006	61 ± 3.0	2.76 ± 0.20	2.46
3a (10 nm)	6	-2.73 ± 0.19	0.55 ± 0.008	62 ± 2.6	2.84 ± 0.25	2.51
3b (4 nm)	5	-2.74 ± 0.18	0.55 ± 0.005	58 ± 4.2	2.72 ± 0.25	2.50
4a (5 nm)	10	-3.12 ± 0.18	0.56 ± 0.006	60 ± 3.0	3.00 ± 0.20	2.52
4b (13 nm)	5	-3.27 ± 0.19	0.53 ± 0.004	62 ± 2.2	3.27 ± 0.24	2.85

*Best result of three tested layer thicknesses (~5 nm, ~10 nm and ~15 nm),

Photoactivity of the aryl end-capped buffer layers is possible as the absorptions of the cells with aryl end-capped quaterthiophenes as buffer layers are increased compared to that of the reference cell with Alq_3 as a buffer layer (Figure 4.6b). The aryl end-capped quaterthiophenes absorb at wavelengths from 350 nm to 550 nm (Figure 4.7), where solar emission intensity is strong (Figure 2.3). Absorption maxima of *p*-cyanophenyl end-capped quaterthiophenes are red shifted and

therefore overlap more with the solar emission spectrum compared to *p*-methoxyphenyl end-capped quaterthiophenes. In addition, the excited state lifetimes in the solid films of the derivatives do not differ significantly (Table 4.6). Thus, the effect of possible photoinduced reactions in *p*-cyanophenyl end-capped quaterthiphenes is stronger than in *p*-methoxyphenyl end-capped quaterthiophenes.

Table 4.6. Fluorescence lifetimes of the quaterthiophenes in solid films based on a three exponential fit (λ_{ex} = 483 nm and λ_{mon} = 600 nm).[IV]

Compound	τ_1 (ns)	τ_2 (ns)	τ_3 (ns)
3a	1.81	0.40	0.05
3b	1.61	0.58	0.06
4a	1.16	0.26	0.05
4b	1.77	0.23	0.04

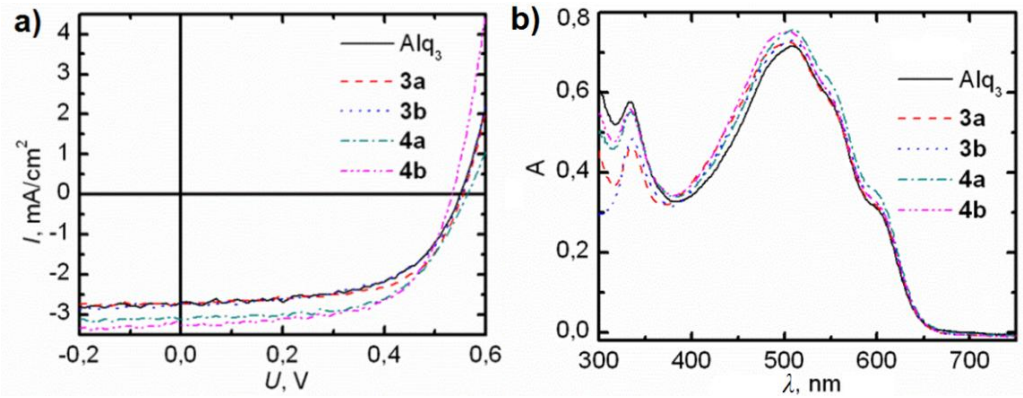

Figure 4.6 *I-V* curves (a) and absorption spectra (b) of the cells with Alq_3 (7 nm), **3a** (10 nm), **3b** (4 nm), **4a** (5 nm), and **4b** (13 nm) buffer layers.[IV]

Based on the performed transient absorption measurements, energy transfer between **4b** and $PC_{60}BM$ is possible.[V] Thus, the excited **4b** molecules of the buffer layer could transfer energy or electrons to $PC_{60}BM$ and increase the amount of excited $PC_{60}BM$ molecules and excitons in the adjacent BHJ photoactive layer. If the additional excitons are within the diffusion length from the donor-acceptor interface, charges are separated and additional current is possibly produced.

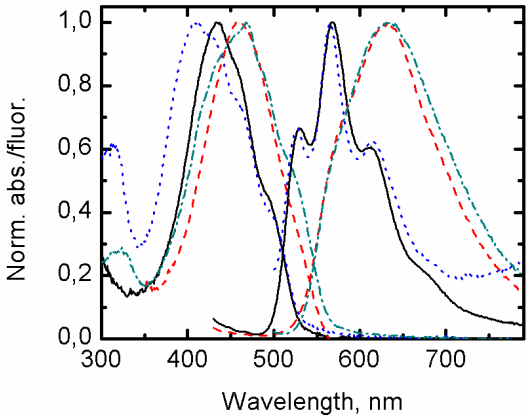

Figure 4.7 Normalized absorption and fluorescence emission (λ_{ex} = 483 nm) spectra of **3a** (blue dot), **3b** (green dash-dot), **4a** (black solid) and **4b** (red dash) of solid vacuum evaporated films.[IV]

Based on the computational calculations of the molecular geometry, the backbones of the *p*-cyanophenyl end-capped quaterthiophenes, **3b** and **4b**, are more planar and have more extended π-conjugation compared to the *p*-methoxyphenyl end-capped quaterthiophenes, **3a** and **4a**. This red shifts the absorption of the *p*-cyanophenyl end-capped quaterthiophenes with respect to the *p*-methoxyphenol quaterthiophenes.

The computed frontier molecular orbitals are shown in Figure 4.8. 90 % of the LUMO electron density is localized on the quaterthiophene backbone in **3a** and **4a**, but only 75 % in **3b** and **4b**. 10 % of the LUMO is localized at the end groups in **3a** and **4a** and 25 % in **3b** and **4b**. Thus, the LUMO electron density is spread more evenly throughout the oligomer structure in the *p*-cyanophenyl end-capped quaterthiophenes than in the *p*-methoxyphenyl end-capped quaterthiophenes. The possible photoinduced exciton diffusion in the excited state and additional current production should be more efficient in the cells with **3b** and **4b** buffer layer compared to cells with **3a** and **4a** buffer layers. This could further explain the increased I_{sc} of the cell with **4b** buffer layer together with the optimal energy levels of the molecule.

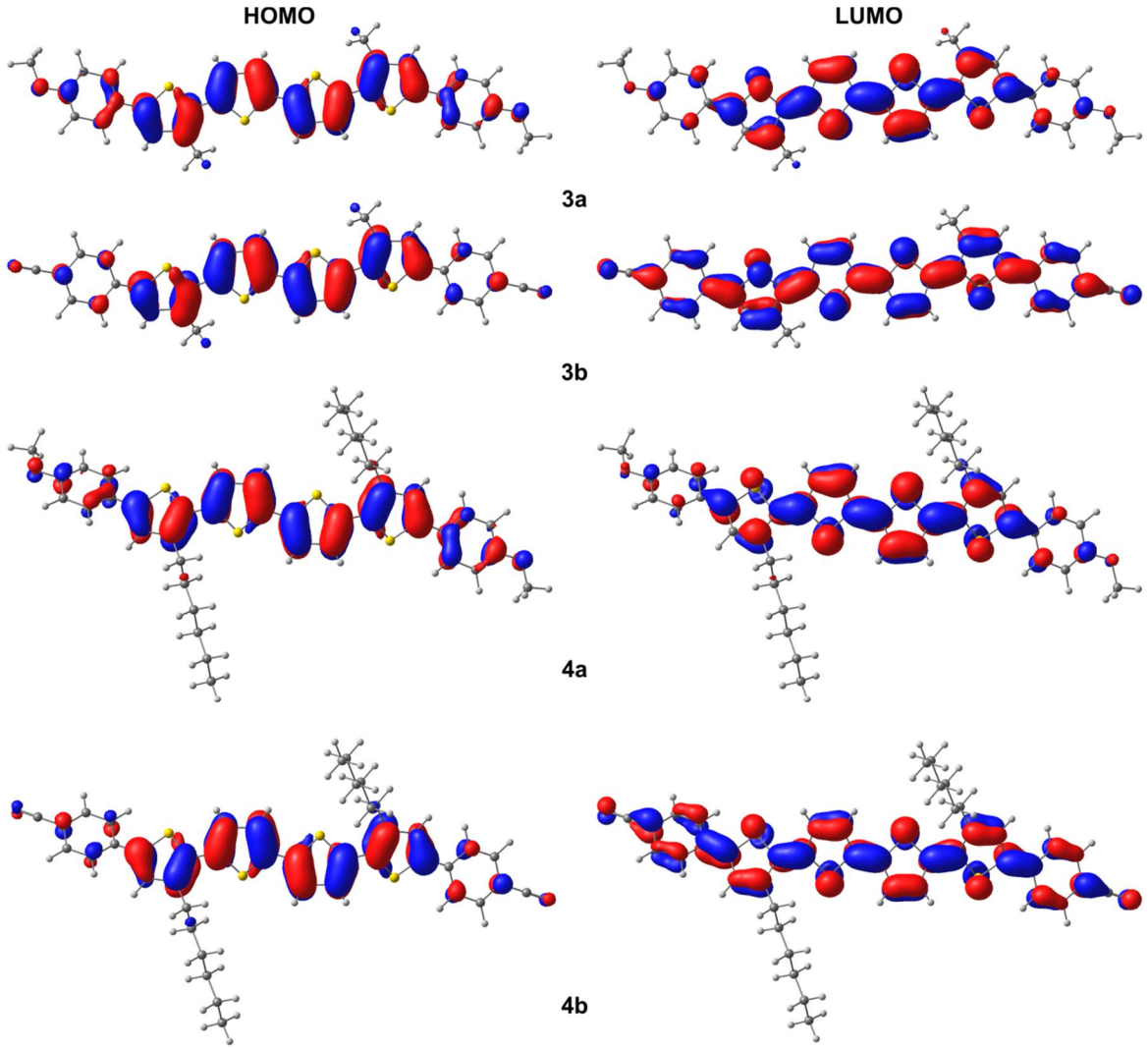

Figure 4.8 Frontier molecular orbitals of **3a**, **3b**, **4a** and **4b** calculated at the B3LYP/6-31G** level of theory.[IV]

4.2 Conjugated benzodithiophene/fluorine-benzotriazole donor-acceptor (D-A) copolymers as donor materials in organic solar cells

Conjugated donor-acceptor copolymers, **P1**-**P4**, were tested as donor molecules in organic solar cells with $PC_{60}BM$ and $PC_{70}BM$ acceptor molecules. The polymers' molecular geometries, energy levels, molecular orbitals, and the effect of interaction with the acceptor molecule on the energy levels were calculated with DFT. Atomic force microscopy (AFM) images of the cell active layers supplement the performed experimental and modeling studies. Investigations aimed at better understanding about the relationship between photovoltaic performance and molecular structures.[II]

4.2.1 Solar cell experiments using P1-P4 as donor materials

A benzodithiophene-benzotriazole D-A copolymer, **P4**, was used as a donor material in inverted organic cells. Performance of **P4** was compared with those of three fluorine-benzotriazole D-A copolymers, **P1**-**P3**, which have been tested previously in conventional organic solar cells under a nitrogen atmosphere.[31] **P4** and **P1** were used as donor materials with both $PC_{60}BM$ and $PC_{70}BM$, testing different donor:acceptor mass ratios, solvents and annealing temperatures. **P2** was used as a donor material with $PC_{60}BM$ only. P3HT was used as a reference donor material with the $PC_{60}BM$ acceptor. The cell with **P3** donor and $PC_{60}BM$ acceptor did not give any photovoltaic response, and is therefore left out of the discussion.

The photovoltaic parameters of the optimized cells measured one day after the cell preparation, using each polymer as a donor material, are shown in Table 4.7. None of the D-A copolymers performed as well as P3HT as a donor material. The cell with **P1** had higher best cell efficiency and significantly higher V_{oc} and I_{sc} than those of the cells with **P2** and **P4**. The cells with **P4** had higher average efficiency, 0.66 %, than the cells with **P1** and **P2**, 0.58 % and 0.12 %, respectively. The cell with **P1** produced significantly higher efficiency, 0.83 %, when $PC_{60}BM$ was used as an acceptor material compared to that with $PC_{70}BM$, 0.27 %. The cell with **P4** had higher efficiency, 0.74 %, with $PC_{70}BM$ acceptor than that with $PC_{60}BM$, 0.57 %.

Table 4.7 Photovoltaic parameters and their standard deviations of the solar cells with P3HT, **P1**, **P2** or **P4** donors and $PC_{60}BM$ or $PC_{70}BM$ acceptors measured one day after the cell preparation.[II]

D:A (thickness, nm)	**D:A***	**Cells**	$\boldsymbol{I_{sc,best}}$ **(mA/cm^2)**	$\boldsymbol{V_{oc,best}}$ **(V)**	$\boldsymbol{FF_{best}}$ **(%)**	$\boldsymbol{\eta_{best}}$ **(%)**	$\boldsymbol{\eta_{avg}}$ **(%)**
P3HT:C$_{60}$ (100)	1.3 : 1	9	-3.09 ± 0.21	0.52 ± 0.01	69 ± 7.7	3.04 ± 0.41	2.47
P1:C$_{60}$ (65)	1 : 4.0	5	-1.53 ± 0.18	0.48 ± 0.02	42 ± 1.4	0.83 ± 0.07	0.58
P1:C$_{70}$ (55)	1 : 4.6	10	-0.73 ± 0.03	0.34 ± 0.02	40 ± 1.1	0.27 ± 0.01	0.25
P2:C$_{60}$ (130)	1 : 4.1	5	-0.65 ± 0.13	0.43 ± 0.01	29 ± 0.9	0.21 ± 0.05	0.12
P4:C$_{60}$ (40)	1 : 2.7	10	-1.17 ± 0.07	0.45 ± 0.03	41 ± 3.0	0.57 ± 0.07	0.43
P4:C$_{70}$ (30)	1 : 3.1	10	-1.13 ± 0.04	0.41 ± 0.02	59 ± 1.9	0.74 ± 0.06	0.66

*Mass ratio = m(donor):m(acceptor)

The cells were measured again 6 months after the cell preparation. Photovoltaic parameters of the cells and changes in the best cell efficiency and V_{oc} are shown in Table 4.8. The efficiency of the **P4**:$PC_{70}BM$ cell improved the most from 0.74 % up to 1.03 %, as its V_{oc} improved from 0.41 V to 0.59 V during the 6-month storage. Whereas, the efficiency of **P4**:$PC_{60}BM$ cell decreased by 0.24 % during the storage. The cell with P3HT had the largest loss in the efficiency, -0.88 %. The

efficiency of the **P1**:$PC_{70}BM$ cell increased slightly while the **P1**:$PC_{60}BM$ cell remained nearly the same.

Table 4.8 Photovoltaic parameters and their standard deviations of the solar cells with P3HT, **P1**, **P2** and **P4** donors and $PC_{60}BM$ and $PC_{70}BM$ acceptors measured 6 months after the cell preparation.[II]

D:A	Cells	$I_{sc,best}$ (mA/cm^2)	$V_{oc,best}$ (V)	FF_{best} (%)	η_{best} (%)	η_{avg} (%)	$\Delta\eta$[a] (%)	ΔV_{oc},[b] (V)
P3HT:C_{60}	3	-2.46 ± 0.18	0.55 ± 0.03	59 ± 3.3	2.16 ± 0.41	2.06	-0.88	+0.03
P1:C_{60}	5	-1.31 ± 0.17	0.56 ± 0.01	40 ± 1.3	0.80 ± 0.08	0.70	-0.03	+0.08
P1:C_{70}	10	-0.69 ± 0.17	0.47 ± 0.11	40 ± 7.2	0.35 ± 0.10	0.28	+0.08	+0.13
P2:C_{60}	5	-0.31 ± 0.08	0.56 ± 0.09	25 ± 2.3	0.12 ± 0.03	0.09	-0.12	+0.13
P4:C_{60}	5	-0.63 ± 0.03	0.43 ± 0.01	45 ± 2.1	0.33 ± 0.02	0.30	-0.24	-0.02
P4:C_{70}	10	-1.01 ± 0.12	0.59 ± 0.07	62 ± 10	1.03 ± 0.27	0.93	+0.29	+0.18

[a]Change in the best cell efficiency during 6 month storage,[b]Change in the best cell V_{oc} during the 6 month storage

The results of the solar cell experiments are explicable by means of the D-A copolymer absorption properties up to a certain point. Since **P4** absorbs at longer wavelengths than **P1** and **P2** (Figure 4.9), absorption and current production of the cells with **P4** extend to longer wavelengths than those of the cells with **P1** or **P2** (Figure 4.10).

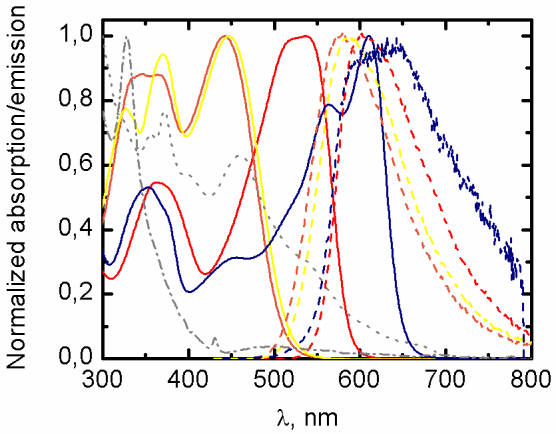

Figure 4.9 Normalized absorption (solid lines) and emission (dashed lines, λ_{ex} = 485 nm) of the donor polymers **P1** (red), **P2** (orange), **P3** (yellow) and **P4** (blue) and absorption of the acceptors $PC_{60}BM$ (dash-dotted line) and $PC_{70}BM$ (dotted line) in chloroform.[II]

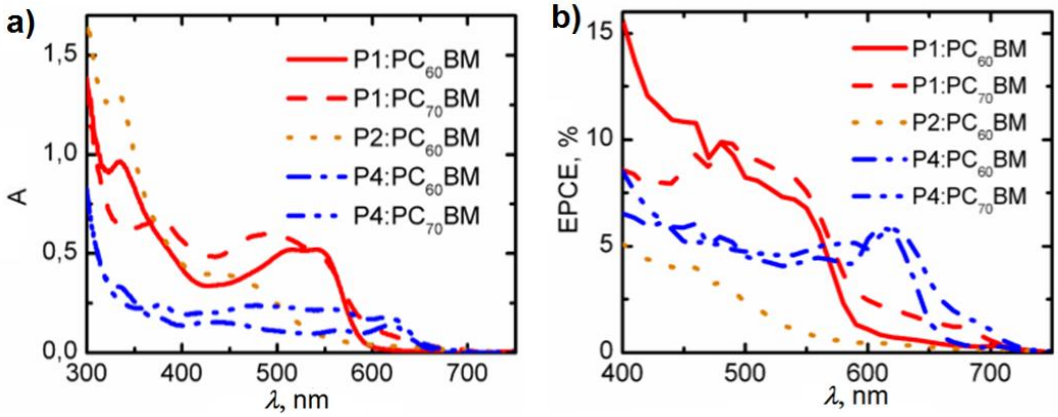

Figure 4.10 Absorption (a) and EPCE (b) spectra of the **P1**:$PC_{60}BM$/$PC_{70}BM$, **P2**:$PC_{60}BM$ and **P4**:$PC_{60}BM$/$PC_{70}BM$ cells.[II]

The V_{oc} values of the cells with **P1** and **P4** donors vary with the used acceptor material, $PC_{60}BM$ or $PC_{70}BM$. The cell V_{oc} depends on the energy difference between donor molecule HOMO and acceptor molecule LUMO levels. Since the LUMO levels of $PC_{60}BM$ and $PC_{70}BM$ are close, -3.7 eV and -3.6 eV (Figure 4.11), respectively, the V_{oc} should be the same using either of the acceptor materials.

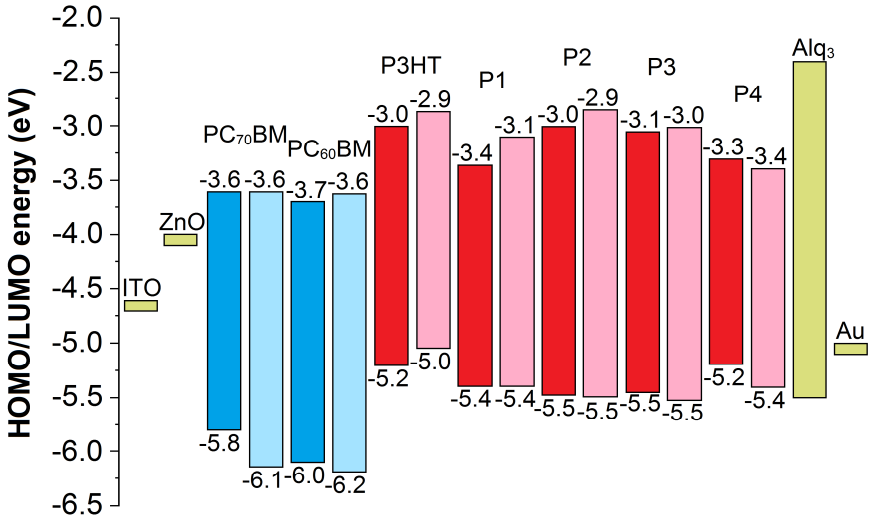

Figure 4.11 Energy level diagram of the donor molecules (red), acceptor molecules (blue), buffer layer materials (green) and electrodes (green) used in the organic solar cells. The experimental values are shown in dark blue/red and the modeled values in light blue/red.[II]

4.2.2 Modelling of the D-A copolymers

To understand better the solar cell performance and the variation in V_{oc} depending on the used acceptor, DFT calculations on polymers' molecular geometries, energy levels, molecular orbitals, and the effect of acceptor molecules on the polymer energy levels were carried out. In the computational models of **P1**-**P4** the solubility enhancing long alkyl side chains, $-C_8H_{17}$ or $-C_6H_{13}$, and $-OC_{10}H_{21}$ or $-OCH_2CH(C_2H_5)C_4H_9$, were replaced by short side chains, $-CH_3$ and $-OCH_3$, respectively. This reduced the computational time and allowed modeling of the oligomer chains up to 7–8 constitutional repeating units (CRUs) and investigating of the convergence of the HOMO-LUMO gaps. Periodic models were built based on the optimized oligomer structures shown in Figure 4.12. As the CRU of **P1** is bent due to the dithiophene 2-phenyl benzotriazole moiety, the periodic **P1** model was built from two **P1** CRUs, which create a zigzagging and almost planar polymer backbone. The methyl substituents of the two 3-methylthiophene rings in the CRU enlarge the backbone dihedral angles in **P2** and **P3**, which prohibits planarity. As a result, the π-conjugation weakens or is broken at some points in the backbones of the **P2** and **P3** polymers. For **P2** and **P3** the periodic models consisted of three CRUs, which create a helical backbone. The periodic model of **P4** consists of a linear and almost planar single CRU.

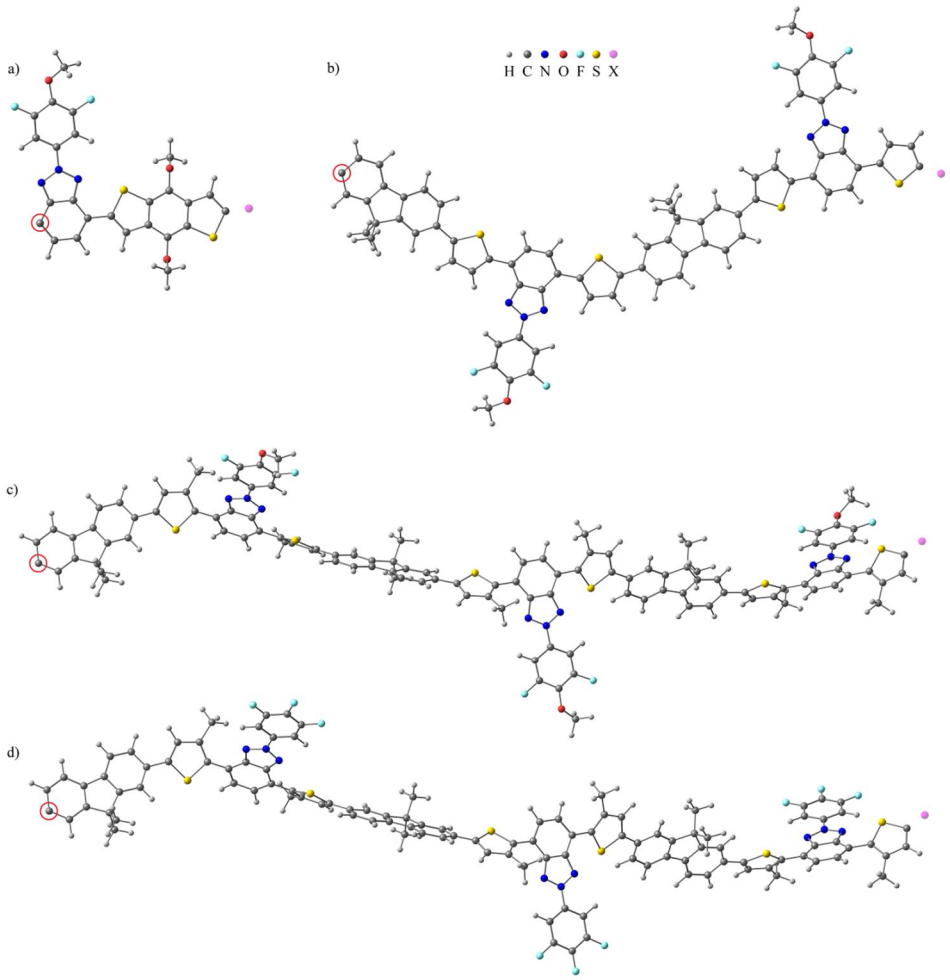

Figure 4.12 Periodic models of **P4** (a), **P1** (b), **P2** (c) and **P3** (d). The repeating structure is copied and translated from the circled carbon atom to the position marked as a pink dummy-atom.[II]

The backbones of **P2** and **P3** are helical due to the steric hindrance of the hexyl chains attached to the thiophene rings, which weakens the π-conjugation in the polymer backbone. The structure of **P1** is zigzagging, but however planar, due to missing hexyl chains. Therefore π-conjugation is stronger and absorption of **P1** is red-shifted compared to **P2** and **P3**. A more planar structure of **P4** compared to those of **P1**-**P3** is due to absence of the thiophene moieties in the polymer backbone. In the nearly planar backbone of **P4** the conjugation is the strongest and absorption red-shifted compared to those of **P1**-**P3**.

The HOMO-LUMO gap energies of oligomers approach the HOCO-LUCO (highest occupied crystal orbital, lowest unoccupied crystal orbital) gap energies of the periodic models as the oligomer length is increased, so the HOCO-LUCO gaps were taken as final computational results for the **P1**-**P4** polymers. The HOCO-LUCO gaps were direct band gaps. The computed energy level gaps (Figure 4.11) are systematically only a bit larger (0.12 eV-0.26 eV) than the experimental values obtained by the electrochemical measurements and the agreement between the two is qualitatively good.

The computed molecular orbitals are presented in Figure 4.13. In **P1**, **P2** and **P3** the HOCO is evenly distributed, and polymer backbone is evenly delocalized, but the LUCO is much more

localized on the 2-phenyl benzotriazole moieties, especially in **P2** and **P3**. In the case of **P2** and **P3** localization most probably results from a weaker π-conjugation along the polymer backbone, as suggested before. In **P4**, as in P3HT, both HOCO and LUCO are evenly delocalized along the polymer backbone, although the **P4** LUCO spreads further into the 2-phenyl benzotriazole derivative.

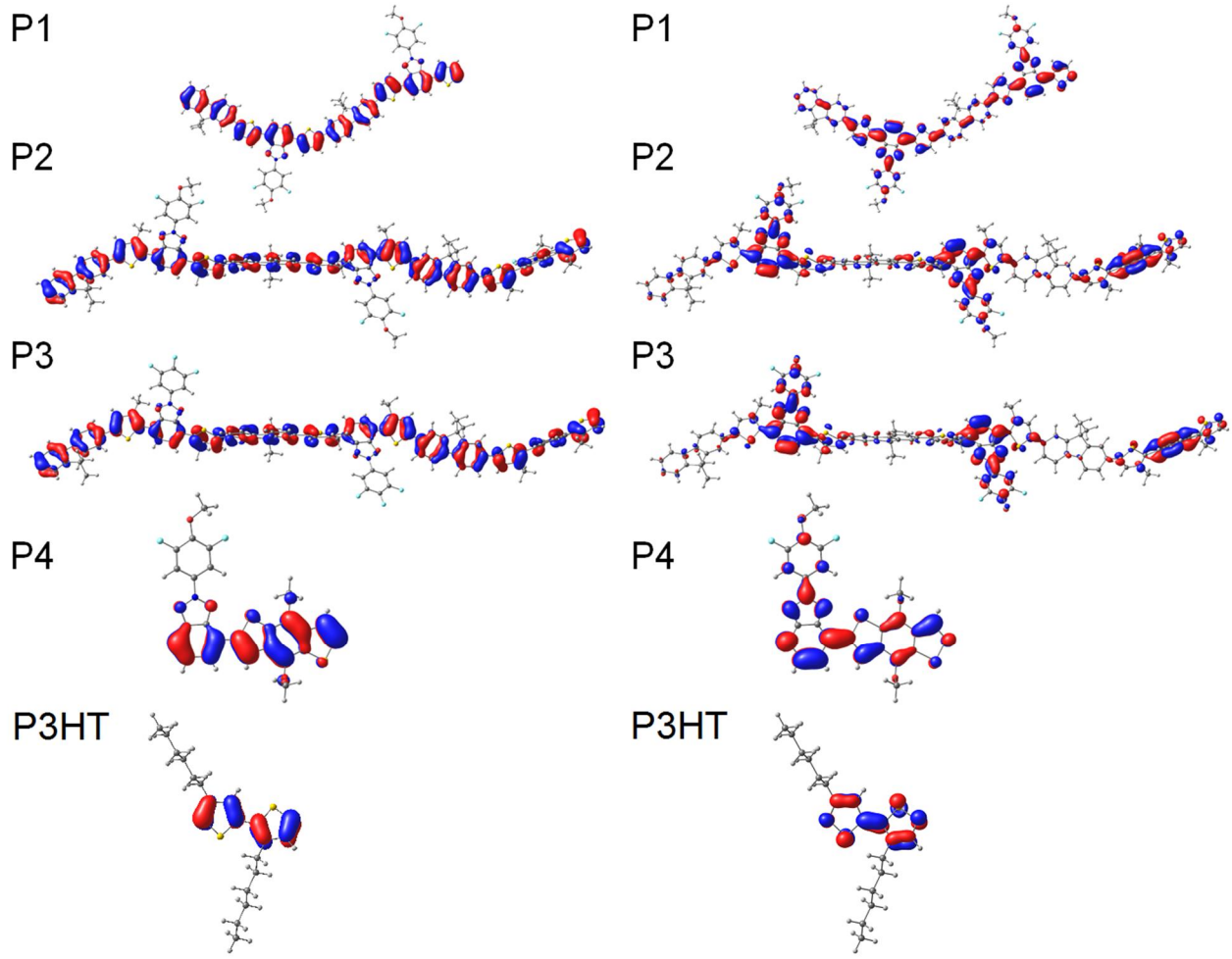

Figure 4.13 The HOCO (left) and LUCO (right) of **P1**-**P4** and P3HT.[II]

The differences in localizations of the LUCOs are expected to affect the exciton diffusion in **P1**-**P4**, because LUCO is partly occupied in excitation and thus participates in the exciton diffusion. Therefore, the exciton diffusion effectivity in the excited state of the polymers can be compared based on the molecular frontier orbitals. LUCOs of **P2** and **P3** are strongly located in the benzotriazole moieties of the polymer backbones and the orbitals are not continuous. The exciton diffusion length in the excited states of **P2** and **P3** might be decreased, if the excitons are trapped in the LUCO orbital spatial gaps. The LUCO orbitals of **P1** and **P4** have continuous electron density throughout the polymer backbones. The N_{MCC} (maximum condusive chain length) values correlate with the conjugation length in the polymer backbones. The calculated N_{MCC} values of **P1** and **P4**, 62 and 59, respectively, are larger than those of **P2** and **P3**, 47 and 37, respectively. Thus, excitons can be expected to diffuse further in **P1** and **P4** than in **P2** and **P3**. HOCOs of **P1**-**P4** are relevant for the hole transport in the materials. Longer conjugation along the backbones leads to better hole

transport in **P1** and **P4** than in **P2** and **P3**, as the last mentioned polymers backbone twists are more likely and may create hole traps.

4.2.3 AFM images of the P1/P4 and $PC_{60/70}BM$ photoactive layers

The differences in the molecular structures of the polymers most probably lead to differences in phase separation and morphology of the photoactive BHJ layer. A rough insight to the active layer morphology was achieved by the AFM images of the cells (Figure 4.14). Usually, small roughness and root mean square (RMS) values and small grain features are correlated with enhanced crystallinity, which offers better power conversion efficiency.[32]

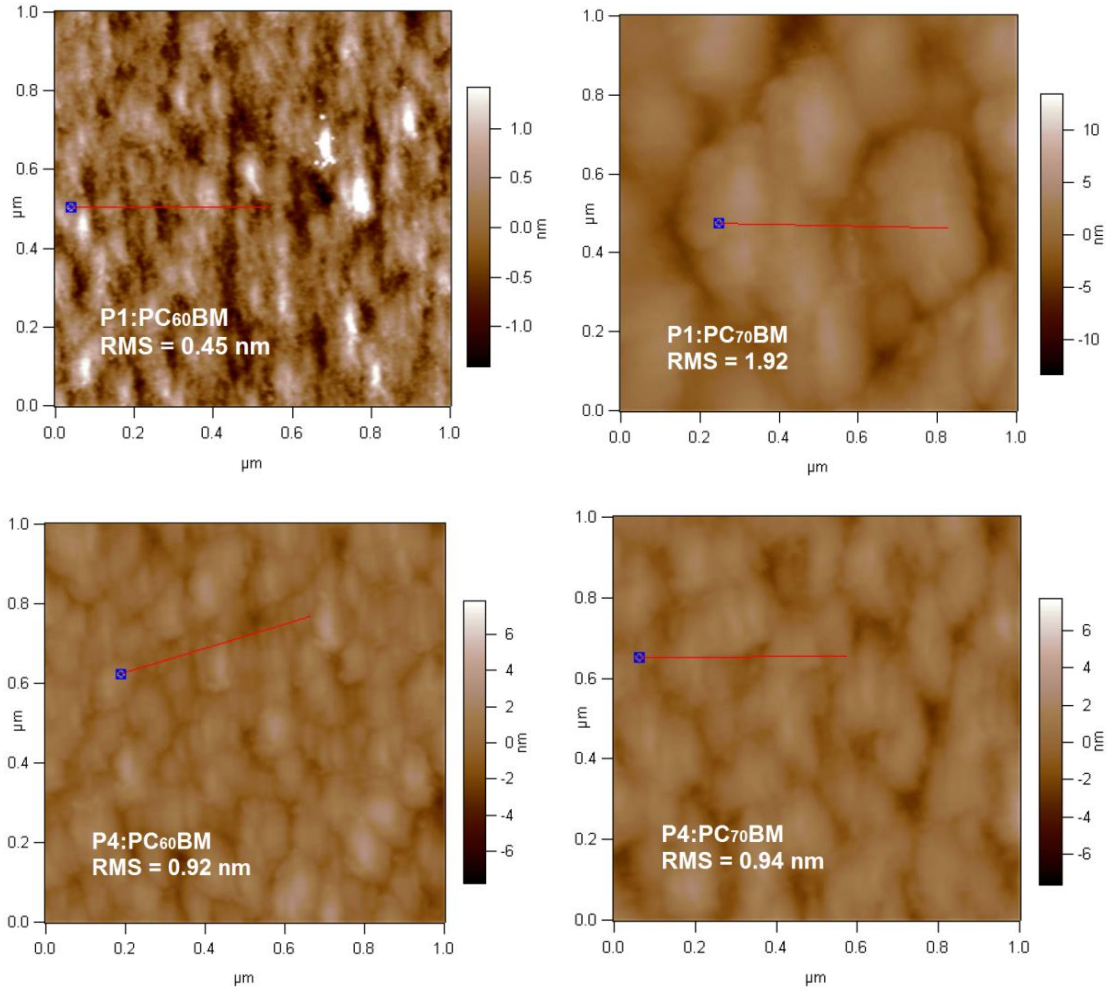

Figure 4.14 AFM images of the **P1**:$PC_{60}BM$/$PC_{70}BM$ and **P4**:$PC_{60}BM$/$PC_{70}BM$ cells.[II]

The RMS value of **P1**:$PC_{70}BM$, 1.92 nm, is significantly larger than that of the **P1**:$PC_{60}BM$ film, 0.45 nm. Large aggregates and grain features can be seen in the **P1**:$PC_{70}BM$ film. The aggregation may lead to current losses due to excessively long conduction paths compared to the exciton diffusion length in the **P1**:$PC_{70}BM$ film. Therefore, the excitons created in the **P1**:$PC_{70}BM$ cell recombine before reaching the donor-acceptor interface more probably than in the **P1**:$PC_{60}BM$ cell. The efficiency, 0.80 %, of the **P1**:$PC_{60}BM$ cell was better than that of the **P1**:$PC_{70}BM$ cell, 0.35 %.

Active layer morphologies of the **P4**:$PC_{60}BM$ and **P4**:$PC_{70}BM$ cells appear very similar, as are the RMS values, 0.92 nm and 0.94 nm respectively. Thus, the film formation properties do not seem to cause the difference between the performance of the **P4**:$PC_{60}BM$ and **P4**:$PC_{70}BM$ cells.

4.2.4 Computed polymer-$PC_{60/70}BM$ interactions and their relation to the solar cell performance

Single **P1** and **P4** monomers with full side chains were studied together with the $PC_{60}BM$ and $PC_{70}BM$ acceptors in combined models to see how their interaction affects the energy levels. The energy levels of the combined models were compared to the energy levels of the isolated monomers and PCBMs. The PCBMs were arranged in three different positions: a) close to the side chains away from the main backbone, b) close to the electron rich moiety of the monomer and c) close to the electron deficient moiety of the monomer (Figure 4.15). The models were fully optimized.

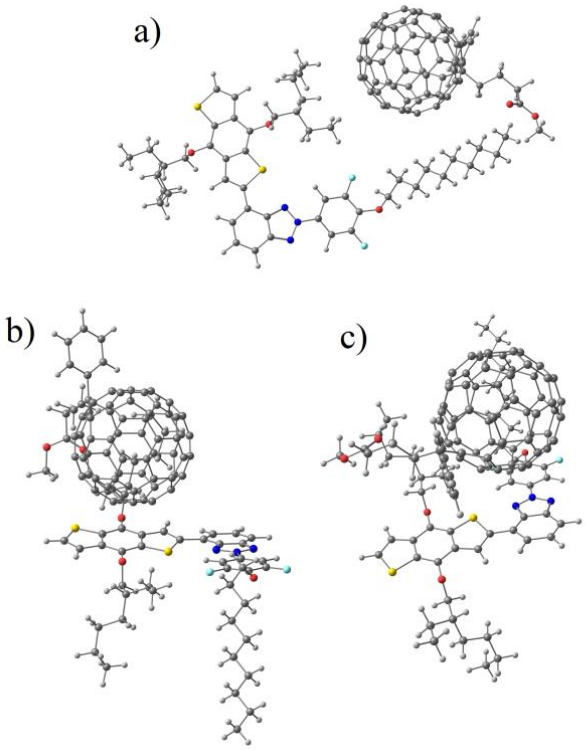

Figure 4.15 Models, where $PC_{60}BM$ is close to the side chains (a), the electron rich moiety (b) and the electron deficient moiety (c) of **P4**.[II]

The largest changes in energies were observed in the model consisting of the **P4** monomer and $PC_{70}BM$ (Figure 4.16). Both the HOMO and LUMO energies of $PC_{70}BM$ increase and those of **P4** decrease, which leads to a larger energy gap between the **P4** monomer HOMO and the $PC_{70}BM$ LUMO, when the $PC_{70}BM$ is close to either the electron rich or the electron deficient moiety of the **P4** monomer. The larger V_{oc} value for the **P4**:$PC_{70}BM$ cell compared to that of the **P4**:$PC_{60}BM$ cell can be explained by the increased energy gap between the **P4** monomer HOMO and the $PC_{70}BM$ LUMO.

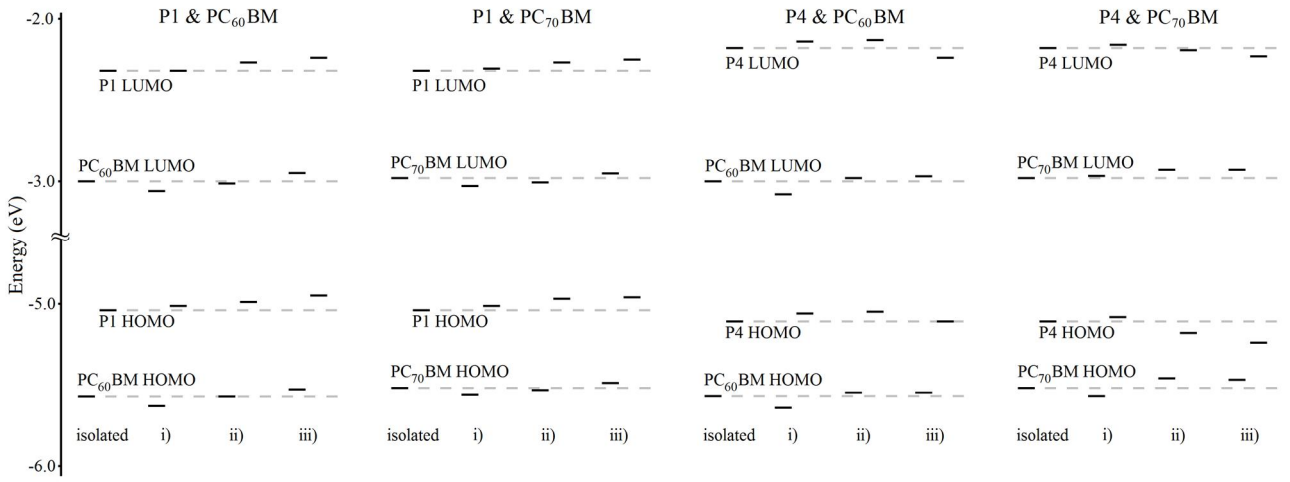

Figure 4.16 Molecular orbital energies of the isolated **P1** and **P4** monomers, $PC_{60/70}BM$ and combined models.[II]

4.3 Oligothiophenes as dopants in the P3HT:$PC_{60}BM$ BHJ photoactive layer

Alq_3 and aryl end-capped oligothiophenes were used as dopants in the photoactive layer of the organic solar cells. The effect of dopant molecules on the cell function was studied by solar cell experiments, spectroscopic measurements of the solar cells, and electrochemical measurements of the dopant molecules. To understand better the function of the dopant molecules in the cell, solution studies on the interaction of the dopant molecules with the photoactive layer components, P3HT and $PC_{60}BM$, were carried out. Intra- and intermolecular interactions of dopants with $PC_{60}BM$ were studied by using steady state and time resolved optical spectroscopic methods.

4.3.1 The effect of $(Alq_3)_2$-OT doping on the cell function

Alq_3 and its derivatives have been used as dopants in the photoactive layer of organic solar cells, which increased significantly the efficiency of the cells.[30] The amount of the organometallic complexes as dopant molecules in BHJ photoactive layer is limited due to the poor solubility of the complexes. High concentrations of the dopant complexes deteriorate the active layer morphology and decrease the cell efficiency. **$(Alq_3)_2$-OT** consists of two Alq_3 complexes attached to a solubilizing hexathiophene backbone with hexyl chains. **$(Alq_3)_2$-OT** was applied as a dopant material in order to test the compatibility of the molecule with the active layer components and its effect on the cell function.[III]

Efficiencies of the cells were not improved when the reference material, phenoxyquinoline end-capped hexathiophene (compound **5**), was used as dopant material.[III] Photovoltaic parameters of the reference cell without doping and the cells with different concentrations of **$(Alq_3)_2$-OT** dopant molecules are shown in Table 4.9. The best cell with 0.15 mM **$(Alq_3)_2$-OT** had better efficiency, 2.63 %, than that, of the reference cell, 2.33 %, measured one day after the cell preparation. The cells were measured again 4 weeks after the cell preparation. The efficiency of the best cell with 0.15 mM **$(Alq_3)_2$-OT** had improved up to 2.85 %, whereas the efficiency of the reference cell remained nearly the same as measured one day after the cell preparation. The cell with 0.15 mM **$(Alq_3)_2$-OT** had better values of V_{oc}, 0.55 V, I_{sc}, -2.99 mA/cm^2 and *FF*, 62 %, compared to those of

the reference cell, 0.53 V, -2.74 mA/cm^2 and 57 %. Thus, doping of the active layer with **$(Alq_3)_2$-OT** affects both the cell voltage and its current.

Table 4.9 Photovoltaic parameters and their standard deviations of the reference cell without doping and the cells with different concentrations of **$(Alq_3)_2$-OT** dopant molecules.[III]

*c** (mM)	Storage time	Number of cells	$I_{sc,best}$ (mA/cm^2)	$V_{oc,best}$ (V)	FF_{best} (%)	η_{best} (%)	η_{avg} (%)
0	1 day	8	-2.86 ± 0.27	0.50 ± 0.005	59 ± 6.1	2.44 ± 0.31	2.07
0.15	"	9	-2.97 ± 0.33	0.52 ± 0.004	61 ± 2.8	2.63 ± 0.37	2.50
0.60	"	9	-3.00 ± 0.16	0.52 ± 0.010	60 ± 2.6	2.62 ±.0.17	2.31
0.90	"	8	-2.52 ± 0.12	0.53 ± 0.005	55 ± 5.4	2.07 ± 0.25	1.90
0	4 weeks	9	-2.74 ± 0.20	0.53 ± 0.007	57 ± 4.8	2.31 ± 0.27	2.06
0.15	"	9	-2.99 ± 0.15	0.55 ± 0.011	62 ± 5.1	2.85 ± 0.29	2.55
0.60	"	10	-2.66 ± 0.20	0.56 ± 0.006	60 ± 2.4	2.49 ± 0.19	2.22
0.90	"	7	-2.59± 0.12	0.55± 0.007	60 ± 5.8	2.36 ± 0.22	2.13

***Concentration of **$(Alq_3)_2$-OT** in the spin-coated P3HT:PC_{60}BM solution

The effect of large concentration of Alq_3 and the corresponding amount of the complexes in **$(Alq_3)_2$-OT** molecules was compared by doping the cells with 1.14 mM Alq_3 and 0.57 mM **$(Alq_3)_2$-OT** (Table 4.10). Doping with large amount of Alq_3 complexes decreased the cell efficiency, whereas the same amount of Alq_3 complexes bound in **$(Alq_3)_2$-OT** in the active layer increased the cell efficiency compared to that of the reference cell without doping. This indicates that the compatibility of **$(Alq_3)_2$-OT** molecules with the active layer components is better than that of Alq_3.

Table 4.10 Photovoltaic parameters and their standard deviations of the reference cell without doping and the cells doped with large concentrations of (**$(Alq_3)_2$-OT** and Alq_3.[III]

Dopant	Number of cells	*c** (mM)	$I_{sc,best}$ (mA/cm^2)	$V_{oc,best}$ (V)	FF_{best} (%)	η_{best} (%)	η_{avg} (%)
No dopant	3	-	-2.67 ± 0.15	0.53 ± 0.005	63 ± 0.6	2.51 ± 0.16	2.33
$(Alq_3)_2$-OT	9	0.57	-2.84 ± 0.18	0.56 ± 0.009	60 ± 2.6	2.69 ± 0.17	2.40
Alq_3	3	1.14	-2.74 ± 0.13	0.51 ± 0.006	49 ± 6.3	2.41 ± 0.34	2.10

***Concentration of dopant in the spin-coated P3HT:PC_{60}BM solution

The cells with different concentrations of **$(Alq_3)_2$-OT** had increased absorbance compared to that of the reference cell without doping (Figure 4.17). Increased absorption of the doped cells at 550 nm and 600 nm indicates different crystallization of P3HT in the presence of the dopant molecules. The increase in the cell efficiency with **$(Alq_3)_2$-OT** doping is partly due to advantageous morphological changes of the BHJ active layer, which possibly increase the exciton and charge transport in the layer. This supports further the compatibility of **$(Alq_3)_2$-OT** molecules in the BHJ layer.

Furthermore, the cells with **$(Alq_3)_2$-OT** absorb more than the reference cell around 380 nm, where **$(Alq_3)_2$-OT** molecules absorb in the solid state (Figure 4.4). Thus, the **$(Alq_3)_2$-OT** dopant molecules function as additional light absorbers in the photoactive BHJ layer and photoinduced reactions, such as electron transfer to PC_{60}BM, are possible. Interactions of the molecules were studied by steady state and time resolved methods to understand better the possible contribution of the dopant molecules to the cell function.

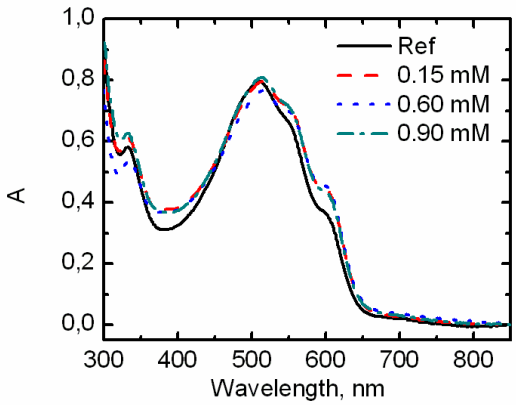

Figure 4.17 Absorption spectra of the reference cell without doping and cells with different concentrations of **$(Alq_3)_2$-OT** dopant molecules in the BHJ layer.[III]

4.3.1.1 Steady state measurements of $(Alq_3)_2$-OT with $PC_{60}BM$

The films of **$(Alq_3)_2$-OT**, $PC_{60}BM$, and their mixtures of three different mass ratios, 1:0.025, 1:0.05, and 1:0.09, were prepared for steady state studies. Absorption spectra of the mixtures and pure **$(Alq_3)_2$-OT** and $PC_{60}BM$ films are shown in Figure 4.18a. The emission of **$(Alq_3)_2$-OT** is quenched as a function of $PC_{60}BM$ content in the solid films (Figure 4.18b). Because $PC_{60}BM$ quenches the emission of **$(Alq_3)_2$-OT**, it seems that **$(Alq_3)_2$-OT** and $PC_{60}BM$ have an interaction in the excited state.

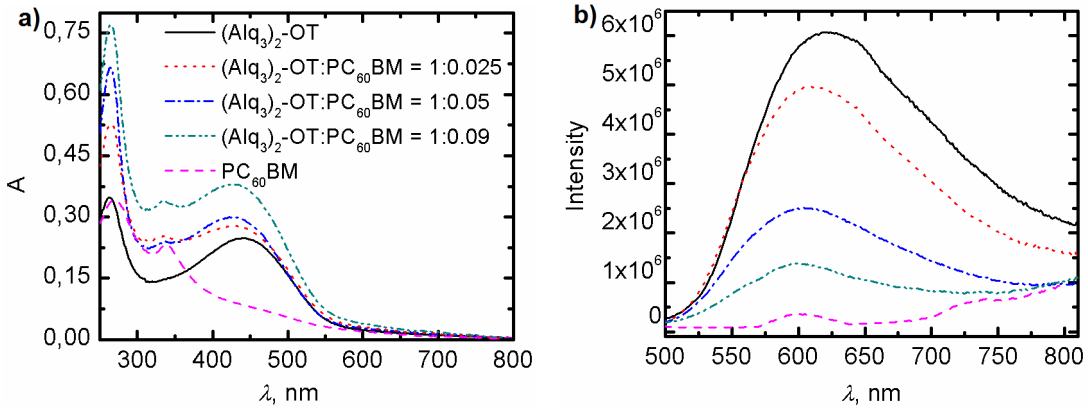

Figure 4.18 Absorption (a) and emission (λ_{ex} = 405 nm) (b) spectra of **$(Alq_3)_2$-OT**, $PC_{60}BM$ and their mixtures of three different mass ratios in films.[III]

4.3.1.2 Time resolved emission and absorption studies on the intra- and intermolecular interactions of $(Alq_3)_2$-OT and $PC_{60}BM$

Spectroscopic properties of **$(Alq_3)_2$-OT**, reference compound **5,** and Alq_3 in chloroform solutions are shown in Table 4.11. The fluorescence intensity of **$(Alq_3)_2$-OT** is red shifted and ten times weaker than those of the reference compound **5** and Alq_3. This could be due to intramolecular charge transfer from the hexathiophene backbone to the Alq_3 moieties in **$(Alq_3)_2$-OT**.

Table 4.11 Spectroscopic properties of compound **5**, **$(Alq_3)_2$-OT** and Alq_3 in chloroform (λ_{ex} = 405 nm, λ_{mon} = 520 nm for Alq_3 and 600 nm for compound **5** and **$(Alq_3)_2$-OT**).[III]

Compound	Concentration (mM)	$\lambda_{abs,max}$ (nm)	A_{405nm}	$\lambda_{PL,max}$ (nm)	$I_{PL,max}$	τ_1 (ns)	τ_2 (ns)
5	0.22	423	1.46	545	4.9×10^7	0.71	-
$(Alq_3)_2$-OT	0.22	427	0.98	604	2.7×10^6	0.40	14
Alq_3	0.44	388	0.42	528	1.9×10^7	16	-

For TCSPC measurements of **$(Alq_3)_2$-OT**, the excitation wavelength of 483 nm was used to solely excite the oligothiophene backbone of the **$(Alq_3)_2$-OT**. As shown in Figure 4.19, excitation at 483 nm results in only one component, similar to the short living component when excited at 405 nm. Energy transfer from the oligothiophene backbone to the Alq_3 moieties can be excluded, because the 14 ns component does not exist when exciting at 483 nm.

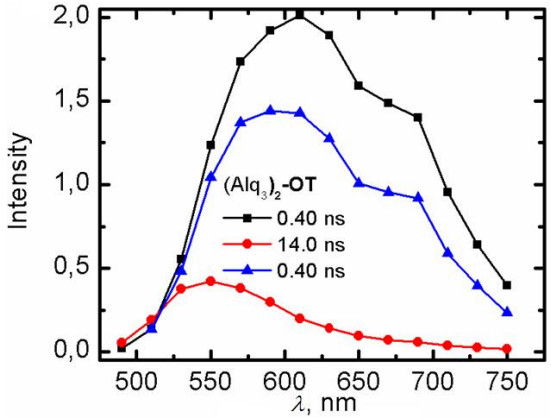

Figure 4.19 Fluorescence DAS of **$(Alq_3)_2$-OT** *(*λ_{ex} = 405 nm: black squares and red circles, λ_{ex} = 483 nm: blue triangles).[III]

To further investigate the possible photoinduced reactions, transient absorption spectra of **$(Alq_3)_2$-OT** in the presence and in the absence of $PC_{60}BM$ were measured with a pump-probe set-up in chloroform (Figure 4.21). The reaction scheme of the intramolecular photoinduced reactions in **$(Alq_3)_2$-OT** and the most probable reaction paths in the presence of $PC_{60}BM$ are presented in Figure 4.20 to facilitate the following discussion about the transient spectra.

With the 390 nm excitation, both the oligothiophene backbone and Alq_3 moieties are excited (Figure 4.21a). The first component (blue triangles), is formed very fast (<< 2 ps) indicated by negative bands at the wavelength areas, at which hexathiophene cation radical, around 800 nm,[33] and Alq_3 anion radical, around 550 nm,[34] have their absorptions. This state was described as excited charge transfer complex (CTC), covering the positive bands from 600 to 1050 nm. CTC decays in 2 ps to an intramolecular charge transfer state (ICTS, black circles). The broad absorption of ICTS, from 600 nm to 1000 nm, consists of the broadened and red shifted absorptions of the Alq_3 anion (550 nm and longer) and hexathiophene cation radicals (800 nm and longer). The charge transfer state recombines to the ground states with a lifetime of 250 ps. The third component with τ > 2000 ps (red squares) is associated to the broad and long-lived (τ = 14 ns by TCSPC) singlet excited state of the Alq_3 moiety.[35]

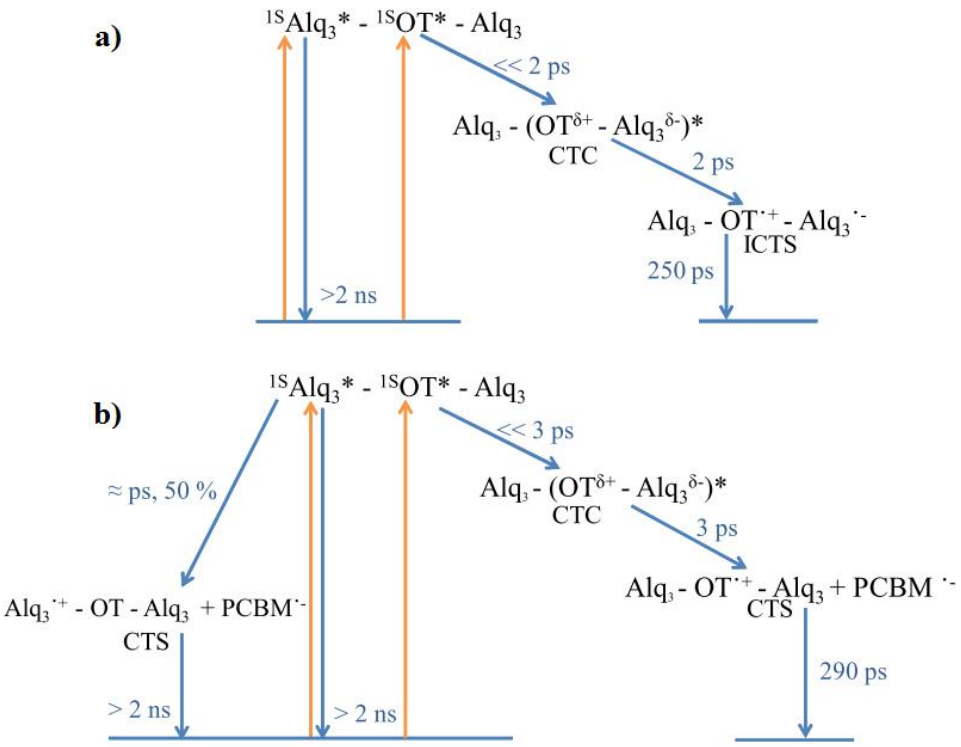

Figure 4.20 Reaction scheme of the phenomena in **$(Alq_3)_2$-OT** (blue arrows) after photoexcitation (yellow arrows) in the absence (a) and in the presence (b) of $PC_{60}BM$.[III]

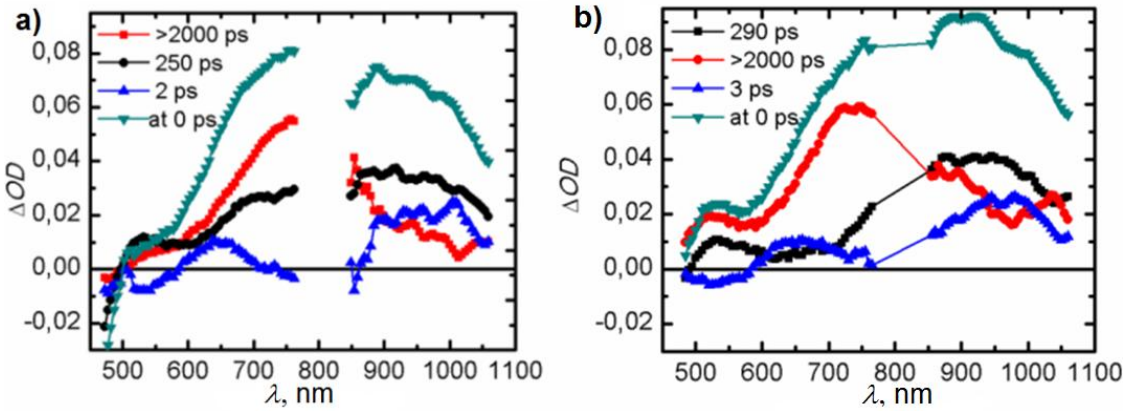

Figure 4.21 Decay component spectra and calculated transient spectrum at 0 ps delay time of **$(Alq_3)_2$-OT** (0.22 mM) in the absence (a) and in the presence (b) of $PC_{60}BM$ (λ_{ex} = 390 nm).[III]

Mixing **$(Alq_3)_2$-OT** with $PC_{60}BM$ causes changes both in the decay component spectra (Figure 4.21) and in the time-resolved absorption spectra (Figure 4.22 and 4.23). The first component (τ = 3 ps, blue triangles, Figure 4.21b) corresponds to the CTC state similar as in Figure 4.21a, in the absence of $PC_{60}BM$. The essential changes are observed in the second component (τ = 290 ps, black squares), in which the short wavelength (600 nm – 750 nm) component of the absorption, corresponding to the Alq_3 anion radical band in Figure 4.21a, is absent. Evidently, $PC_{60}BM$ has captured the electron from the formed ICTS and only the absorption of the hexathiophene cation radical is left. Its lifetime is increased, because the recombination with the counter anion radical is delayed. Instead it recombines with the $PC_{60}BM$ radical anion with lifetime of about 290 ps.

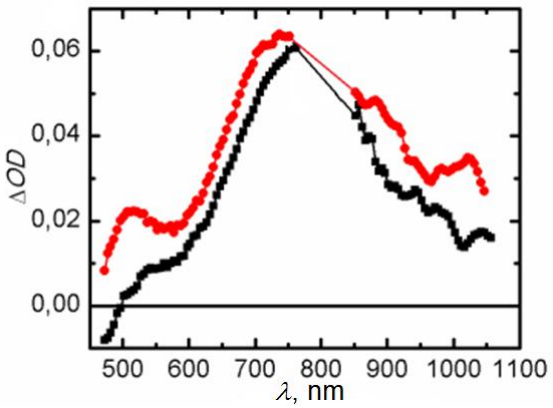

Figure 4.22 Calculated transient absorption spectra of **$(Alq_3)_2$-OT** (0.22 mM) in the absence (black squares) and presence (red circles) of $PC_{60}BM$ (0.84 mM) 300 ps after the excitation (λ_{ex} = 390 nm).[III]

There are, however, $PC_{60}BM$ anion radicals present after 300 ps (Figure 4.22) and 1000 ps (Figure 4.23) after excitation, as indicated by the absorption bands at 1050 nm.[33] Thus there is another way for its formation. An alternative path for the formation of $PC_{60}BM$ radical anion could be the electron transfer from Alq_3 singlet excited state to $PC_{60}BM$. This could also be seen as Alq_3 cation radical band at 550 nm[34] in Figures 4.21b, 4.22 and 4.23b.

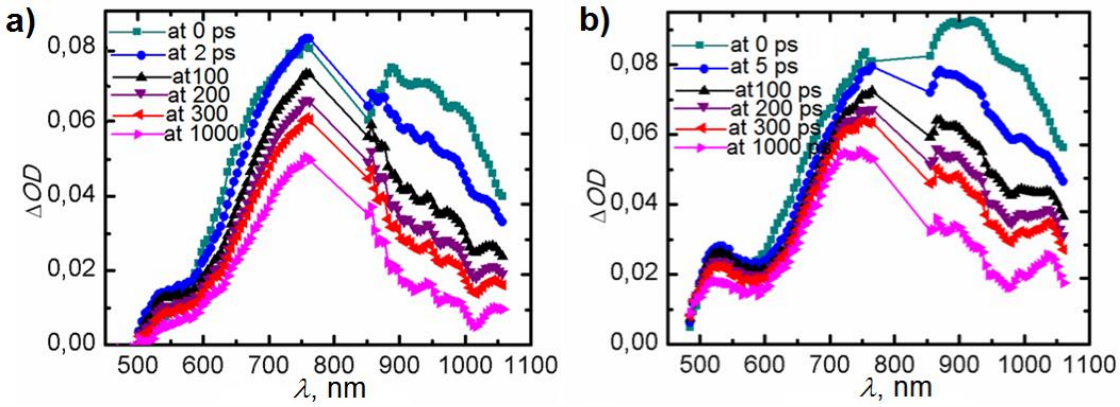

Figure 4.23 Transient absorption spectra of the **$(Alq_3)_2$-OT** (0.22 mM) in the absence (a) and in the presence (b) of $PC_{60}BM$ (0.84 mM) at 0 ps, 2 ps, 5 ps, 100 ps, 200 ps, 300 ps and 1000 ps after photoexcitation at 390 nm in chloroform.[III]

To conclude, the **$(Alq_3)_2$-OT** dopant molecules increase the cell efficiency. As the LUMO level of **$(Alq_3)_2$-OT**, -2.5 eV, is higher than that of $PC_{60}BM$, -3.7 eV, **$(Alq_3)_2$-OT** is capable of donating electrons to $PC_{60}BM$. **$(Alq_3)_2$-OT** functions as an additional light-absorber in the BHJ layer, which increases the cell I_{sc}. Simultaneously, the *FF* and V_{oc} values of the cell increase due to advantageous P3HT crystallization changes and improved transport properties of the BHJ layer caused by the **$(Alq_3)_2$-OT** molecules.

4.3.2 The effect of DPP-group in the properties and function of a *p*-cyanophenyl end-capped oligothiophene dopant material

$DPP\text{-}(2TPhCN)_2$ was synthesized in order to include a DPP-group in the center of the **di-(*p*-PhCN)T4** (previously named as **4b**[IV]) aryl end-capped oligothiophene structure. Both molecules,

di-(*p*-PhCN)T4 and **DPP-(2TPhCN)$_2$** were used as a dopant material in the inverted cells. Doping with **DPP-(2TPhCN)$_2$** improved the cell efficiency, while the influence of **di-(*p*-PhCN)T4** on the cell efficiency was modest. Interactions of the dopant molecules with the active layer components, P3HT and $PC_{60}BM$, were studied by steady state and time resolved spectroscopic methods. The studies aimed to understand the effect of DPP-group inclusion on the molecular properties and function as a dopant material.[V]

4.3.2.1 Photovoltaic performance of DPP-(2TPhCN)$_2$ doped cells

DPP-(2TPhCN)$_2$ doping improved the cell efficiency significantly, when the content of the dopant molecules in the photoactive layer was 3.5 m-% or 5.0 m-% of the P3HT:$PC_{60}BM$:dopant mixture total mass (Table 4.12). Efficiencies of the best cells with 3.5 m-% or 5.0 m-% content of **DPP-(2TPhCN)$_2$** dopant molecules were 2.95 % and 3.26 %, respectively, compared to that of the reference cell, 2.77 %, measured one day after the cell preparation. The average efficiency of the cells, with 3.5 m-% doping content, was 2.73 % compared to that of the ten non-doped reference cells, 2.41 %.

Table 4.12 The content (2.5 – 10 mass percent, m-%) of **DPP-(2TPhCN)$_2$** dopant molecules in the photoactive layer of the P3HT:$PC_{60}BM$ cell, the corresponding photovoltaic parameters measured one day after the cell preparation and their standard deviations, and those of the **DPP-(2TPhCN)$_2$**:$PC_{70}BM$ (60:40 m-%) cell.[V]

m-%	mol-%	Number of cells	$I_{sc,\,best}$ (mA/cm^2)	$V_{oc,best}$ (V)	FF_{best} (%)	η_{best} (%)	η_{avg} (%)
0	**0**	9	-2.85 ± 0.14	0.55 ± 0.008	57 ± 6.3	2.77 ± 0.35	2.41
2.5	**0.7**	9	-2.46 ± 0.25	0.54 ± 0.008	62 ± 7.2	2.45 ± 0.29	2.10
3.5	**1.0**	10	-2.94 ± 0.16	0.55 ± 0.004	58 ± 8.2	2.95 ± 0.24	2.73
5.0	**1.4**	10	-3.28 ± 0.29	0.54 ± 0.010	62 ± 6.7	3.26 ± 0.41	2.57
6.5	**1.8**	9	-2.74 ± 0.31	0.55 ± 0.003	53 ± 6.6	2.50 ± 0.43	1.96
10	**2.7**	7	-1.86 ± 0.24	0.55 ± 0.008	41 ± 4.1	1.28 ± 0.08	1.18
60*	**59**	4	-1.20 ± 0.23	0.61 ± 0.036	34 ± 2.1	0.74 ± 0.10	0.61

*__DPP-(2TPhCN)$_2$__:$PC_{70}BM$ (60:40) cell

Table 4.13 The content (2.5 – 10 m%) of **DPP-(2TPhCN)$_2$** dopant molecules in the photoactive layer of the P3HT:$PC_{60}BM$ cell, the corresponding photovoltaic parameters measured one month after cell preparation and their standard deviations.

m%	mol%	Number of cells	$I_{sc,\,best}$ (mA/cm^2)	$V_{oc,best}$ (V)	FF_{best} (%)	η_{best} (%)	η_{avg} (%)
0	**0**	9	-2.83 ± 0.17	0.54 ± 0.012	61 ± 4.7	2.78 ± 0.27	2.40
2.5	**0.7**	8	-2.65 ± 0.30	0.56 ± 0.007	65 ± 9.4	2.99 ± 0.55	2.25
3.5	**1.0**	9	-3.04 ± 0.19	0.57 ± 0.003	59 ± 3.4	3.16 ± 0.21	2.80
5.0	**1.4**	9	-3.28 ± 0.36	0.57 ± 0.005	62 ± 7.0	3.60 ± 0.59	2.88
6.5	**1.8**	9	-3.06 ± 0.44	0.56 ± 0.007	49 ± 10	2.59 ± 0.64	1.90
10	**2.7**	4	-2.43 ± 0.55	0.58 ± 0.032	38 ± 3.7	1.65 ± 0.35	1.17

When the cells were remeasured after one month storage in the dark (Table 4.13), efficiencies of the best cells with 3.5 m-% and 5.0 m-% content of **DPP-(2TPhCN)$_2$** dopant increased up to 3.16 % and 3.60 %, respectively, compared to that of the reference cell, 2.78 %. The average efficiency of the cells with 5.0 m-% content of **DPP-(2TPhCN)$_2$** dopant increased up to 2.88 % compared to that of the reference cells, 2.40 %.

The V_{oc} of the cells with **DPP-(2TPhCN)$_2$** dopant molecules changed remarkably during the storage compared to that of the reference cells. The efficiency of **DPP-(2TPhCN)$_2$** doped cells increased, mainly due to improved I_{sc} and slightly higher *FF* values. When the content of the dopant molecules is 6.5 m-% or more, the interpenetrating network of the P3HT donor and the $PC_{60}BM$ acceptor molecules is deteriorated. Aggregates in the photoactive layer were visible with an optical microscope. Thus, the efficiency of the cells decreases as the charge transport to the electrodes is limited by high dopant concentrations. The **DPP-(2TPhCN)$_2$**:$PC_{70}BM$ (60:40) cell, where P3HT donor was completely replaced by the **DPP-(2TPhCN)$_2$**, had an efficiency of 0.74 % after optimization experiments. The theoretical maximum efficiency for the cell, with the same donor LUMO and $PC_{60}BM$ acceptor, is ~4 %.[36] The cell V_{oc} was 0.61 V, which corresponds well to the V_{oc} produced by the donors with the same HOMO level.[36] I_{sc} remained low, which limits the cell function the most.

DPP-(2TPhCN)$_2$ dopant molecules broaden the cell absorbance (Figure 4.24a) to the longer wavelengths, which is one possible explanation for the better I_{sc} in the presence of the dopant molecules. In addition, the emission from the doped cells decreased compared to the reference and **DPP-(2TPhCN)$_2$**:$PC_{70}BM$ cells (Figure 4.24b). Because the absorption range of the dopant molecules overlaps with that of P3HT emission, dopant molecules can absorb the emission caused by P3HT, which increases the cell current further.

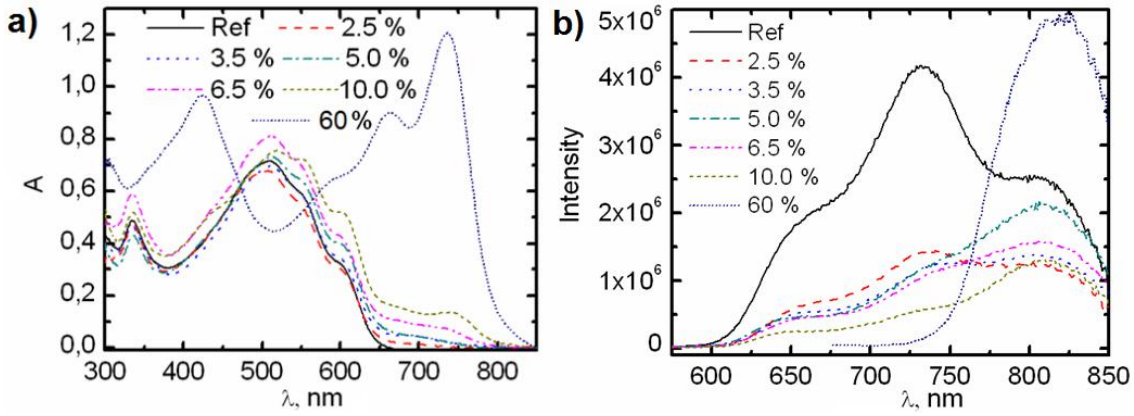

Figure 4.24 Absorption (a) and emission (b) (λ_{ex} = 500 nm) spectra of the P3HT:$PC_{60}BM$ reference cell, the cells doped with **DPP-(2TPhCN)$_2$ (**in m-%) and **DPP-(2TPhCN)$_2$**:$PC_{70}BM$ (60:40) cell (λ_{ex} = 660 nm).[V]

4.3.2.2 Photovoltaic performance of di-(*p*-CNPh)4T doped cells

For comparison, doping with **di-(*p*-CNPh)4T** was carried out in three similar molar ratios (0.7, 1.4 and 2.7) as was the case for **DPP-(2TPhCN)$_2$** (Table 4.14). When **di-(*p*-CNPh)4T** was used as a dopant, only one cell out of ten in the case of 4.8 m-% dopant content had better efficiency than the

reference cell. The average efficiency of the cells doped with **di-(*p*-CNPh)4T** did not improve compared to that of the reference cells, measured one day after the cell preparation.

Table 4.14 The content (2.4 – 4.8 m-%) of **di-(*p*-CNPh)4T** dopant molecules in the photoactive layer of the P3HT:$PC_{60}BM$ reference cell, the corresponding photovoltaic parameters measured one day after the cell preparation and their standard deviations, and those of the **di-(*p*-CNPh)4T**:$PC_{60}BM$ (67:33) cell.[V]

m%	mol%	Number of cells	$I_{sc,\,best}$ (mA/cm^2)	$V_{oc,best}$ (V)	FF_{best} (%)	η_{best} (%)	η_{avg} (%)
0	**0**	7	-2.92 ± 0.27	0.55 ± 0.011	56 ± 7.1	2.84 ± 0.44	2.59
2.4	**0.7**	5	-2.63 ± 0.26	0.54 ± 0.004	57 ± 7.9	2.51 ± 0.04	2.46
3.6	**1.4**	6	-3.48 ± 0.42	0.54 ± 0.005	46 ± 9.5	2.72 ± 0.53	2.49
4.8	**2.7**	10	-3.39 ± 0.29	0.53 ± 0.006	62 ± 5.6	3.46 ± 0.46	2.48
67*	**73**	3	-0.12 ± 0.05	0.67 ±0.000	42 ±16	0.09 ± 0.04	0.07

***di-(*p*-CNPh)4T**:$PC_{60}BM$ (67:33) cell

Table 4.15 The content (2.4 – 4.8 m-%) of **di-(*p*-CNPh)4T** dopant molecules in the photoactive layer of the P3HT:$PC_{60}BM$ reference cell, the corresponding photovoltaic parameters measured one month after the cell preparation and their standard deviations.[V]

m%	mol%	Number of cells	$I_{sc,best}$ (mA/cm^2)	$V_{oc,best}$ (V)	FF_{best} (%)	η_{best} (%)	η_{avg} (%)
0	**0**	7	-2.96 ± 0.25	0.55 ± 0.005	60 ± 4.9	3.01 ± 0.37	2.56
2.4	**0.7**	8	-2.91 ± 0.23	0.54 ± 0.012	57 ± 3.4	2.84 ± 0.14	2.64
3.6	**1.4**	5	-3.05 ± 0.40	0.56 ± 0.009	57 ± 2.8	3.04 ± 0.42	2.64
4.8	**2.7**	9	-3.37 ± 0.28	0.54 ± 0.004	62 ± 5.4	3.50 ± 0.43	2.55

After one month of storage, the average efficiencies of the cells with 2.4 m-% or 3.6 m-% content of **di-(*p*-CNPh)4T** dopant improved slightly compared to that the reference cells (Table 4.15). When **di-(*p*-CNPh)4T** molecules were used as a donor material, replacing P3HT completely, the best efficiency after optimization experiments was 0.09 %. The theoretical maximum efficiency for the cell, with the same donor LUMO level and $PC_{60}BM$ acceptor, is less than 1 %.[36] The cell had a high V_{oc} value, 0.67 V, but the I_{sc} value was only -0.12 mA/cm^2.

Doping with **di-(*p*-CNPh)4T** broadens the cell absorption, when 3.6 m-% of the dopant is used (Figure 4.25a). However, the absorbances of the cells with 2.4 m-% or 4.8 m-% of the dopant decreased compared to that of the reference cell. These differences are due to uneven spreading of the solution during spin-coating. Emission of P3HT is not quenched in the cells doped with **di-(*p*-CNPh)4T** (Figure 4.25b) as in the case of **DPP-(2TPhCN)$_2$** doping. In contrast, the cell emission intensities increase with **di-(*p*-CNPh)4T** doping. This is mainly due to the emission from **di-(*p*-CNPh)4T** as it overlaps with the P3HT emission band (see the 67 % absorption and emission bands in Fig. 4.25).

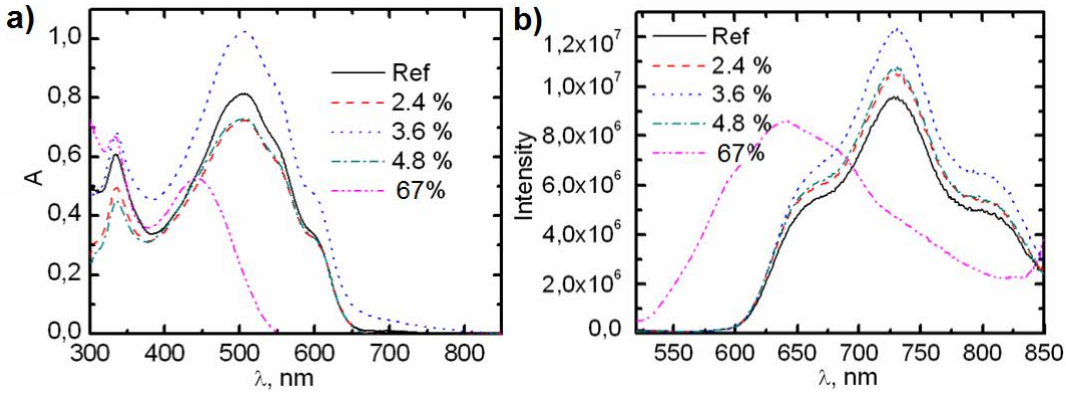

Figure 4.25 Absorption (a) and emission spectra (λ_{ex} =500 nm) (b) of the P3HT:$PC_{60}BM$ cells doped with **di-(*p*-CNPh)4T** and **di-(*p*-CNPh)4T**:$PC_{60}BM$ (67:33) cell (λ_{ex} =450 nm).[V]

4.3.2.3 Spectroscopic studies on the intra- and intermolecular interactions of DPP-$(2TPhCN)_2$ with $PC_{60}BM$

The process of doping the organic solar cells involved the insertion of additional dopant molecules into the solution of photoactive layer components, P3HT and $PC_{60}BM$, and spin coating the solution. After the spin coating, the dopant molecules form a solid BHJ layer with P3HT and $PC_{60}BM$, where the molecules are mixed and in close proximity. Thus, intermolecular interactions, such as energy or electron transfer, are possible between the molecules in solid cell structures. This interaction can be easily observed from the broadened and red shifted absorption and emission spectra of the cells (Figures 4.24 and 4.25) compared to those measured in solution (Figures 4.26 and 4.30). Intra- and intermolecular interactions of **DPP-$(2TPhCN)_2$** and **di-(*p*-CNPh)T4** dopant molecules with P3HT and $PC_{60}BM$ were studied by steady state and time-resolved absorption and fluorescence methods in chloroform solutions.

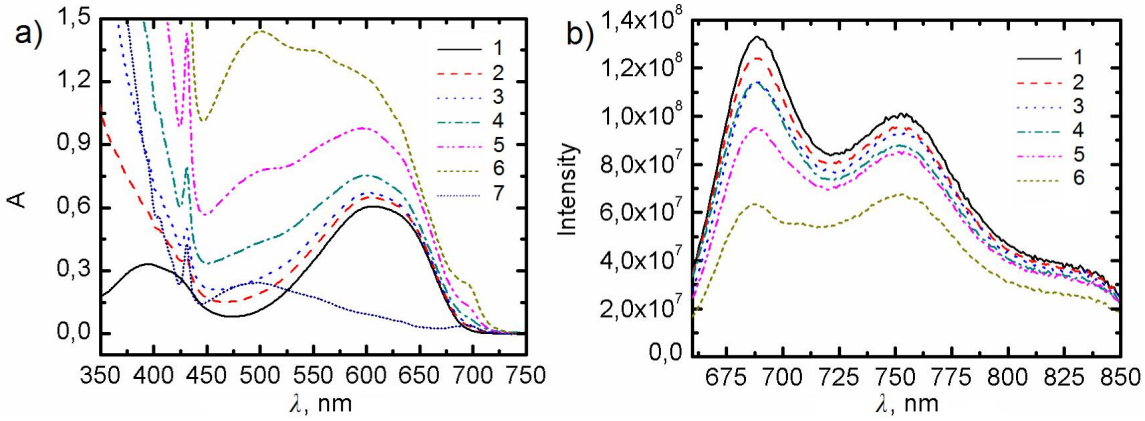

Figure 4.26 Absorption (a) and emission (λ_{ex} = 650 nm) (b) spectra of **DPP-$(2TPhCN)_2$** with the different concentrations of $PC_{60}BM$ in the $CHCl_3$ solutions 1-7. Concentrations of **DPP-$(2TPhCN)_2$** and $PC_{60}BM$ in the solutions 1-7 are shown in Table 14.6.[V]

When 0.12 mM **DPP-$(2TPhCN)_2$** is mixed in chloroform with $PC_{60}BM$ in different concentrations, their combined emission is decreased as a function of the $PC_{60}BM$ concentration as shown in Table 4.16 and Figure 4.26. Also, lifetimes of the single exponential fits of the fluorescence decay curves (Figure 4.26a, Table 4.14) decrease as the $PC_{60}BM$ concentration is increased. The emission of **DPP-$(2TPhCN)_2$** is possibly quenched dynamically by $PC_{60}BM$.[37] The constant for the dynamic

quenching can be determined based on the fluorescence lifetimes as a function of the $PC_{60}BM$ concentration. As $\tau_0/\tau = 1 + K_D[Q]$, K_D is 0.026 $M^{-1}/10^{-3}$ = 26 M^{-1} and the dynamic quenching rate, k_q, is 26 M^{-1}/1.08 ns = 2.40×10^{10} M^{-1} s^{-1}. This value corresponds well with the diffusion controlled rate constant in chloroform. Thus the quenching of **DPP-(2TPhCN)$_2$** with $PC_{60}BM$ is possible, with the energy transfer mechanism.

Table 4.16 Concentrations, absorbances at the excitation wavelength, transmittances at the excitation wavelength, measured and corrected fluorescence emission (λ_{ex} = 650 nm) intensities at 750 nm, and fluorescence lifetimes (λ_{mon} = 690 nm) of **DPP-(2TPhCN)$_2$** and $PC_{60}BM$ solutions 1-7 (Fig. 4.26) in chloroform.[V]

Solution/ Curves	[DPP-(2TPhCN)$_2$] (mM)	[$PC_{60}BM$] (mM)	$A_{(650)}$	$T_{(650)}$ [a]	$I_{(750)}$	$I_{corr(750)}$ [b]	$\tau_{(690)}$ (ns)
1	0.12	-	0.44	0.60	1.00×10^8	2.51×10^8	1.08
2	0.12	0.44	0.47	0.58	9.49×10^7	2.29×10^8	1.07
3	0.12	0.88	0.48	0.57	8.75×10^7	2.05×10^8	1.06
4	0.12	1.76	0.52	0.55	9.23×10^7	2.06×10^8	1.03
5	0.12	3.52	0.67	0.46	8.41×10^7	1.56×10^8	1.00
6	0.12	7.04	0.70	0.45	6.70×10^7	1.21×10^8	0.91
7	-	0.15	0.01	-	-	-	-

[a]Estimated transmittance of the sample solution for the excitation light: $T_{ex} = 10^{(-1/2\times A(650))}$, as the fluorescence intensity is measured in 90 degree angle relative to excitation, [b]Corrected intensity at 750 nm: $I_{corr} = I_{(750)}/(1-T_{ex})$

In the fluorescence lifetime experiments above, the excitation wavelength was 650 nm, where mainly the DPP-core absorbs. The lifetime of the DPP-group only is 7.1 ns[38], but is quenched in the case of **DPP-(2TPhCN)$_2$** due to the two substituted thiophene units, to 1.1 ns. Thus this intramolecular quenching has a rate of 7.9 × 10^8 s^{-1} and the process corresponds to the charge transfer from the thiophene units to the DPP-core.

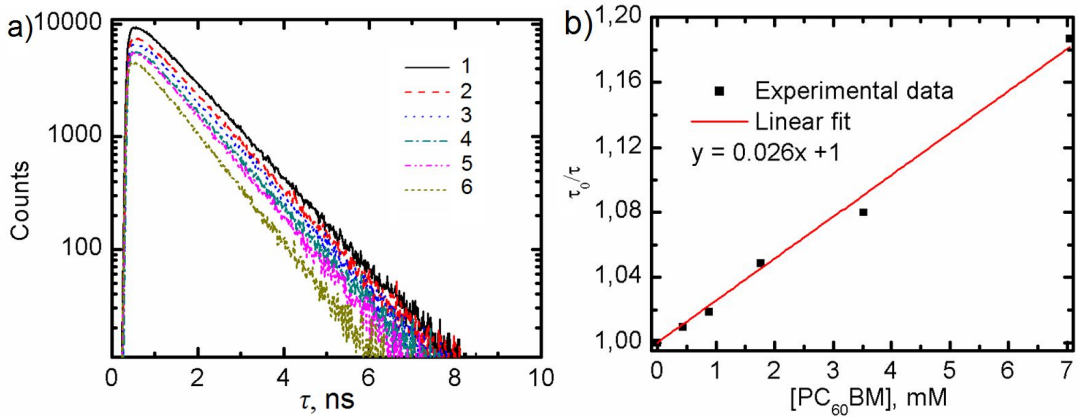

Figure 4.27 Fluorescence decay curves (λ_{ex} = 650 nm, λ_{mon} = 690 nm) and τ_0/τ as a function of $PC_{60}BM$ concentration of the **DPP-(2TPhCN)$_2$** and $PC_{60}BM$ solutions.[V]

To estimate the strength of the **DPP-(2TPhCN)$_2$**/$PC_{60}BM$ interaction, and the possible electron transfer, pump-probe measurements for the **DPP-(2TPhCN)$_2$**/$PC_{60}BM$ system were carried out. The excitation wavelength was 650 nm and only the DPP-moiety was excited. Figure 4.28a presents the sum of the decay component spectra of **DPP-(2TPhCN)$_2$** in chloroform at 0 ps (green curve) and the component spectra with lifetimes of 6.2 ps and 590 ps (blue and red curves) in the visible

wavelength range, and 9.8 ps and 740 ps in the near-infrared range. It is worth noting, that none of the lifetimes observed in the transient absorption experiments corresponds to the fluorescence lifetime (≈ 1.1 ns) measured by the TCSPC method above. A transient state is formed in an average lifetime of 8.0 ps, which can be seen as a bleaching of the **DPP-(2TPhCN)$_2$** ground state (blue triangles) at 550 nm – 650 nm and as a small absorption band at 670 nm. The formed state, with an average lifetime of 660 ps (red circles), is very probably an intramolecular charge transfer state (ICTS), as the electrons transfer from the ICT state of **DPP-(2TPhCN)$_2$**, ($P^{\delta-}T^{\delta+}$), to the cyano-phenyl (C) moiety:

$$(P^{\delta-}T^{\delta+})*C \rightarrow (PT^{\delta+})C^{\delta-}$$

The absorption band of the cation radical ($PT^{\delta+}$) has been observed at the wavelength range of 900 – 1200 nm.[39] The negative amplitudes of the component spectrum at 550 – 700 nm, with the average lifetime of 660 ps, correspond to the recovery of the ground state as the ICT state, with the positive amplitude at 900 – 1100 nm, recombines with the same rate.

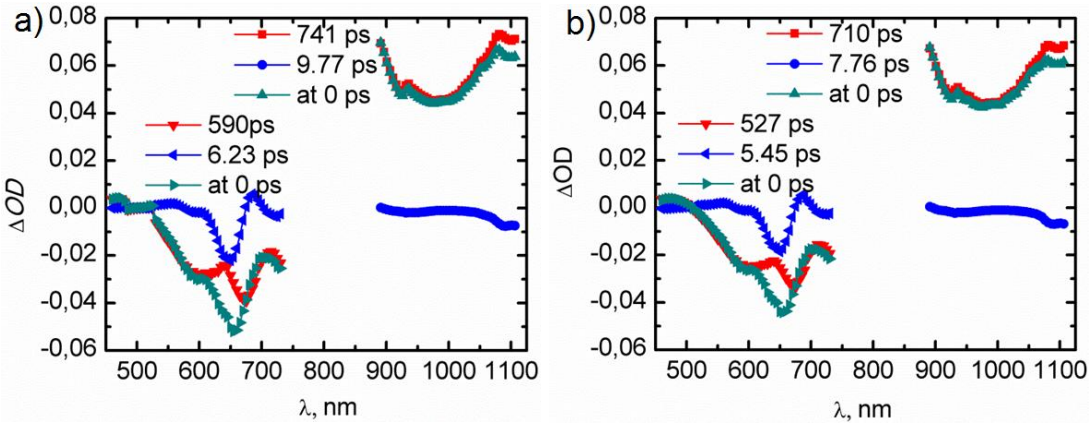

Figure 4.28 Decay component spectra of 0.234 mM **DPP-(2TPhCN)$_2$** in the absence (a) and in the presence (b) of 1.76 mM $PC_{60}BM$ in $CHCl_3$ (λ_{ex} = 650 nm).[V]

In chloroform, in the presence of the $PC_{60}BM$ acceptor (Figure 4.28b), no remarkable changes appear in the spectra. Here, as well, the excitation at 650 nm, pumps the DPP-core, but also $PC_{60}BM$, since the molecule absorbs at the wavelength (Figure. 4.26a). The only small difference between the spectra in Figures 4.28a and 4.28b are the component average lifetimes, 7 ps and 620 ps, which are 5-10 % shorter in the presence of $PC_{60}BM$. The differences in lifetimes can be explained rather by the experimental accuracy than by molecular interactions, because $PC_{60}BM$, at the used experimental concentration, 1.76 mM, can not interact with components of lifetimes < 700 ps. This is also the reason, why no evidences for electron transfer from **DPP-(2TPhCN)$_2$** to $PC_{60}BM$ were observed by the pump probe experiments. Higher concentration of $PC_{60}BM$ could not be used, because $PC_{60}BM$ absorbs at 650, and the sample absorbance exceeds the instrumental limit. Interaction between P3HT and **DPP-(2TPhCN)$_2$** was studied by corresponding steady state and transient absorption measurements. Clear interaction between the molecules was not observed.

Intramolecular charge transfer in **DPP-(2TPhCN)$_2$**, from the thiophenes and DPP-group to the cyanophenyl group, was computed by DFT. Electron density of the HOMO is concentrated on the

thiophenes and DPP-core of the molecule, whereas the LUMO electron density extends to the cyanophenyl groups as well (Figure 4.29 and Table 4.17).

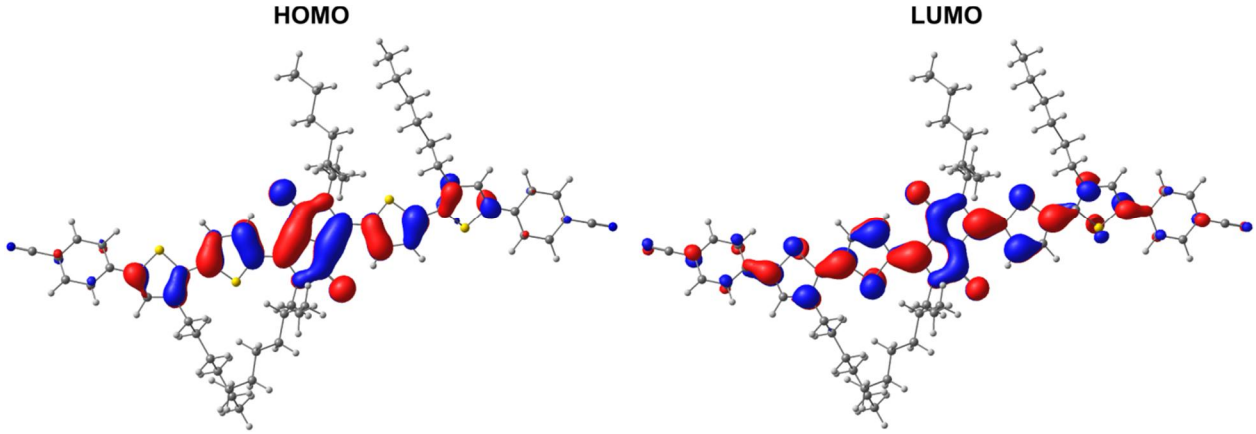

Figure 4.29 Frontier molecular orbitals of **DPP-(2TPhCN)$_2$** calculated at the B3LYP/6-31G** level of theory.[V]

Table 4.17 Contributions (%) of the whole backbone, separate thiophenes and DPP-group, and cyanophenyl end-groups to the HOMO and LUMO of **DPP-(2TPhCN)$_2$**.[V]

HOMO				LUMO			
Backbone (thiophenes+DPP)	**Thiophenes**	**DPP**	**End-groups**	**Backbone (thiophenes+DPP)**	**Thiophenes**	**DPP**	**End-groups**
96.2	42.6	53.6	3.8	91.35	53.41	37.94	8.65

4.3.2.4 Spectroscopic studies on the intra- and intermolecular interactions of di-(*p*-CNPh)4T with $PC_{60}BM$

As the LUMO level of **di-(*p*-CNPh)4T** (-2.62 eV)[IV] is higher than that of $PC_{60}BM$ (-3.7 eV) and **di-(*p*-CNPh)4T** is excited, photoinduced energy or electron transfer is possible from the former to the latter (Figure 4.32). Emission of **di-(*p*-CNPh)4T** is quenched as a function of $PC_{60}BM$ concentration (Figure 4.30 and Table 4.18).

Table 4.18 Concentrations, absorbances at the excitation wavelength, transmittances at the excitation wavelength, measured and corrected fluorescence emission (λ_{ex} = 483 nm) intensities, and fluorescence lifetimes (λ_{mon} = 525 nm) of **di-(*p*-CNPh)4T** and $PC_{60}BM$ solutions 1-7 (Figure 4.30) in chloroform.[V]

Solution/ curves	[di-(p-CNPh)-OT4](mM)	[PCBM] (mM)	$A_{(483)}$	$T_{(483)}$[a]	$A_{(525)}$[b]	$T_{(525)}$	$I_{(525)}$	$I_{corr(525)}$[c]	$\tau_{(525)}$ (ns)
1	0.18	-	0.39	0.64	0.015	0.98	5.81×10^7	9.26×10^7	0.72
2	0.18	0.22	0.41	0.62	0.050	0.92	4.96×10^7	8.70×10^7	0.70
3	0.18	0.44	0.46	0.59	0.086	0.87	4.38×10^7	8.53×10^7	0.69
4	0.18	0.88	0.54	0.54	0.156	0.78	3.33×10^7	7.91×10^7	0.66
5	0.18	1.76	0.64	0.48	0.276	0.64	2.19×10^7	7.13×10^7	0.62
6	0.18	3.52	0.93	0.34	0.532	0.42	8.88×10^6	6.22×10^7	-[d]
7	0.18	7.04	1.57	0.16	1.095	0.17	8.32×10^5	3.06×10^7	-[d]

[a]Estimated transmittance for the excitation light: $T_{(483)} = 10^{(-1/2\times A(483))}$, as the fluorescence intensity is measured in 90 degree angle relative to excitation, [b]Estimated transmittance of the sample for the emission light at 525 nm: $T_{(525)} = 10^{(-1/2\times A(525))}$, [c]Corrected intensity at 525 nm: $I_{corr} = I_{(525)} / (1-(T_{483}\times T_{525})$, [d]Number of counts too small for a reliable fit

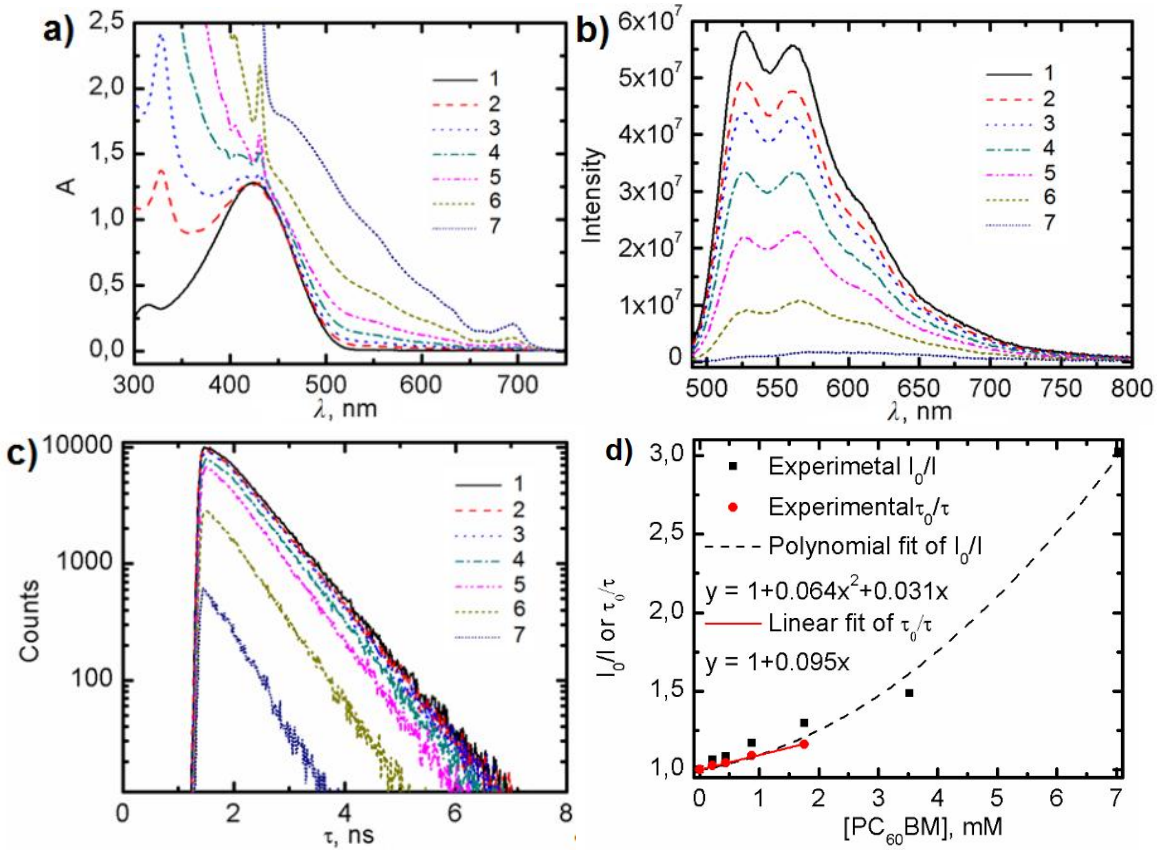

Figure 4.30 Absorption (a) and emission (b) (λ_{ex} = 483 nm) spectra and emission decay curves (λ_{ex} = 483 nm, λ_{mon} = 525 nm) (c) and Stern-Volmer plot (d) of **di-(*p*-CNPh)4T** with different concentrations of $PC_{60}BM$ (concentrations shown in Table 4.18).[V]

As the emission decay curves (Figure 4.30c) show, lifetimes of single exponential fits decrease in the presence of $PC_{60}BM$. The quenching of **di-(*p*-CNPh)4T** could be both static and dynamic[37] in the presence of $PC_{60}BM$, as the increase in I_0/I is exponential as a function of $PC_{60}BM$ concentration (Figure 4.30d).

In order to investigate the kinetics, pump-probe measurements were carried out. The excitation wavelength, 483 nm, corresponds to the thiophene absorption band. Figure 4.31a presents the sum of the decay component spectra of **di-(*p*-CNPh)4T** in chloroform at 0 ps (green curve) and the component spectra with lifetimes of 1.0 – 5.1 ps (blue curves) and 700 – 920 ps (red curves). The first decay component (1.0 – 5.1 ps, blue triangles) could be an ICT state as electrons spread from the quaterthiophene backbone to the aryl group forming a quaterthiophene cation, analogically to the the sexithiophene ($6T^{+}$) cation, which absorbs[40] around 800 nm, or the sexithiophene dication ($6T^{2+}$), which absorbs[41] at 940 nm. The second component (τ = 707 – 923 ps, red circles) shows the decay of the ICT back to the ground state. The lifetime of the ICT state is consistent with the singlet excited state lifetime of 0.72 ns measured for **di-(*p*-CNPh)4T** by TCSPC.

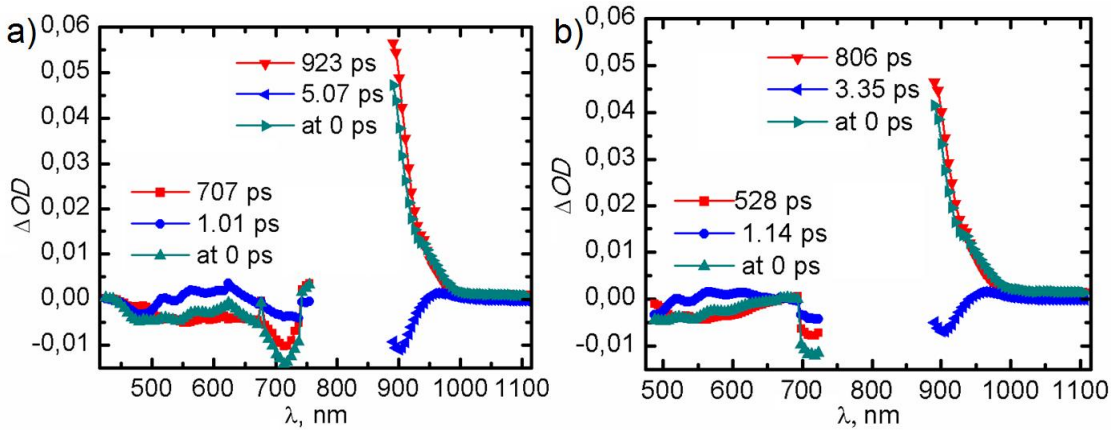

Figure 4.31 Decay component spectra of 0.355 mM **di-(*p*-CNPh)4T** in the absence (a) and in the presence (b) of 1.76 mM $PC_{60}BM$ in $CHCl_3$ (λ_{ex} = 483 nm).[V]

In the presence of $PC_{60}BM$, the decay component spectra of **di-(*p*-CNPh)4T** do not show changes in the absorption peak positions, but the lifetimes are slightly decreased. The decrease in the lifetimes is consistent with the results of TCSPC measurements in the presence of $PC_{60}BM$. Thus, energy transfer between the molecules is very likely in chloroform solution. Interaction between P3HT and **di-(*p*-CNPh)4T** was studied by steady state and transient absorption measurements. Clear interaction between the molecules was not observed.

To summarize, **DPP-(2TPhCN)$_2$** and **di-(p-CNPh)4T** dopant molecules absorb light and donate energy to $PC_{60}BM$, which increased the cell current. Since the LUMO levels of the dopants are higher than that of $PC_{60}BM$ (Figure 4.32), electron transfer from the dopants to $PC_{60}BM$ could be possible, but it was not observed in the experiments. The absorption of the **DPP-(2TPhCN)$_2$** dopant molecules covers wider wavelength region than that of **di-(p-CNPh)4T**. Therefore, **DPP-(2TPhCN)$_2$** doping increases the cell current and efficiency more than **di-(p-CNPh)4T** doping.

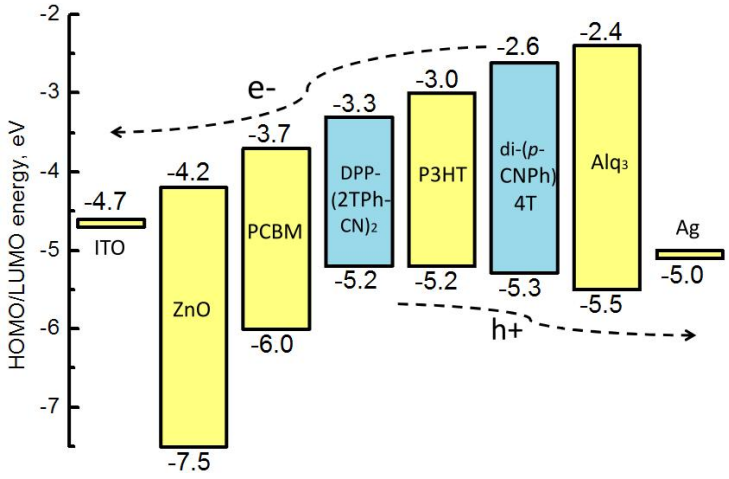

Figure 4.32 Energy levels of the inverted cell structure (yellow) and the used dopant molecules **DPP-(2TPhCN)$_2$** and **di-(*p*-CNPh)4T** (blue). Direction of the electron and hole transport is shown by arrows.[V]

5 Conclusions

Organometallic n-type 5-amino substituted Alq_3 derivatives, p-type aryl end-capped quaterthiophenes and a combined p- and n-type Alq_3 end-capped hexathiophene were tested as anodic hole transporting buffer layers in the inverted cell structure. The use of the buffer materials aimed to better charge transport and efficiency of the cell. An ideal energy level alignment of the buffer material with the adjacent photoactive layer and metal anode increased the cell I_{sc} values significantly. Photoactivity of the buffer layer was considered if the buffer material absorption matches with the solar emission spectrum. In this case, energy or electron transfer from the buffer layer to the photoactive layer possibly increases the cell current more. Continuous electron density of the molecular orbitals, HOMO and LUMO, promoted to an efficient exciton or charge transfer in the buffer layer.

Conjugated donor-acceptor copolymers were tested as donor molecules in the organic solar cells with $PC_{60}BM$ and $PC_{70}BM$ acceptors. The benzodithiophene-benzotriazole copolymer performed better as donor material than the fluorine-benzotriazole copolymers. The polymers molecular geometries, energy levels, molecular orbitals and the effect of their interaction with the acceptor molecule on the energy levels were calculated with DFT. Based on the calculations, bulky side groups in the polymer structures of the fluorine-benzotriazole copolymers caused steric hindrance and twisting or bending of the backbone. As a result, the electron density is concentrated in parts of the polymer structure and π-conjugation is weakened or broken. As the delocalization does not cover the whole polymer structure, excitons or charges are trapped in the gaps of the discontinuous molecular orbitals and I_{sc} remains low. Energy levels of the donor and acceptor materials change due to their electronic interactions. The cell with benzodithiophene-benzotriazole copolymer produced a different V_{oc} depending on the used acceptor material, $PC_{60}BM$ or $PC_{70}BM$. A correlation between the increased V_{oc} values and changes of the energy levels was found, when the donor and acceptor are positioned close to each other in a computational model.

Alq_3, aryl and 8-phenoxyquinoline end-capped oligothiophenes were used as dopant materials in the P3HT:$PC_{60}BM$ BHJ photoactive layer. Based on the results of the solar cell experiments and spectroscopic and electrochemical studies, the dopant molecules function as additional light-absorbers in the photoactive layer. In the ternary blend of the dopant, P3HT and $PC_{60}BM$ molecules intermolecular interactions are likely. To better understand the function of the dopant molecules in the cell, solution studies on the interaction of the dopant molecules with P3HT and $PC_{60}BM$ were carried out using steady state and time resolved optical spectroscopic methods. The observed photoinduced energy or electron transfer reactions from the dopant molecules to $PC_{60}BM$ most likely improve the cell current and power conversion efficiency. If the dopant molecule absorbs at the near IR region, the cell absorbance broadened and the cell current further increased. The improvements in the efficiencies of the doped cells were partly due to advantageous morphological changes in the photoactive layer, which raised the absorbance and improved the charge transport properties of the photoactive layer.

6 References

[1] *Statistical Review of World Energy 2013*, 62nd edition of the BP Statistical Review of World Energy, **2013**, http://www.bp.com/en/global/corporate/about-bp/energy-economics/statistical-review-of-world-energy-2013.html.

[2] *Basic Research Needs for Solar Energy Utilization*, **2005**, The U. S. Department of Energy (DOE) Office of Basic Energy Sciences, http://science.energy.gov/~/media/bes/pdf/reports/files/seu_rpt.pdf.

[3] J. Matthew Roney, *World Solar Power Topped 100,000 Megawatts in 2012*, **2013**, Earth Policy Institute, http://www.earth-policy.org/indicators/C47/solar_power_2013.

[4] M. Peach, *Heliatek achieves 12 % organic solar cell efficiency*, 23 January **2013**, http://optics.org/news/4/1/36.

[5] a) T. S. van der Poll, J. A. Love, T.-Q. Nguyen and G. C. Bazan, *Adv. Mater.* **2012**, 24, 3646 – 3649; b) Y. M. Sun, G. C. Welch, W. L. Leong, C. J. Tacaks, G. C. Bazan, and A. J. Heeger, *Nat. Mater.* **2012**, 11, 44 – 48; c) Z. Li, G. He, X. Wan, Y. Liu, J. Zhou, G. Long, Y. Zuo, M. Zhang and Y. Chen, *Adv. Energy Mater.* **2012**, 2, 74 – 77.

[6] a) X. Li1, W. C. H. Choy, L. Huo, F. Xie, W. E. I. Sha, B. Ding, X. Guo, Y. Li, J. Hou, J. You and Y. Yang, *Adv. Mater.* **2012**, 24, 3046 – 3052; b) L. T. Dou, J. B. You, J. Yang, C.-C. Chen, Y. J. He, S. Murase, T. Moriarty, K. Emery, G. Li and Y. Yang, *Nat. Photonics*, **2012**, 6, 180 – 185; c) H. Y. Chen, J. H. Hou, S. Q. Zhang, Y. Y. Liang, G. W. Yang, Y. Yang, L. P. Yu, Y. Wu and G. Li, *Natur. Photonics*, **2009**, 3, 649 – 653.

[7] V. Gupta, A. K. K. Kyaw, D. H. Wang, S. Chand, G. C. Bazan and A. J. Heeger, *Scientific Reports*, **2013**, 3, Article number: 1969.

[8] M. S. White, D. C. Olson, S. E. Shaneen, N. Kopidakis and D. S. Ginley, *Appl. Phys. Lett.* **2006**, 89, 143517.

[9] HOMO and LUMO levels of ZnO, PHT and PCBM, see: a) A. K. K. Kyaw, X. W. Sun, C. Y. Jiang, G. Q. Lo and D. W. Zhao, *Appl. Phys. Lett.* **2008**, 93, 221107; Work function of Au, see: b) E. Ito, Y. Washizu, N. Hayashi, H. Ishii, N. Matsuie, K. Tsuboi and Y. Ouchi, *J. Appl. Phys.* 92, **2002**, 12, 7306 – 7310.

[10] Paul D. Cunningham, *Optical pump terahertz probe studies of semiconducting polymers*, Doctoral Thesis/Dissertation, University of Maryland, **2010**, 258 pages.

[11] *American Society for Testing and Materials (ASTM) Terrestrial Reference Spectra for Photovoltaic Performance Evaluation*, http://rredc.nrel.gov/solar/spectra/am1.5/.

[12] M.-S. Kim, B.-G. Kim, and J. Kim, *ACS Appl. Mater. Interfaces*, **2009**, 1(6), 1264 – 1269.

[13] C. W. Tang and VanSlyke, *Appl. Phys. Lett.* **1987**, 51 (12), 913 – 915.

[14] a) C. Perez-Bolivar, S. Takizawa, G. Nishimura, V. A. Montes, P. Anzenbacher Jr., *Chem. Eur. J.* **2011**, 17, 9076 – 9082; b) W. A. E. Omar, H. Haverinen and O. E. O. Hormi, *Tetrahedron*, **2009**, 65, 9707 – 9712; c) J. P. Heiskanen, A. E. Tolkki, H. J. Lemmetyinen and O. E. O. Hormi, *J. Mater. Chem.* **2011**, 21, 14766 – 14775.

[15] a) Y.-K. Han and S. U. Lee, *Chem. Phys. Lett*. **2002**, 366, 9 – 16; b) V. A. Montes, R. Pohl, J. Shinar, and P. Anzenbacher Jr., *Chem. Eur. J*. **2006**, 12, 4523 – 4535.

[16] C. Hansch, A. Leo and R. W. Taft, *Chem. Rev.* **1991**, 91, 165 – 195.

[17] a) J. Hou, M.-H. Park, S. Zhang, Y. Yao, L.-M. Chen, J.-H. Li and Y. Yang, *Macromolecules*, **2008**, 41, 6012 – 6018; b) J. Hou, H.-Y. Chen, S. Zhang, R. I. Chen, Y. Yang, Y. Wu and G. Li, *J. Am. Chem. Soc.* **2009**, 131, 15586 – 15587; c) Y. Zhang, S. K. Hau, H.-L. Yip, Y. Sun, O. Acton and A. K.-Y. Jen, *Chem. Mater.* **2010**, 22 (9), 2696 – 2698; d) S. C. Price, A. C. Stuart and W. You, *Macromolecules*, **2010**, 43, 4609 – 4612; e) Q. Shi, H. Fan, Y. Liu, J. Chen, L. Ma, W. Hu, Z. Shuai, Y. Li and X. Zhan, *Macromolecules*, **2011**, 44, 423 – 4240; f) L. Dou, J. Gao, E. Richards, J. You, C.-C. Chen, K. C. Cha, Y. He, G. Li, and Y. Yang, *J. Am. Chem. Soc.* **2012**, 134, 10071 – 10079; g) B. Äich, J. Lu, S. Beaupré, M. Leclerc and Y. Tao, *Org. Electron.* **2012**, 13, 1736 – 1741.

[18] a) H. Wettach, F. Pasker, and S. Höger, *Macromolecules*, **2008**, 41, 951 – 9515; b) L. Zhang, C. He, J. Chen, P. Yuan, L. Huang, C. Zhang, W. Cai, Z. Liu and Y. Cao, *Macromolecules*, **2010**, 43, 9771 – 9778; c) B. Peng, A. Najari, B. Liu, P. Perrouard, D. Gendron, Y. He, K. Zhou, M. Leclerc and Y. Zou, *Macromol. Chem. Phys*. **2010**, 211, 2026 – 2033; d) J. Min, Z.-G. Zhang, S. Zhang, M. Zhang, J. Zhang and Y. Li, *Macromolecules*, **2011**, 44, 7632 – 7638.

[19] a) S. C. Price, A. C. Stuart, L. Yang, H. Zhou and W. You, *J. Am. Chem. Soc.* **2011**, 133, 4625 – 4631; b) Z. Zhang, B. Peng, B. Liu, C. Pan, Y. Li, Y. He, K. Zhou and Y. Zou, *Polym. Chem.* **2010**, 1, 1441 – 1447.

[20] Y. Chen, H. Tian, Y. Geng, J. Geng, D. Ma, D. Yan, and L. Wang, *J. Mater. Chem.* **2011**, 21, 15332 – 15336.

[21] M. Melucci, L. Favaretto, M. Zambianchi, M. Durso, M. Gazzano, A. Zanelli, M. Monari, M. G. Lobello, F. De Angelis, V. Biondo, G. Generali, S, Troisi, W. Koopman, S. Toffanin, R. Capelli and M. Muccini, *Chem. Mater.* **2013**, 25, 668 – 676.

[22] I. Imae, S. Imabayashi, K. Komaguchi, Z. Tan, Y. Ooyama and Y. Harima, *RSC Adv.* **2014**, 4, 2501 – 2508.

[23] a) F. Zhang, D. Wu, Y. Xu, X. Feng, *J. Mater. Chem.* **2011**, 21, 17590 – 17600; b) A. Mishra and P. Bäuerle, *Angew. Chem. Int. Ed.* **2012**, 51, 2020 – 2067.

[24] M. T. Tang, L. Hirsch and G. Wantz, *Adv. Mater.* **2011**, 23, 3597 – 3602.

[25] M. Niemi, *Photoinduced Electron Transfer in Dyads and Triads of Porphyrins, Phthalocyanines and fullerenes*, Doctoral Thesis, Tampere University of Technology, **2008**, 51 pages.

[26] N. V. Tkachenko: *Optical Spectroscopy Methods and Instrumentations*, Elsevier, Amsterdam **2006**.

[27] R. R. Gagne, C. A. Koval, G. C. Lisensky, *Inorg. Chem.* **1980**, 19, 2854 – 2855.

[28] S. Gutmann, M. Conrad, M. A. Wolak, M. M. Beerbom and R. Schlaf, *J. Appl. Phys.* **2012**, 111, 123710.

[29] W. Tress, K. Leo, M. Riede, *Adv. Funct. Mater.* **2011**, 21, 2140 – 2149.

[30] A. Tolkki, K. Kaunisto, J. P. Heiskanen, W. A. E. Omar, K. Huttunen, S. Lehtimäki, O. E. O. Hormi, H. Lemmetyinen, *Thin Solid Films*, **2012**, 520, 4475 – 4481.

[31] F. M. Pasker, M. F. G. Klein, M. Sanyal, E. Barrena, U. Lemmer, A. Colsmann and S. Höger, *J.Pol. Sci. A: Pol. Chem.*, **2011**, 49, 5001 – 5011.

[32] P. Boland, S. S. Sunkavali, S. Chennuri, K. Foe, T. Abdel-Fattah and G. Namkoong, *Thin Solid Films*, **2010**, 518, 1728 – 1731.

[33] R. A. J. Janssen, M. P. T. Christiaans, K. Pakbaz, D. Moses, J. C. Hummelen and N. S. Saricifti, *J. Chem. Phys.* **1995**, 102 , 2628.

[34] C. Ganzorig and M. Fujihira, *Appl. Phys. Lett.* **2002**, 81, 3137.

[35] (a) S. Watanabe, A. Furube and R. Katoh, *J. Phys. Chem. A*, **2006**, 110, 10173. (b) S. Watanabe, M. Murai, Y. Tamaki, A. Furube and R. Katoh, *Prog. Int. Symp. Super-Functionality Organic Devises: IPAP Conf. Series 6*, **2005**, pp. 121.

[36] M. C. Schaper, D. Mühlbacher, M. Koppe, P. Denk, C. Waldauf, A. J. Heeger, C. J. Brabec, *Adv. Mater.* **2006**, 18, 789 – 794.

[37] J. R. Lakowicz, *Principles of fluorescence spectroscopy 3rd ed*. **2006**, University of Maryland School of Medicine, 953 pages.

[38] M. Eschle, Photochemical and Photophysical properties of diketopyrrolopyrrole organic pigments, Lausanne: EPFL, Theses N° 1616, 1997, 130 pages.

[39] B. P. Karsten, R. K. M. Bouwer, J. C. Hummelen, R. M. Williams and R. A. J. Janssen, *Photochem. Photobiol. Sci.*, 2010, **9**, 1055 – 1065.

[40] a) V. Wintgens, P. Valat and F. Garnier, *J. Phys. Chem.* **1994**, 98, 228 – 232.

[41] R. A. J. Janssen, L. Smilowitz. N. S. Sariciftci and D. Moses, *J. Chem. Phys*, **1995**, 101 (3), 1787.

Publication I

Synthesis and characterization of tris-(5-amino-8-hydroxyquinoline)aluminum complexes and their use as anode buffer layers in inverted organic solar cells

Venla M. Manninen, Walaa A. E. Omar, Juha P. Heiskanen, Helge J. Lemmetyinen and Osmo E. O. Hormi

J. Mater. Chem., **2012**, 22, 22971 – 22982.

Journal of
Materials Chemistry

Cite this: J. Mater. Chem., 2012, 22, 22971

www.rsc.org/materials

PAPER

Synthesis and characterization of tris-(5-amino-8-hydroxyquinoline) aluminum complexes and their use as anode buffer layers in inverted organic solar cells†

Venla M. Manninen,*[a] Walaa A. E. Omar,[bc] Juha P. Heiskanen,[a] Helge J. Lemmetyinen[a] and Osmo E. O. Hormi[b]

Received 7th August 2012, Accepted 13th September 2012
DOI: 10.1039/c2jm35292c

Tris-(8-hydroxyquinoline)aluminum (Alq_3) and its derivatives have been studied as light-emitting materials in organic light emitting diodes (OLEDs) and recently also as buffer layer materials in inverted organic solar cells based on the well-known bulk-heterojunction (BHJ) of poly(3-hexylthiophene) (P3HT) and C_{61}-butyric acid methyl ester (PCBM). Due to the positions of the highest occupied molecular orbital (HOMO) energy levels of P3HT and Alq_3, an extraction barrier for the photogenerated holes to escape the device is created. To reduce the height of the barrier, the position of the Al-complex HOMO level can be elevated by attaching different substituents on the 8-hydroxyquinoline ligand. In this study three new tris-(5-amino-8-hydroxyquinoline)aluminum complexes with electron donating amino substituents were synthesized, characterized and used as anode buffer layers in inverted organic solar cells. Results of the performed spectroscopic and electrochemical studies confirmed that 5-amino substitution of the hydroxyquinoline ligand is directly correlated with the position of HOMO levels in the complexes while lowest unoccupied molecular orbital (LUMO) levels remained unaffected. Although the complexes exhibit extremely low emission properties compared to the parent Alq_3, they performed nicely as charge transporting buffer layers between the photoactive layer and the gold anode in the organic solar cells.

1. Introduction

Alq_3 is an organometallic complex consisting of three 8-hydroxyquinoline ligands coordinated to aluminum. By attaching different electron-withdrawing or -donating substituents on the 8-hydroxyquinoline ligands, the properties of the complex, such as solubility, emission wavelength, and HOMO and LUMO energy levels, can be modified. Therefore, Alq_3 derivatives have become an interesting research target for different organic electronic applications. The parent Alq_3 has been studied as an electron-transporting and light emitting material since Tang and VanSlyke reported[1] for the first time on the use of Alq_3 in organic light emitting diodes (OLEDs). Recently, the possibilities of applying Alq_3 as a buffer layer in organic solar cells have been investigated. As a buffer layer, Alq_3 is believed to obstruct the permeation of oxygen and moisture into the photoactive layer, thus increasing the stability and lifetime of the organic solar cells.[2] A layered organic solar cell with Alq_3/Au as a cathode showed a 60-fold enhancement in efficiency, from 0.01% to 0.60%, compared to a cell without Alq_3.[3]

Studies have shown that chemical tailoring of the ligand backbone can produce Alq_3 derivatives, which can exhibit tremendously higher photoluminescence (PL) quantum yields and better electroluminescence properties compared to the parent Alq_3.[4] In addition, an inverted organic solar cell equipped with the Alq_3 derivative, tris-(4-pyrazolyl-8-hydroxyl-quinoline) aluminum, as an anode buffer layer showed more than 30% improvement in the efficiency compared to that with the parent Alq_3 as a buffer layer.[5]

In the Alq_3 complex, the highest HOMO electron density is allocated on the 5-position of the 8-hydroxyquinoline ligand and the nature of the substituent attached to this position affects the properties of the resulting complex through modification of its HOMO level.[6] The studied derivatives have electron-donating amino substituents,[7] which are supposed to ease the oxidation of the complexes and to elevate the HOMO energy levels compared to the parent Alq_3.

In organic solar cells the energy levels of the different materials in the layered solar cell structure determine the open circuit

[a]*Department of Chemistry and Bioengineering, Tampere University of Technology, P.O. Box 541, FI-33101, Tampere, Finland. E-mail: venla.manninen@tut.fi; Fax: +358 3 3115 2108*
[b]*Department of Chemistry, University of Oulu, P.O. Box 3000, FI-90014, Finland*
[c]*Department of Science and Mathematics, Faculty of Petroleum and Mining Engineering, Suez Canal University, Suez 43721, Egypt*
† Electronic supplementary information (ESI) available: ^1H and ^{13}C NMR spectra, solid film thickness determination. See DOI: 10.1039/c2jm35292c

voltage (V_{OC}) and have an effect on the fill factor (FF) and short circuit current (I_{sc}). In the used indium tin oxide (ITO)|zinc oxide (ZnO)|P3HT:PCBM|Alq_3|Au inverted solar cell structure, Alq_3 functions as an anode buffer layer between the photoactive P3HT:PCBM BHJ layer and the metal anode. If the HOMO energy level of the P3HT donor lies more than 0.2 eV higher than the HOMO of the buffer layer, an extraction barrier is created at the interface and the FF decreases.[8] An extraction barrier denotes an energetic barrier for the photogenerated holes in the donor to escape the device. By elevating the HOMO level of the buffer material compared to that of the parent Alq_3, the extraction barrier between P3HT and the buffer material can be reduced, which is supposed to improve the FF. Therefore, 5-amino substituted Alq_3 derivatives are interesting candidates for anode buffer layer materials in organic solar cells.

In order to study the properties of 5-amino substituted Alq_3 derivatives and the possibility of applying them in organic solar cells, a synthetic method to produce these target compounds had to be developed. Hartwig–Buchwald (H–B) coupling reaction is currently a widely used method to form arylamines. On the other hand, there are only a few literature references about H–B couplings between quinoline substrates and amines,[9] even though many aminoquinolines have shown remarkable pharmaceutical properties in the treatment of Alzheimer's disease and further potential as antimalarial agents.[9f,10] Amination of quinoline rings has turned out to be somewhat problematic and moreover, the catalytic systems vary from one substrate to another and from one amine to another. Such variations in the reaction conditions create a need for more investigation of different catalytic systems with different substrates and amines. Optimization and screening of the reaction conditions become a prerequisite for any type of Pd catalyzed amination reaction.

In this paper, the effect of three commercially available phosphine ligands in the H–B amination of 8-(benzyloxy)-5-bromoquinoline with three secondary amines was studied to prepare 5-amino-8-benzyloxyquinoline derivatives. It was observed that β-hydrogen elimination competes severely with reductive elimination if reaction conditions have not been optimized carefully. The benzyloxy protecting group at the 8-position tolerated the strong basic medium needed in the H–B amination and could be removed smoothly after the reaction by catalytic hydrogenation affording the corresponding 8-hydroxyquinoline derivatives. The synthesized 5-amino-8-hydroxyquinolines were complexed with Al^{3+} to form three new Alq_3 derivatives. The synthetic work was then followed by extensive studies of the photophysical, electrochemical and thermodynamic properties of the new Alq_3 derivatives and their use as anode buffer layers in organic solar cells.

2. Results and discussion

2.1 Synthesis

Three 5-amino substituted Alq_3 derivatives have been prepared in this work in order to study their photophysical characteristics and their behavior as buffer layers in organic solar cells. The preparation of the new Alq_3 derivatives started from commercially available 5-bromo-8-hydroxyquinoline **1** by protecting the hydroxyl group at the 8-position with the benzyloxy group

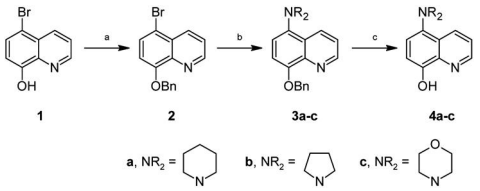

Scheme 1 *Reagents and conditions*: (a) BnBr, K_2CO_3, DMF, rt, 1 h; (b) $Pd(OAc)_2$, ligand **L1**, **L2** or **L3**, NaO-*t*-Bu (1.25 equiv.), amine (1.25 equiv.), toluene, 80–100 °C, 0.5–24 h; (c) Pd–C (10 wt%), H_2, ethanol, reflux, 3 h.

(Scheme 1).[11] After that, the Hartwig–Buchwald coupling was carried out between 8-(benzyloxy)-5-bromoquinoline **2** and amine.

For the Hartwig–Buchwald amination, optimization of the reaction conditions was mandatory. Three phosphine ligands were considered in our preliminary tests in the H–B amination along with palladium acetate as the palladium source. Palladium acetate has served as a stable effective palladium source in the Pd catalyzed aminations[12] while electron rich, sterically demanding ligands proved to be active in many H–B aminations.[9c,12,13] The activities of such ligands are attributed to a combination of steric and electronic factors. Among the active ligands reported in the H–B amination are tri-*tert*-butylphosphine (TTBP) **L1**,[14] di-*tert*-butylneopentylphosphine (DTBNpP)[13,15] **L2**, and (2-biphenyl)di-*tert*-butylphosphine (Johnphos)[12a] **L3** (Fig. 1). Ligands **L1** and **L2** were used as their air stable tetrafluoroborate salts. Piperidine was used as a coupling partner and sodium *tert*-butoxide as a base in the preliminary tests. Both *N*,*N*-dimethylacetamide (DMA) and toluene were tested as solvents in the amination reaction. During the optimization (Table 1), ^{1}H NMR analysis of the crude reaction mixtures revealed that the main side product of this amination reaction was 8-(benzyloxy)quinoline, which is the reduction product of compound **2**. Hartwig *et al.*[16] stated that the arene *versus* amine ratio is controlled by electronic and steric factors of the intermediate complex and that the formation of the arene along with the amine is attributed to the competitive reductive elimination of the amine and the β-hydrogen elimination from the amido aryl intermediate during the reaction.

Experiments showed considerable difference in reaction outcome between toluene and DMA (Table 1, entries 1 and 2). Clearly, the reduction of the starting material is a more favored process in DMA than in toluene. Among the tested ligands, **L2** was the most effective ligand in the H–B amination of compound **2** with piperidine, producing 8-(benzyloxy)-5-(piperidin-1-yl) quinoline **3a** in a high yield (entry 6). The catalyst ligand ratio 1 : 2 was proved to improve the amine : arene ratio and allowed the complete conversion at lower Pd loading (Table 1, entries 3, 4, and 6). Closely related to the present work, it is interesting to

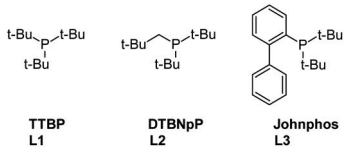

Fig. 1 The ligands used in the optimization of H–B amination reaction of compound **2**.

Table 1 Pd catalyzed amination of 8-(benzyloxy)-5-bromoquinoline **2** with piperidine[a]

Entry	Lig.	Pd/Lig.	Pd cont. (mol%)	Solvent	*t* (h)	Start (%)	Red. prod.(%)	Prod. **3a** (%)
1	**L1**	1/1	5	DMA	4	12	36	52
2	**L1**	1/1	5	Tol.	24	25	12	63
3	**L2**	1/1	5	Tol.	24	5	7	88
4	**L2**	1/1	8	Tol.	24	0	6	94
5	**L3**	1/1	8	Tol.	24	5	11	84
6	**L2**	1/2	5	Tol.	24	0	3	97 (84)[b]

[a] *Reaction conditions*: 50–250 mg of 5-bromo-8-benzyloxyquinoline, $Pd(OAc)_2$, NaO-*t*-Bu (1.25 equiv.), amine (1.25 equiv.), 100 °C, under argon atmosphere. The percentages were analyzed based on ^{1}H NMR from the crude reaction mixtures after the reaction time mentioned. [b] Isolated yield.

note that Hamann *et al.* observed a very low yield (4%) of 8-methoxy-5-(piperidin-1-yl)quinoline during the amination of 5-bromo-8-methoxyquinoline with piperidine at 120 °C, using the $Pd_2(dba)_3$/PPFA catalytic system.[9a] The use of microwave heating improved the yield to a moderate level (46%). Both the methoxy and benzyloxy substituents are electron-donating groups and thus deactivate the quinoline ring and hinder the oxidative addition to palladium, but in our case the used catalyst system is powerful enough to perform the coupling affording the products in high yields and without need for microwave assistance.

During the coupling of compound **2** with pyrrolidine using **L2**, although there was a complete conversion of the starting materials to products, the formation of the reduction product was observed noticeably along with the desired amination product (Table 2, entry 2). Therefore, the effect of **L1** and **L3** was also investigated under same conditions. Similarly to the coupling between compound **2** and piperidine, **L1** did not afford complete conversion and, surprisingly, the reduced product was the main reaction product (Table 2, entry 1). The experiment with ligand **L3** was successful giving a complete conversion and affording the amination product, 8-(benzyloxy)-5-(pyrrolidin-1-yl)quinoline **3b**, in high yield (Table 2, entry 3). Moreover, during the coupling of compound **2** with pyrrolidine, the reaction proceeded faster (30 minutes) and at lower temperature. In contrast to our result, ligand **L3** was previously observed to be uneffective in the H–B amination of halogenated quinoline derivatives.[9c,f]

In the third amination reaction, morpholine was employed as the amine under the same reaction conditions (Table 3). Both **L1** and **L2** showed incomplete conversion of the starting material to product (Table 3, entries 1 and 2). When **L3** was used under the same reaction conditions, the complete conversion was observed and the coupling product, 4-(8-(benzyloxy)quinolin-5-yl)morpholine **3c**, was formed in a high yield (Table 3, entry 3). The

Table 2 Pd catalysed amination of 8-(benzyloxy)-5-bromoquinoline with pyrrolidine[a]

Entry	Lig.	Start (%)	Red. prod. (%)	Prod. **3b** (%)
1	**L1**	44	40	16[b]
2	**L2**	0	43	57[c]
3	**L3**	0	16	84[c] (80)[d]

[a] *Reaction conditions*: 50 mg of **2**, $Pd(OAc)_2$ (5 mol%), ligand (10 mol%), NaO-*t*-Bu (1.25 equiv.), amine (1.25 equiv.), toluene, 80 °C. The resulting percentages were analyzed based on ^{1}H NMR from crude reaction after the reaction time. [b] Reaction time was 3 h under argon. [c] Reaction time 30 min. [d] Isolated yield.

Table 3 Pd catalyzed amination of 8-(benzyloxy)-5-bromoquinoline with morpholine[a]

Entry	Lig.	Start (%)	Red. prod. (%)	Prod. **3c** (%)
1	**L1**	56	9	35
2	**L2**	35	10	55
3	**L3**	0	14	86 (84)[b]

[a] *Reaction conditions*: 50 mg of compound **2**, $Pd(OAc)_2$ (5 mol%), ligand (10 mol%), NaO-*t*-Bu (1.25 equiv.), amine (1.25 equiv.), toluene, 80 °C for 3 h under argon. The resulting percentages were analyzed based on ^{1}H NMR from crude reaction after the reaction time. [b] Isolated yield.

amination with morpholine took place at 100 °C and lasted for 3 hours.

Hill *et al.*[13] stated that the optimal cone angle for the effective ligand in the H–B reactions falls between 190° and 200°. This suggestion can explain the low activity observed for **L1** with all the amine substrates used in our reactions, as **L1** has the lowest cone angle among the ligands used ($\theta = 182°$). Replacement of one *tert*-butyl group with a biphenyl group in **L3** increases the cone angle significantly ($\theta = 246°$)[17] which is clearly out of the suggested range. However, ligand **L3** gave high conversion of compound **2** to the desired product in all cases. Actually, this criterion stated by Hill *et al.* worked only with ligand **L2** ($\theta = 198°$)[17] in the coupling between compound **2** and piperidine. Obviously, a larger ligand size facilitates the formation of active PdL species from the coordinatively saturated PdL_2 by the ligand dissociation and thus promotes the oxidative addition to the quinoline substrate. Moreover, it could be observed during the amination of compound **2** with secondary amines, piperidine, pyrrolidine, and morpholine, that the different ligands employed, gave different conversion percentages from the starting materials to products and different arene/arylamine ratios. This can be attributed to the different steric requirements for each amine and to the ease of the β-hydrogen elimination from the intermediate complex. Pyrrolidine seems to be the most sensitive to the ligand size variation, in which case the amount of β-hydrogen elimination product decreases with the increasing ligand size.

After the optimization of the reaction conditions for each amine substrate, the reaction mixtures of the 5-amino-8-benzyloxyquinolines **3a–c** prepared under the optimal conditions were obtained in a pure form by column chromatography using the proper eluent. The purified compounds **3a–c** were deprotected by using the palladium catalyzed hydrogenation. The deprotection took 1–3 hours and gave the resulting deprotected 5-amino-8-hydroxyquinolines **4a–c** in high yields after work up.

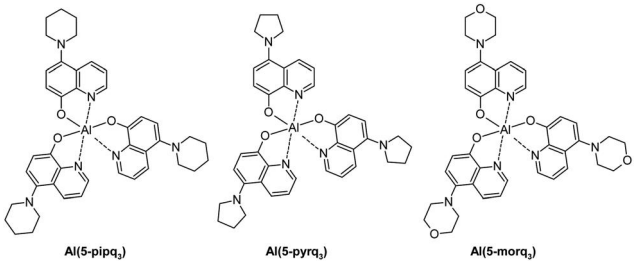

Fig. 2 The chemical structures of the 5-amino substituted Alq_3 derivatives.

The aluminum complexes Al(5-pipq)$_3$, Al(5-pyrq)$_3$ and Al(5-morq)$_3$ (Fig. 2) were prepared by complexing the ligands **4a–c** with aluminum isopropoxide in absolute ethanol for 24 hours under argon atmosphere.

2.2 Thermal analysis

Differential scanning calorimetry (DSC) measurements were carried out to investigate the solid state properties of the Alq_3 derivatives. Although, the parent Alq_3 has a clear melting peak at 417 °C, none of the derivatives exhibited any clear endothermic signal of melting. Around 400 °C all the derivatives showed broad exothermic peaks, which might be caused by the degradation of the complexes. Clear glass transition temperatures (T_g) could be observed at 208 °C, 213 °C, and 224 °C for Al(5-pyrq)$_3$, Al(5-pipq)$_3$, and Al(5-morq)$_3$ respectively, as shown in Fig. 3. T_g values of the derivatives are clearly higher than that of the parent Alq_3, which undergoes the glass transition at 162 °C (ref. 4*b*). In consequence of the higher T_g values compared to the parent Alq_3, the derivatives would have better stability in photovoltaic applications. The absence of melting peaks and the appearance of clear glass transitions indicate that the prepared Alq_3 derivatives are amorphous. Altogether, the derivatives seem to have very identical thermodynamic properties in a solid state according to the DSC measurements. Based on this result, the derivatives are assumed to have similar morphological properties in solid films as well.

2.3 Electrochemical analysis

The differential pulse voltammetry (DPV) measurements were carried out to determine the HOMO and LUMO levels of the Alq_3 derivatives. DPV curves in Fig. 4 exhibit reversible

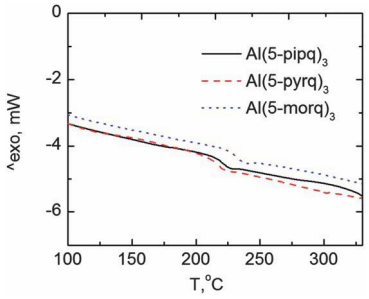

Fig. 3 Third DSC heating scan for Al(5-pipq)$_3$, Al(5-pyrq)$_3$ and Al(5-morq)$_3$.

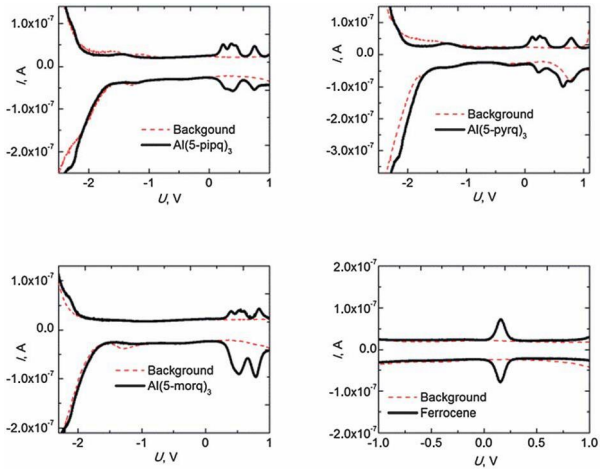

Fig. 4 DPV curves of Al(5-pipq)$_3$, Al(5-pyrq)$_3$, Al(5-morq)$_3$ and the ferrocene reference.

oxidation and reduction for all the derivatives. The ferrocene reference oxidation peak appears at 0.16 V. The HOMO and LUMO energy levels and the band gap energy for the derivatives were calculated based on the sample redox potentials referenced to the ferrocene oxidation potential. The results are presented in Table 4 and the HOMO and LUMO levels are illustrated in Fig. 5.

The absolute values of the electrochemical band gaps (E_g^{cc}) calculated based on the HOMO and LUMO levels differ slightly from the optical band gap (E_g^{opt}) values, which are calculated from the absorption maxima of the compounds in $CHCl_3$ solution (Fig. 6). However, the values have relative correspondence as Al(5-morq)$_3$ has the highest and Al(5-pyrq)$_3$ has the lowest calculated band gap in both methods.

The different electron donating properties of the 5-amino substituents on the 8-hydroxyquinoline ligand are supposed to ease the oxidation and raise the HOMO levels of the complexes with respect to the parent Alq_3. As can be seen in Fig. 5, the LUMO levels of the derivatives remained virtually unaffected, while the HOMO levels lie remarkably higher relative to the parent Alq_3.

2.4 Photophysical studies

Both steady state and time resolved spectroscopies were applied to investigate photophysical properties of the derivatives. Absorption spectra of the derivatives and the parent Alq_3 in $CHCl_3$ solution and in vacuum evaporated solid films are presented in Fig. 6 and 7. Steady state absorption and emission

Table 4 Electrochemical properties of the 5-amino substituted Alq_3 derivatives[a]

Derivative	HOMO [eV]	LUMO [eV]	E_g^{cc} [eV]	E_g^{opt} [eV]
Al(5-pipq)$_3$	−4.87	−2.33	2.54	2.89
Al(5-pyrq)$_3$	−4.77	−2.46	2.31	2.82
Al(5-morq)$_3$	−5.04	−2.48	2.56	2.96

[a] E_g^{opt} calculated from the absorption maxima in $CHCl_3$ solution at 430 nm for Al(5-pipq)$_3$, at 439 nm for Al(5-pyrq)$_3$ and at 419 nm for Al(5-morq)$_3$.

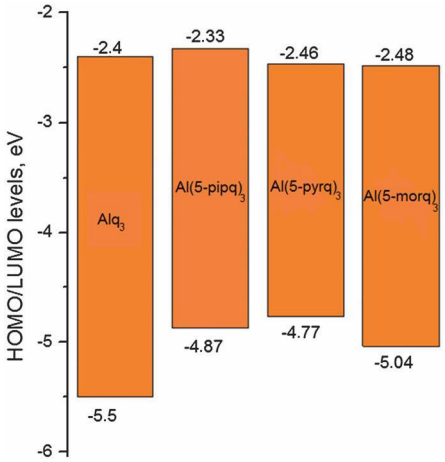

Fig. 5 HOMO and LUMO levels of Alq_3 (ref. 5), $Al(5\text{-pipq})_3$, $Al(5\text{-pyrq})_3$ and $Al(5\text{-morq})_3$.

properties are summarized in Table 5. The most significant difference between the emission properties of the derivatives and the parent Alq_3 is that the fluorescence emissions of the derivatives appear to be remarkably weak. The relative fluorescence emission quantum yields of $Al(5\text{-pipq})_3$ and $Al(5\text{-pyrq})_3$ are extremely low, 0.004 and 0.001 respectively, relative to Alq_3. However, $Al(5\text{-morq})_3$ has a slightly higher relative quantum yield, 0.017, with respect to the parent Alq_3.

All the derivatives have narrow emission bands, as shown in Fig. 8, between 375 and 425 nm, with excitation of the second absorption band at 320 nm. The excitation at the Soret band, 405 nm, provides the fluorescence emission in the range of 525–700 nm in the case of $Al(5\text{-morq})_3$ and 450–650 nm in the case of $Al(5\text{-pyrq})_3$ (Fig. 9). $Al(5\text{-pipq})_3$ has a broadened emission covering the wavelengths between 450 and 750 nm, the largest Stokes shift and the emission decay is multiexponential, as can be seen in the decay curves measured by time correlated single photon counting (TCSPC) in Fig. 10. Although $Al(5\text{-morq})_3$ has higher fluorescence quantum yield than the other derivatives, the emission decay occurs fastest and is the most clearly two-exponential.

The fluorescence emission lifetimes were calculated based on two-exponential global fittings of the TCSPC measurements and are presented in Table 6. Decay associated spectra (DAS) are presented in Fig. 11. The intensities of the spectra are the product

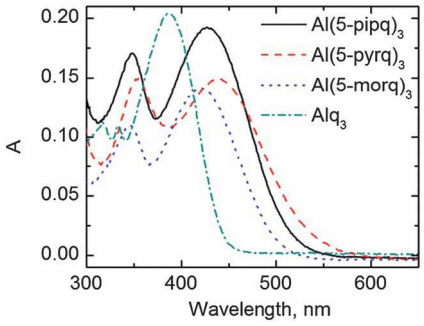

Fig. 6 Absorption spectra of the parent Alq_3 and the derivatives in $CHCl_3$ solution (60 μM).

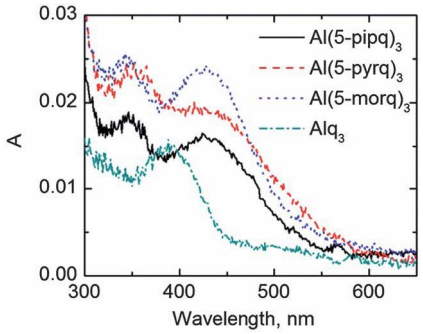

Fig. 7 Absorption spectra of the parent Alq_3 and the derivatives in solid films. The film thicknesses are 7.6 nm, 14.7 nm, 13.5 nm and 5.4 nm for $Al(5\text{-pipq})_3$, $Al(5\text{-pyrq})_3$, $Al(5\text{-morq})_3$ and Alq_3 respectively.

of the amplitude and lifetime at each wavelength, corrected according to the detector wavelength sensitivity. $Al(5\text{-pipq})_3$ and $Al(5\text{-pyrq})_3$ both have an intense long living, 3.54 ns and 4.83 ns respectively, decay component around 500 nm. However, the DAS of $Al(5\text{-morq})_3$ exhibits an intense short living, 0.50 ns (94%), component at 570 nm, whereas a longer living, 5.83 ns, component at 500 nm is faint (6%).

2.5 Alq_3 derivatives as buffer layers in inverted organic solar cells

The synthesized Alq_3 derivatives were tested as anode buffer layers in ITO|ZnO|P3HT:PCBM|Buffer|Au organic solar cells, the schematic structure of which is presented in Fig. 12. The parent Alq_3 was used as a reference buffer layer material. The solution-processed ZnO interlayer between ITO and the photoactive layer efficiently collects the electrons from the active layer to the ITO direction. This provides an inverted solar cell structure,[18] *i.e.* the electrons flow to the ITO cathode as shown in the energy level diagram in Fig. 13a.

The solar cells are illuminated through the glass substrate. The illuminated light passes through the transparent glass, ITO and ZnO layers and most of the light is absorbed by the *ca.* 100 nm thick photoactive P3HT:PCBM layer. The absorption of the ~5 nm buffer layer behind the photoactive layer is faint. Thus the contribution of the photophysical properties of the buffer layer to the function of the solar cell will be discussed together with the results of the solar cell experiments.

Table 5 Steady state absorption and emission properties of the derivatives and the parent Alq_3

Complex	λ_{sol}[a] (nm)	λ_{film}[b] (nm)	α[c] (μm^{-1})	$\lambda_{PL,\ sol}$[d] (nm)	Stokes shift[e] (nm)	ϕ_{PL}[f]
$Al(5\text{-pipq})_3$	430	426	1.4	617	187	0.004
$Al(5\text{-pyrq})_3$	439	429	1.3	511	72	0.001
$Al(5\text{-morq})_3$	419	427	1.8	575	156	0.017
Alq_3	385	385	2.1 (ref. 5)	513	128	1

[a] Absorption maximum in $CHCl_3$ solution. [b] Absorption maximum in a solid film. [c] Absorption coefficient in a solid film at 430 nm for the derivatives and at 398 nm for Alq_3. [d] Fluorescence emission maximum in $CHCl_3$ solution. [e] $\lambda_{PL,\ sol} - \lambda_{sol}$. [f] Relative fluorescence quantum yield with respect to the parent Alq_3 (the absolute fluorescence quantum yield for Alq_3 in $CHCl_3$ is 0.171 (ref. 6*b*)).

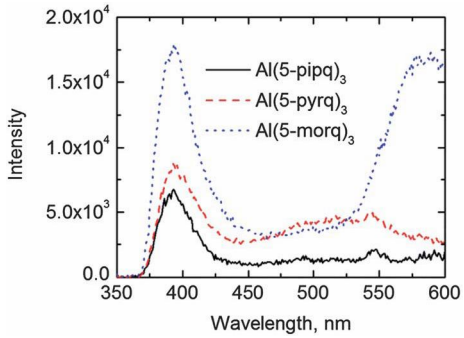

Fig. 8 Fluorescence emission spectra of the derivatives (λ_{ex} = 320 nm).

The photovoltaic parameters of the solar cell devices with the derivatives as buffer layers measured one day after preparation are presented in Table 7. The efficiency of the solar cell varies with the different buffer materials. The solar cell with Al(5-morq)$_3$ as a buffer layer gives the highest power conversion efficiency (η), 2.63%, which is higher than that (2.36%) of the reference device with Alq$_3$ as a buffer layer. Morphological properties in the solid buffer layers are assumed to be similar for the derivatives, because the DSC measurements showed uniform thermodynamic behavior. Morphological factors, whether crystalline or amorphous, of the buffer material seem not to cause the differences in the performance of the buffer layers because both crystalline Alq$_3$ and amorphous derivatives seem to work well as buffer layers.

Absorption spectra and *I*–*V* curves of the solar cell devices measured one day after preparation are shown in Fig. 14 and 15. The absorption spectra of the solar cells with different buffer layers do not differ between 350 nm and 450 nm, where the absorption of the buffer materials takes place. Some differences in the absorption spectra can be seen around 500 nm, where the P3HT absorption peaks, showing small variation in the photoactive layer thicknesses of the solar cell samples. The cell absorptions are between 0.7 and 0.8, while the maximum absorption of ~5 nm buffer layer according to Fig. 7 in the case of Alq$_3$ is only about 0.015, which is negligible compared to the cell absorption. Also the absorption coefficients of the derivatives and parent Alq$_3$ are small. Previous studies[5] about Alq$_3$ derivatives as buffer layers proposed that due to minor absorption of the buffer compared to the cell absorption, the buffer layer acts as a transparent spacer and charge transporting layer between the photoactive region and the metal anode.

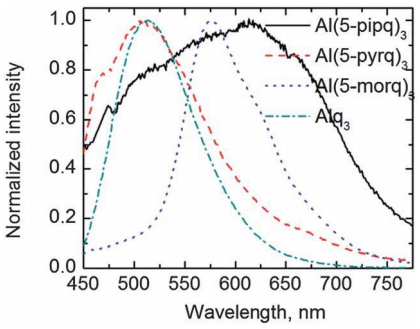

Fig. 9 Normalized fluorescence emission spectra of the derivatives and the parent Alq$_3$, λ_{ex} = 405 nm.

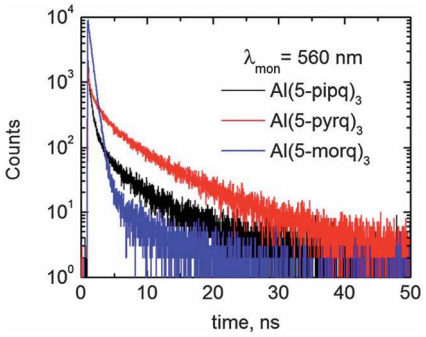

Fig. 10 Fluorescence emission decay (λ_{ex} = 405 nm) curves of the derivatives at a monitoring wavelength of 560 nm.

Table 6 Fluorescence emission lifetimes of the two-exponential fit for the derivatives (one-exponential for Alq$_3$) and the average lifetimes

Complex	τ_1 (ns)	τ_2 (ns)	τ_{avg} (ns)
Al(5-pipq)$_3$	3.54 (56%)	0.15 (44%)	2.05
Al(5-pyrq)	4.83 (87%)	0.51 (13%)	4.27
Al(5-morq)$_3$	0.50 (94%)	5.83 (6%)	0.82
Alq$_3$	16.62 (ref. 5)	—	16.6

To further validate the assumption, that the photophysical properties of the weakly absorbing buffer layer do not affect the cell efficiency, the fluorescence properties of different buffer layer materials can be compared together with the cell efficiencies. The fluorescence lifetimes and quantum yields of all the 5-substituted derivatives are remarkably smaller than those of the parent Alq$_3$. This means that the average existence of the excited state of Alq$_3$ is much longer compared to that of the derivatives. However, the cell efficiency seems not to depend on either quantum yield or lifetime. The cell with Al(5-morq)$_3$, which has both very low ϕ_{PL} and the shortest τ_{avg} (Table 6) of all the derivatives, has better η than the cell with highly fluorescent Alq$_3$ as a buffer layer measured one day after the device preparation. According to this result, the contribution of the buffer layer to the cell efficiency seems not to be influenced by the excited state of the buffer layer material. Thus the ground state properties, such as conductivity

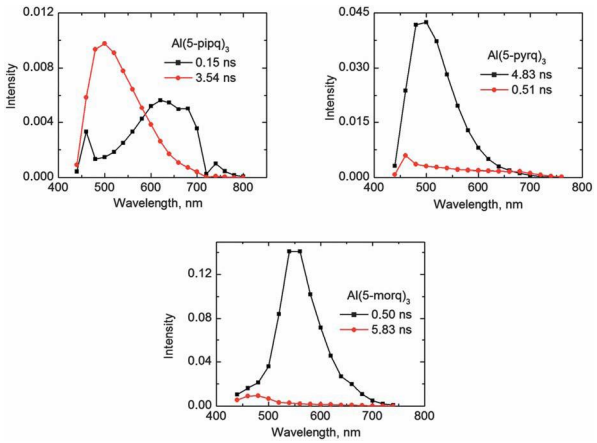

Fig. 11 Decay associated spectra of Al(5-pipq)$_3$, Al(5-pyrq)$_3$ and Al(5-morq)$_3$.

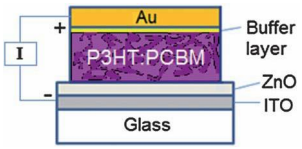

Fig. 12 Schematic structure of the inverted organic solar cell.

or contact with both the metal anode and the photoactive layer, seem to define the function of the buffer layer in the inverted organic solar cells.

Conductivity of both types of carriers inside the buffer layer is necessary, as the holes ejected from the photoactive layer recombine with the electrons produced by the photoexcitation and inserted into the cell from an external circuit *via* the gold anode. The electron to hole mobility ratio (μ_e/μ_h) primarily controls the charge recombination and the mobility of holes in the parent Alq_3 is generally two orders of magnitude less than that of electrons.[20] Therefore major attention will be drawn to the transport of slower charge carriers, holes, at the P3HT/buffer interface. The transport of holes, from P3HT to the gold anode modified by the buffer layer, is controlled by the HOMO energy

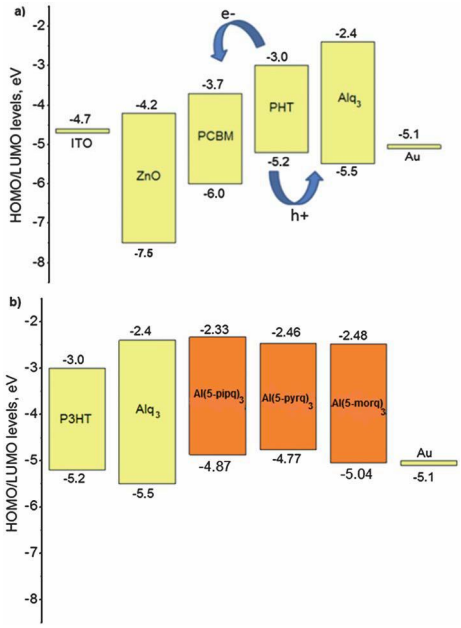

Fig. 13 (a) Energy levels of the inverted organic solar cell device. Measured values for the derivatives and the literature values for ITO,[3] ZnO,[19] PHT,[19] PCBM,[19] Alq_3,[5] and Au;[19] (b) energy levels of the derivatives and the parent Alq_3 positioned between the gold electrode and P3HT in the cell structure.

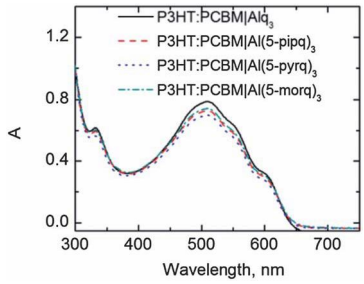

Fig. 14 Absorption spectra of the solar cells with Alq_3 and the derivatives as buffer layers.

levels of P3HT and the used buffer material. Thus the results of solar cell experiments are justified in terms of the energy levels in the following.

The difference between HOMO of P3HT and that of the buffer layer affects the cell V_{OC}. An injection barrier for holes is formed if the HOMO of the buffer layer lies higher than that of P3HT. The current through the P3HT:PCBM blend is driven by the electrons, which recombine with holes at the buffer/blend interface. The extraction force for the photogenerated charge carriers decreases due to the diminished built-in field caused by the injection barrier and V_{OC} is decreased.[8] The device with Alq_3 as an anode buffer layer produced the highest V_{OC}, 0.51 V. The HOMO level of Alq_3 at −5.5 eV lies lower than the HOMO of P3HT and no injection barrier exists (Fig. 13b). HOMO levels of all the 5-amino substituted derivatives lie higher than that of P3HT and therefore injection barriers are created. However, the HOMO level of Al(5-morq)$_3$, at −5.04 eV, lies lower than the HOMO levels of Al(5-pipq)$_3$, at −4.87 eV, and Al(5-pyrq)$_3$, at −4.77 eV. Thus the device with Al(5-morq)$_3$ as an anode buffer layer produced low injection barrier, 0.16 eV, and nice V_{OC}, 0.48 V. The devices with Al(5-pipq)$_3$ and Al(5-pyrq)$_3$, which have higher injection barriers than Al(5-morq)$_3$, 0.33 eV and 0.43 eV respectively, produced smaller V_{OC}, 0.45 V.

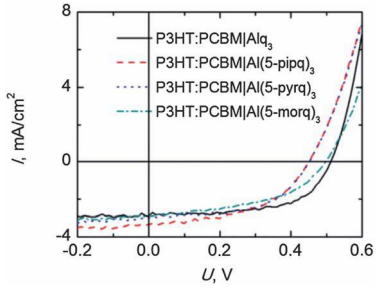

Fig. 15 *I–V* curves of the solar cells with Alq_3 and the derivatives as buffer layers measured 1 day after preparation.

Table 7 Photovoltaic parameters of the solar cells with Alq_3 and the derivatives as buffer layers measured one day after the cell preparation

Used buffer layer (thickness, nm)	I_{SC} (mA cm^{-2})	V_{OC} (V)	FF (%)	η (%)	R_s (Ω cm^{-2})	R_{sh} (Ω cm^{-2})
Alq_3 (4.30)	−2.91	0.51	60	2.36	17.94	1797
Al(5-pipq)$_3$ (4.00)	−3.33	0.45	50	2.02	19.65	600
Al(5-pyrq)$_3$ (3.60)	−3.01	0.45	55	1.99	20.04	820
Al(5-morq)$_3$ (3.66)	−3.20	0.48	64	2.63	25.72	564

Table 8 Photovoltaic parameters of the solar cells with Alq_3 and the derivatives as buffer layers measured 5 months after the cell preparation

Used buffer layer	I_{SC} (mA cm^{-2})	V_{OC} (V)	FF (%)	η (%)	R_s (Ω cm^{-2})	R_{sh} (Ω cm^{-2})
Alq_3	−2.89	0.55	62	2.62	28.03	2824
Al(5-pipq)$_3$	−3.52	0.53	56	2.76	30.67	1031
Al(5-pyrq)$_3$	−3.46	0.52	54	2.59	24.72	752
Al(5-morq)$_3$	−3.56	0.53	56	2.80	28.70	1161

The highest FF, 64%, was also produced by the device with Al(5-morq)$_3$ as a buffer layer. The high FF is due to the small energy difference, 0.16 eV, between the HOMO levels of P3HT and Al(5-morq)$_3$. FF decreases as soon as the HOMO mismatch is more than 0.2 eV.[8] The parent Alq_3 has an extraction barrier, 0.3 eV, and therefore FF is slightly lower, 60%. The difference between HOMO levels of Al(5-pipq)$_3$ and Al(5-pyrq)$_3$ compared to the HOMO of P3HT is 0.33 eV and 0.43 eV respectively. The cells with Al(5-pipq)$_3$ and Al(5-pyrq)$_3$ had FF values of 50% and 55% respectively, which are clearly lower than that of the cell with Al(5-morq)$_3$ as a buffer layer.

Long-term stability measurements of the solar cells were carried out 5 months after the device preparation and storage in ambient air in darkness. The photovoltaic parameters measured 5 months after the device preparation are given in Table 8 and the corresponding I–V curves of the solar cells are shown in Fig. 16. The devices with Alq_3 and 5-amino substituted derivatives as buffer layers had better performance (Table 7) after the 5-month storage than one day after the preparation. The highest percentage increase, 36.6%, in η was achieved by the device with the Al(5-pipq)$_3$ buffer layer. Despite a rather small, 6.5%, increase in η, the device with the Al(5-morq)$_3$ buffer layer had the highest η, 2.80%, also after the 5-month storage.

Especially, V_{OC} of the cells had increased significantly during the storage. The values followed the same order as measured one day before preparation. The cell with Alq_3 had the highest and the cell with Al(5-pyrq)$_3$ had the lowest V_{OC}. However, the distinction of the V_{OC} values between the cells with different buffer layers was not as substantial as before.

The FF values of the cells had also changed during the storage. FF of the cell with Al(5-pipq) as the buffer layer had increased from 50% to 56%. FF values of the cells with Alq_3 and Al(5-pyrq)$_3$ had not changed significantly. The most drastic change, from 64% to 56%, took place in the cell with Al(5-morq)$_3$ as the buffer layer. Due to the changes during the storage the FF values

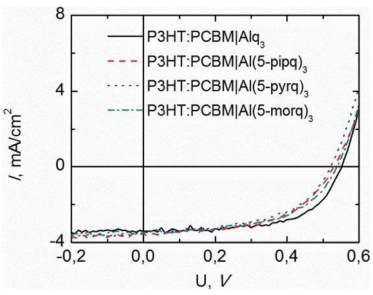

Fig. 16 I–V curves of the solar cells with Alq_3 and the derivatives as buffer layers measured 5 months after preparation.

are not consistent with the measurements carried out one day after preparation. To explain the differences in FF values and further compare the results of measurements carried out one day and five months after preparation, the serial resistances and shunt resistances (R_s and R_{sh}, Tables 7 and 8) of the solar cells were calculated based on the I–V curves as explained in the literature.[21]

During the storage both R_s and R_{sh} values of the reference cell with the Alq_3 buffer layer increased by a factor of 1.56. The R_s of the cell with Al(5-pipq)$_3$ also increased by a factor of 1.56, in which case the effective current change caused by the ageing of the cell is of the same order as in the case of Alq_3. However R_{sh} of the cell with Al(5-pipq)$_3$ increased by a factor of 1.72. R_{sh} is correlated with the amount of recombinations and leakage current[21] in the cell. The cell with Al(5-pipq)$_3$ has relatively higher R_{sh} after the storage than the cell with Alq_3, which means lower recombination rate in the cell with Al(5-pipq)$_3$. This together with the remarkably increased V_{OC} improved the FF and the cell with Al(5-pipq)$_3$ experienced the largest increase in η and the absolute value, 2.76%, is even bigger than that, 2.62%, of the reference device with Alq_3.

R_s of the cell with Al(5-pyrq)$_3$ increased by a factor of 1.23 during the storage and therefore the cell has the biggest increase in I_{SC}. Although R_{sh} had decreased during the storage the increased V_{OC} and I_{SC} resulted in improved η. However the absolute η, 2.59%, is slightly smaller than that of the reference device.

The device with the Al(5-morq)$_3$ buffer layer had the smallest relative and absolute increase in R_s, which means that the current in the cell is nearly the same before and after the storage. In addition the current losses are diminished efficiently as R_{sh} was improved by the highest factor, 2.06. These together resulted in the best η, 2.80%.

In conclusion, the energy levels of Al(5-morq)$_3$ seem to lie in advantageous positions in terms of charge transfer in the inverted solar cell structure. The HOMO level of Al(5-morq)$_3$, positioned close to both HOMO of P3HT and work function of Au, guarantees efficient hole transportation to the anode. Moreover, the LUMO level of Al(5-morq)$_3$ is high enough to prevent any electron flow to the anode direction. These together result in a I_{SC} of 3.20 mA cm^{-2}, V_{OC} of 0.48 V and a high FF of 64%, and therefore the device with Al(5-morq)$_3$ gives the highest η one day after the preparation. The device with Al(5-morq)$_3$ performed best also after 5-month storage due to smallest increase in R_s and highest relative increase in R_{sh}.

3. Experimental section

3.1 Materials used in the electrochemical measurements and preparation of the solar cell devices

The solvents, $TBAPF_6$ supporting electrolyte and parent Alq_3 (99.995%) were purchased from Sigma-Aldrich and used without further purification. The solar cell samples were prepared on indium tin oxide (ITO) coated glass substrates (1.2 cm × 3.5 cm) purchased from Solems. The zinc-acetate ($Zn(O\text{-}COCH_3)_2 \cdot 2H_2O$) for ZnO layer preparation was from Sigma-Aldrich and the active layer compounds P3HT and PCBM from Rieke Metals Inc. (4002-E) and Nano-C, respectively.

3.2 DSC measurements

A Mettler Toledo DSC821 thermo analyzer was used for differential scanning calorimetry measurements. To observe the thermodynamic properties of the Alq_3 derivatives, 1 mg of each complex was heated from 25 °C to 500 °C by dynamic 20 °C min^{-1} heating rate in a standard 40 μg Al cup with 60 mL min^{-1} N_2 flow. For determination of T_g, 5 mg of each derivative was heated from −70 °C to 350 °C with 20 K min^{-1} heating rate and cooled back to −70 °C with 60 mL min^{-1} N_2 flow. The same procedure was repeated three times for each sample to first remove the thermal history and then observe the ongoing thermodynamic processes. T_gs are reported as on-set values.

3.3 DPV measurements and determination of HOMO and LUMO levels

DPV measurements were carried out by employing an Iviumstat (Compactstat IEC 61326 Standard) potentiostat and a three-electrode cell configuration to determine HOMO and LUMO energy levels for the derivatives. Measurements were carried out using 0.1 M $TBAPF_6$ in dichloromethane (DCM) as the supporting electrolyte, glass platinum electrode as the working electrode, graphite rod as the counter electrode and platinum wire as the pseudo reference electrode. For each sample, the background was measured for 2.5 mL of the electrolyte solution after 20 min deoxygenation by purging with N_2. 100 μL of 0.5 mM sample in DCM was inserted and the system was stabilized again purging with N_2. Each sample was measured between −2.5 V and 1.5 V scanning in both directions with 2.5 mV steps. Ferrocene (Acros Organics, 98%) was used as the internal standard reference to scale the measured potentials against the vacuum level.[22] HOMO and LUMO level calculations were based on the formal oxidation and reduction potentials observed in the DPV curves according to the following equations:

$$E_{HOMO} = -(4.8 + E_{dif,ox})\ eV$$

$$E_{LUMO} = (-E_{dif,red} + 4.8)\ eV$$

where 4.8 eV is the oxidation energy of ferrocene. $E_{dif,ox}$ is the difference in volts between the formal oxidation potentials of ferrocene and the measured sample. $E_{dif,red}$ is the difference in volts between the formal oxidation potential of ferrocene and the formal reduction potential of the sample.

3.4 Solid film thickness measurements with the profilometer and determination of α value

To determine the film thickness of the derivatives in a solid state, carefully cleaned quartz plates with a narrow strip of tape crossing in the middle of the plate were placed inside an Edwards Auto 306 evaporator. Test films of 5, 10 and 15 nm of each derivative were vacuum ($\sim 10^{-6}$ mbar) evaporated on the quartz plates. Prior to the measurements with a WYKO NT-1100 profilometer the tape was removed, leaving the bare glass stripe in the middle of the evaporated film, and producing a sharp step of the solid film on the edges of the bare glass stripe. The step was analyzed by the profilometer using phase shift interferometry $230 \times 300\ \mu m^2$. The vertical resolution of this method is close to 1 Å according to the instrument manual and the horizontal resolution of the objective (20× magnification) is 0.75 μm. The determination of film thicknesses and absorption coefficients (α) was done according to a literature process[23] and is presented in the ESI.†

3.5 Spectroscopic measurements

The steady state absorption and fluorescence measurements were done employing a UV-3600 Shimadzu UV-VIS-NIR spectrophotometer and a Jobin Yvon-SPEX fluorolog. The fluorescence lifetimes were determined with a time correlated single photon counting (TCSPC) system equipped with a Picoharp 300 controller and a PDL 800-B driver for excitation and a microchannel plate photomultiplier (Hamamatsu R3809U-50) for detection in 90

405 nm and the pulse frequency was 2.5 MHz. The experimental set-up of the measuring instrumentation was similar for all the derivatives.

3.6 Preparation of the solar cell devices

Solar cells were constructed on commercial ITO covered glass substrates. The ITO layer was taped and polished for *aqua regia* etching to achieve a patterned ITO. After 30 min sonication in acetone, $CHCl_3$, SDS (sodium dodecyl sulfate) solution, H_2O and 2-propanol and a 10 min N_2 plasma cleaning procedure (Harrick Plasma Cleaner PDG-236), the 20 nm ZnO layer was deposited by 1 min spin-coating in a WS-400B-6NPP/LITE spin-coater from Laurell Technologies from 50 g L^{-1} zinc-acetate in 96% 2-methoxyethanol and 4% ethanolamine solution following the literature process.[18]

The photoactive layer compounds P3HT and PCBM were dissolved separately in 1,2-dichlorobenzene and stirred (250 rpm) for 4 hours at 50 °C. Thereafter the solutions were combined and stirred (500 rpm) at 70 °C for one hour and at 50 °C (250 rpm) overnight. The temperature was raised to 70 °C for 30 min prior to spin-coating the ~100 nm thick photoactive layer from the 32 g L^{-1} P3HT:PCBM (mass ratio 1 : 0.8) blend for 5 minutes (600 rpm) under N_2 flow. The spin-coated films were annealed in vacuum at 110 °C for 10 min. The buffer layer and Au anode were evaporated in the vacuum evaporator under $\sim 3 \times 10^{-6}$ mbar pressure. The evaporation rate and film thickness were controlled by evaporator crystals to deposit a ~5 nm thick buffer layer and 50 nm thick gold anode layer on top of the buffer. The devices were stored in ambient air for 24 hours in the dark before measurements and analysis.

The photovoltaic parameters were obtained and calculated from current–voltage (I–V) curves, which were measured under simulated AM 1.5 sunlight illumination (50 mW cm^{-2}) using an Agilent E5272A source/monitor unit. A voltage between −0.2 and 0.6 V was applied in 10 mV steps and the measurements were carried out in air at room temperature without encapsulation of the devices. The illumination was produced by a filtered Xe-lamp (Oriel Corporation & Lasertek) in the Zuzchem LZC-SSL solar simulator. The illumination power density was measured using a Coherent Fieldmax II LM10 power meter. Because a certified

measuring system could not be employed, the absolute efficiency values are not directly comparable with the other published results. However, the reported efficiencies and the relative efficiency changes are comparable within the presented devices.

3.7 General considerations about syntheses

All reactions were carried out under argon atmosphere except the palladium catalyzed deprotection of the benzyloxy group in 8-(benzyloxy)-5-bromoquinoline **2** which was carried out under hydrogen atmosphere. Solvents were dried by molecular sieves of the proper size. 5-Bromo-8-hydroxyquinoline was purchased from Tokyo Chemical Industry Co. (TCI). 8-(Benzyloxy)-5-bromoquinoline was synthesized according to previously published procedures.[11] Ligands (**L_1–L_3**) were purchased from Aldrich Chemical company. Palladium acetate was purchased from Fluka Chemical Company. Melting points were determined using a METTLER TOLEDO DSC821 at a heating rate of 10 °C min^{-1}. NMR analyses (^1H and ^{13}C) were performed using Bruker DPX 200 (200 MHz) and Varian Mercury 300 MHz (Varian Inc.) spectrometers. TLC was performed on dry silica gel plates using a chloroform–methanol mixture as the eluent.

3.8 General procedure for the synthesis of 8-(benzyloxy)-5-aminoquinoline derivatives 3(a–c) *via* Hartwig–Buchwald amination reaction

In an oven dried vessel with a magnetic stirring bar, toluene was added and bubbled with argon for 10 min. Compound **2**, $Pd(OAc)_2$ (5 mol%), ligand of choice after optimization (10 mol %), sodium *tert*-butoxide (1.25 equiv.) and amine (1.25 equiv.) were added and the reaction mixture stirred under argon at appropriate temperature. The reaction mixture was then allowed to cool to room temperature, filtered through a thin pad of silica gel and the solvent was evaporated under vacuum. The product was purified by flash chromatography using acetone–*n*-hexane (1 : 1) as the eluent.

8-(Benzyloxy)-5-(piperidin-1-yl)quinoline (3a). The title compound was prepared by following the general procedure. The specific amounts of chemicals used: compound **2** (250 mg, 0.796 mmol), $Pd(OAc)_2$ (9.0 mg, 0.040 mmol), ligand **L2** (24.3 mg, 0.080 mmol), sodium *tert*-butoxide (96.8 mg, 1.01 mmol) and piperidine (0.10 mL, 1.01 mmol). The reaction was stirred for 24 h at 100 °C. The procedure gave the title compound **3a** as an off-white powder (213 mg, 84%). Mp 113–114 °C. ^1H NMR (300 MHz; DMSO-d_6; Me_4Si) 1.59 (2H, br s), 1.75 (4H, q, $J = 5.4$), 2.89 (4H, br s), 5.26 (2H, s), 7.09 (1H, d, $J = 8.1$), 7.18 (1H, d, $J = 8.4$), 7.32–7.45 (3H, m), 7.52–7.58 (3H, m), 8.46 (1H, dd, $J = 8.6$, 1.7), 8.85 (1H, dd, $J = 4.0$, 1.6). ^{13}C NMR (75 MHz; DMSO-d_6; Me_4Si) 24.0 (CH_2), 26.2 (2C, CH_2), 54.4 (2C, CH_2), 70.1 (CH_2), 110.0, 115.1, 121.1, 124.6, 127.8 (3C), 128.4 (2C), 131.7, 137.3, 140.7, 143.6, 148.8, 150.2. HRMS: calcd for $C_{21}H_{23}N_2O$ ([M + H]$^+$) 319.1810, found 319.1822.

8-(Benzyloxy)-5-(pyrrolidin-1-yl)quinoline (3b). The title compound was prepared by following the general procedure. The specific amounts of chemicals used: compound **2** (500 mg, 1.59 mmol), $Pd(OAc)_2$ (5 mol%, 17.86 mg, 0.080 mmol), ligand **L3** (49.05 mg, 0.16 mmol), sodium *tert*-butoxide (191.17 mg, 2 mmol) and pyrrolidine (0.16 mL, 2 mmol). The reaction temperature was adjusted to 80 °C and the reaction completed in 30 minutes. The procedure gave the title compound **3b** as yellow crystals (0.38 g, 80%). Mp 102–103 °C. ^1H NMR (200 MHz; DMSO-d_6; Me_4Si) 1.90 (4H, br s), 3.14 (4H, br s), 5.23 (2H, s, CH_2), 6.93 (1H, d, $J = 8.3$), 7.10 (1H, d, $J = 8.7$), 7.32–7.54 (6H, m), 8.47 (1H, d, $J = 8.7$), 8.83 (1H, d, $J = 2.6$). ^{13}C NMR (50 MHz; DMSO-d_6; Me_4Si) 24.9 (2C), 53.4 (2C), 71.1 (CH_2), 111.5, 112.9, 121.2, 124.8, 128.6 (3C), 129.2 (2C), 133.5, 138.4, 141.5, 141.6, 149.5, 150.0. HRMS: calcd for $C_{20}H_{21}N_2O$ ([M + H]$^+$) 305.1654, found 305.1659.

8-(Benzyloxy)-5-morpholin-1-yl)quinoline (3c). The title compound was prepared by following the general procedure. The specific amounts of chemicals used: compound **2** (500 mg, 1.59 mmol), $Pd(OAc)_2$ (5 mol%, 17.86 mg, 0.080 mmol), ligand **L3** (49.05 mg, 0.16 mmol), sodium *tert*-butoxide (191.17 mg, 2 mmol) and morpholine (0.17 mL, 2 mmol). The reaction temperature was adjusted to 100 °C and the reaction time was 3 hours. The procedure gave the title compound **3c** as yellowish crystals (0.43 g, 84%). Mp 119–120 °C. ^1H NMR (200 MHz; DMSO-d_6; Me_4Si) 2.53 (4H, t, $J = 4.2$), 3.83 (4H, t, $J = 3.9$), 5.29 (2H, s, CH_2), 7.17–7.24 (2H, m), 7.36–7.61 (6H, m), 8.53 (1H, dd, $J = 8.8$, 1.7), 8.88 (1H, dd, $J = 4.1$, 1.5). ^{13}C NMR (50 MHz; DMSO-d_6; Me_4Si) 53.9 (2C), 67.0 (2C), 70.5, 110.1, 115.9, 121.7, 124.8, 128.2 (3C), 128.9 (2C), 132.1, 137.7, 141.2, 142.6, 149.4, 151.1. HRMS: calcd for $C_{20}H_{21}N_2O_2$ ([M + H]$^+$) 321.1603, found 321.1571.

3.9 General procedure for the synthesis of 5-amino-8-hydroxyquinolines 4(a–c)

In a dry two-necked round bottom flask, 150 mg of 5-amino-8-benzyloxyquinoline (**3a–c**) and 30 mg Pd–C (10 wt%) were stirred and refluxed in ethanol under hydrogen atmosphere for 3 hours. The reaction mixture was then filtered through a thin pad of silica gel. The solvent was evaporated under vacuum and the residue was recrystallized from the appropriate solvent.

5-Piperidinyl-8-hydroxyquinoline (4a). Compound **4a** was prepared according to the general procedure, dissolved in ethanol, filtered through a 0.20 μm syringe filter and the filtrate was evaporated to dryness. The precipitate was boiled in water, cooled to rt, filtered and washed with water. These procedures gave the product as a greenish powder (102 mg, 94%). Mp 115–116 °C. ^1H NMR (300 MHz; DMSO-d_6; Me_4Si) 1.58 (2H, br s), 1.74 (4H, q, $J = 5.4$), 2.88 (4H, br s), 6.98 (1H, d, $J = 8.1$), 7.07 (1H, d, $J = 8.1$), 7.56 (1H, dd, $J = 8.6$, 4.2), 8.46 (1H, dd, $J = 8.6$, 1.4), 8.83 (1H, dd, $J = 4.0$, 1.2), 9.38 (1H, br s). ^{13}C NMR (75 MHz; DMSO-d_6; Me_4Si) 24.0 (CH_2), 26.2 (2C, CH_2), 54.5 (2C, CH_2), 110.4, 116.2, 121.1, 124.2, 132.0, 139.1, 141.9, 147.9, 149.1. HRMS: calcd for $C_{14}H_{17}N_2O$ ([M + H]$^+$) 229.1341, found 229.1348.

5-Pyrrolidinyl-8-hydroxyquinoline (4b). Compound **4b** was prepared according to the general procedure and recrystallized from methanol to give yellow crystals (72 mg, 68%). Mp 83–84 °C. ^1H NMR (200 MHz; DMSO-d_6; Me_4Si) 1.92 (4H, br s),

3.13 (4H, br s), 6.97 (2H, s), 7.47–7.54 (1H, m), 8.49 (1H, d, J = 8.6), 8.81 (1H, d, J = 3.1), 9.21 (1H, OH). ^{13}C NMR (50 MHz; DMSO-d_6; Me_4Si) 24.5 (2C), 53.1 (2C), 111.0, 114, 120.9, 124.2, 133.5, 139.2, 139.4, 148.2, 148.5. HRMS: calcd for $C_{13}H_{15}N_2O$ ($[M + H]^+$) 215.1184, found 215.1180.

5-Morpholinyl-8-hydroxyquinoline (4c). Compound **4c** was prepared according to the general procedure and recrystallized from ethanol to give yellow crystals (85 mg, 79%). Mp 160–161 °C. ^{1}H NMR (200 MHz; DMSO-d_6; Me_4Si) 2.94 (4H, t, J = 4.4), 3.85 (4H, t, J = 4.2), 7.01 (1H, d, J = 8.6), 7.13 (1H, d, J = 8.4) 7.55–7.62 (1H, m), 8.54 (1H, dd, J = 8.5, 1.1), 8.87 (1H, dd, J = 4.0, 1.2), 9.50 (1H, OH). ^{13}C NMR (50 MHz; DMSO-d_6; Me_4Si) 54.0 (2C), 67.1 (2C), 110.9, 117.0, 121.7, 124.6, 132.5, 139.6, 140.9, 148.5, 150.1. HRMS: calcd for $C_{13}H_{15}N_2O_2$($[M + H]^+$) 231.1134, found 231.1131.

3.10 General procedures for the synthesis of tris(5-amino-8-hydroxyquinoline)aluminum derivatives

Compound **4** (3 equiv.) and aluminium isopropoxide (1 equiv.) were refluxed in ethanol for 21 hours under argon atmosphere. The Alq_3 derivatives were obtained after reaction work up.

Tris-(5-piperidinyl-8-hydroxyquinoline)aluminum (Al(5-pipq)$_3$). Compound **4a** (100 mg, 0.44 mmol) and aluminium isopropoxide (29.8 mg, 0.15 mmol) were refluxed in ethanol (10 mL) for 21 h under argon atmosphere. The reaction mixture was filtered and the filtrate was evaporated to dryness. The precipitate was dissolved in acetone (1.5 mL) and the resulting solution was added dropwise in *n*-hexane (12 mL). The precipitated product was filtered and washed with solvent mixture. The procedure gave the product as a greenish yellow powder (47.1 mg, 46%). ^{1}H NMR (300 MHz; DMSO-d_6; Me_4Si) 1.56 (6H, br s), 1.72 (12H, br s), 2.87 (12H, br s), 6.63 (1H, d, J = 8.1), 6.78 (2H, dd, J = 8.1, 2.2), 7.13–7.19 (3H, m), 7.28 (1H, d, J = 4.0), 7.45 (1H, dd, J = 8.1, 5.0), 7.60 (1H, dd, J = 7.9, 4.8), 7.69 (1H, dd, J = 8.6, 4.8), 8.56–8.64 (4H, m), 8.76 (1H, d, J = 5.0). HRMS: calcd for $C_{42}H_{45}N_6O_3Al$ (M^+) 708.3369, found 708.3373.

Tris-(5-pyrrolidinyl-8-hydroxyquinoline)aluminum (Al(5-pyrq)$_3$). Compound **4b** (180 mg, 0.84 mmol) and aluminium isopropoxide (57.2 mg, 0.28 mmol) were refluxed in ethanol (10 mL) for 21 h. The reaction mixture was then concentrated under vacuum and light petrol was added. The precipitate formed was filtered and washed with petroleum ether (10 mL, three portions, boiling range 80–110 °C). The procedure gave the product as a reddish brown powder (175.5 mg, 94%). ^{1}H NMR (200 MHz; DMSO-d_6; Me_4Si) 1.93 (12H, br s), 3.04 (12H, br s), 6.62 (1H, d, J = 8.5), 6.78 (2H, d, J = 8.5), 7.07–7.17 (3H, m), 7.30–7.67 (4H, m), 8.62–8.80 (5H, m). HRMS: calcd for $C_{39}H_{40}N_6O_3Al$ ($[M + H]^+$) 667.2977, found 667.3007.

Tris-(5-morpholinyl-8-hydroxyquinoline)aluminum (Al(5-morq)$_3$). Compound **4c** (82 mg, 0.36 mmol) and aluminium isopropoxide (24 mg, 0.12 mmol) were refluxed in ethanol 8 mL for 24 h. The reaction mixture was then concentrated and treated with petroleum ether. The precipitate formed was filtered and washed with petroleum ether. The procedure gave the product as an orange powder (64.0 mg, 75%). ^{1}H NMR (200 MHz; DMSO-d_6; Me_4Si) 2.81 (12H, br s), 3.82 (12H, br s), 6.79 (1H, d, J = 8.3), 6.80 (2H, d, J = 8.1), 7.20–7.76 (3H, m), 8.64–8.81 (5H, m). HRMS: calcd for $C_{39}H_{40}N_6O_6Al$ ($[M + H]^+$) 715.2825, found 715.2827.

4. Conclusions

The Hartwig–Buchwald coupling could be applied efficiently in the preparation of 5-amino-8-hydroxyquinolines from 8-(benzyloxy)-5-bromoquinoline. Three phosphine ligands (**L1–L3**) were employed during the amination reaction optimization, and only the ligands with a cone angle higher than 182° were proved to achieve the amination successfully. The relative reactivity of **L2** and **L3** depends on the amine steric requirements. The primary side product formed during the amination reaction was the reduction product, 8-benzyloxyquinoline. The amount of the reduction product could be controlled by optimization of the reaction conditions and appropriate choice of the ligand. The benzyloxy group at the 8-position of 8-(benzyloxy)-5-bromoquinoline tolerated the amination reaction conditions and could be removed after the amination reaction by catalytic hydrogenation affording the 5-amino-8-hydroxyquinolines in high purity.

The three 5-amino substituted Alq_3 derivatives were characterized and applied as anode buffer layer materials in inverted organic solar cells. All the derivatives exhibited similar amorphous properties in DSC measurements. Due to higher glass transition temperatures compared to the parent Alq_3, the derivatives possess better thermodynamic stability than Alq_3. According to the DPV measurements, the electron-donating 5-amino substituents of the Alq_3 derivatives affected notably HOMO levels of the complexes, which lie remarkably higher compared to those of the parent Alq_3. LUMO levels of the derivatives remained virtually unaffected. Although the steady state and time resolved spectroscopic measurements showed lower quantum yield and shorter lifetime for all the derivatives compared to Alq_3, Al(5-morq)$_3$ performed better than the parent Alq_3 or the other derivatives as anode buffer layer materials in organic solar cells. The cell with Al(5-morq)$_3$ as a buffer layer had a clearly improved fill factor and showed the highest power conversion efficiency due to suitable HOMO and LUMO levels of the buffer layer relative to the energy levels of the inverted organic solar cell structure.

Note added after first publication

This article replaces the version published on 13th September 2012, which contained errors in the last sentence of Section 2.5.

Acknowledgements

The authors thank Mrs Päivi Joensuu for HRMS data. The National Doctoral Program in nanoscience (NGS-NANO) is greatly acknowledged for funding.

References

1 C. W. Tang and S. A. VanSlyke, *Appl. Phys. Lett.*, 1987, **51**(12), 913–915.

2 Q. L. Song, F. Y. Li, H. Yang, H. R. Wu, X. Z. Wang, W. Zhou, J. M. Zhao, X. M. Ding, C. H. Huang and X. Y. Hou, *Chem. Phys. Lett.*, 2005, **416**, 42–46.
3 P. Vivo, J. Jukola, M. Ojala, V. Chukharev and H. Lemmetyinen, *Sol. Energy Mater. Sol. Cells*, 2008, **92**, 1416–1420.
4 (*a*) W. A. E. Omar, H. Haverinen and O. E. O. Hormi, *Tetrahedron*, 2009, **65**, 9707–9712; (*b*) J. P. Heiskanen, A. E. Tolkki, H. J. Lemmetyinen and O. E. O. Hormi, *J. Mater. Chem.*, 2011, **21**, 14766–14775.
5 A. Tolkki, K. Kaunisto, J. P. Heiskanen, W. A. E. Omar, K. Huttunen, S. Lehtimäki, O. E. O. Hormi and H. Lemmetyinen, *Thin Solid Films*, 2012, **520**, 4475–4481.
6 (*a*) Y.-K. Han and S. U. Lee, *Chem. Phys. Lett.*, 2002, **366**, 9–16; (*b*) V. A. Montes, R. Pohl, J. Shinar and P. Anzenbacher Jr, *Chem.–Eur. J.*, 2006, **12**, 4523–4535.
7 C. Hansch, A. Leo and R. W. Taft, *Chem. Rev.*, 1991, **91**, 165–195.
8 W. Tress, K. Leo and M. Riede, *Adv. Funct. Mater.*, 2011, **21**, 2140–2149.
9 (*a*) T. Wang, D. R. Magnin and L. G. Hamann, *Org. Lett.*, 2003, **5**, 897–900; (*b*) S. Hostyn, B. U. W. Maes, L. Pieters, G. L. F. Lemiere, P. Matyus, G. Hajos and R. A. Dommisse, *Tetrahedron*, 2005, **61**, 1571–1577; (*c*) J. A. Smith, R. K. Jones, G. W. Booker and S. M. Pyke, *J. Org. Chem.*, 2008, **73**, 8880–8892; (*d*) M. Fekete, M. Töröncsi and L. Novak, *Cent. Eur. J. Chem.*, 2008, **6**, 33–37; (*e*) J. Porter, S. Lumb, F. Lecomte, J. Reuberson, A. Foley, M. Calmiano, K. Riche, H. Edwards, J. Delgado, R. J. Franklin, J. M. Gascon-Simorte, A. Maloney, C. Meier and M. Batchelor, *Bioorg. Med. Chem. Lett.*, 2009, **19**, 397–400; (*f*) C. Ronco, L. Jean, H. Outaabout and P. Y. Renard, *Eur. J. Org. Chem.*, 2011, 302–310.
10 (*a*) B. A. Solaja, D. Opsenica, K. S. Smith, W. K. Milhous, N. Terzic, I. Opsenica, J. C. Burnett, J. Nuss, R. Gussio and S. J. Bavari, *J. Med. Chem.*, 2008, **51**, 4388–4391; (*b*) S. Ray, P. B. Madrid, P. Catz, S. E. LeValley, M. J. Furniss, L. L. Rausch, R. K. Guy, J. L. DeRisi, L. V. Iyer, C. E. Green and J. C. J. Mirsalis, *J. Med. Chem.*, 2010, **53**, 3685–3695.
11 8-(Benzyloxy)-5-bromoquinoline was synthesized in high yield (93%) by using the similar method described previously in the literature. See ref. 6*b*
12 (*a*) J. P. Wolfe, H. Tomori, J. P. Sadighi, J. Yin and S. L. Buchwald, *J. Org. Chem.*, 2000, **65**, 1158–1174; (*b*) S. R. Stauffer and J. F. Hartwig, *J. Am. Chem. Soc.*, 2003, **125**, 6977–6985; (*c*) A. Tewari, M. Hein, A. Zapf and M. Beller, *Tetrahedron*, 2005, **61**, 9705–9709.
13 L. L. Hill, L. R. Moore, R. Huang, R. Craciun, A. J. Vincent, D. A. Dixon, J. Chou, C. J. Woltermann and K. H. J. Shaughnessy, *J. Org. Chem.*, 2006, **71**, 5117–5125.
14 (*a*) J. F. Hartwig, M. Kawatsura, S. I. Hauk, K. H. Shaughnessy and L. M. Alcazar-Roman, *J. Org. Chem.*, 1999, **64**, 5575–5580; (*b*) R. Kuwano, M. Utsunomiya and J. F. Hartwig, *J. Org. Chem.*, 2002, **67**, 6479–6486.
15 L. L. Hill, J. M. Smith, W. S. Brown, L. R. Moore, P. Guevera, E. S. Pair, J. Porter, J. Chou, C. J. Wolterman, R. Cracium, D. A. Dixon and K. H. Shaughnessy, *Tetrahedron*, 2008, **64**, 6920–6934.
16 J. F. Hartwig, S. Richards, D. Baranano and F. Paul, *J. Am. Chem. Soc.*, 1996, **118**, 3626–3633.
17 H. Clavier and S. P. Nolan, *Chem. Commun.*, 2010, **46**, 841–861.
18 M. S. White, D. C. Olson, S. E. Shaheen, N. Kopidakis and D. S. Ginley, *Appl. Phys. Lett.*, 2006, **89**, 143517.
19 HOMO and LUMO levels of ZnO, P3HT and PCBM, see: (*a*) A. K. K. Kyaw, X. W. Sun, C. Y. Jiang, G. Q. Lo and D. W. Zhao, *Appl. Phys. Lett.*, 2008, **93**, 221107; Work function of Au, see: (*b*) E. Ito, Y. Washizu, N. Hayashi, H. Ishii, N. Matsuie, K. Tsuboi and Y. Ouchi, *J. Appl. Phys.*, 2002, **92**(12), 7306–7310.
20 H. H. Fong and S. K. So, *J. Appl. Phys.*, 2006, **100**, 094502.
21 M.-S. Kim, B.-G. Kim and J. Kim, *ACS Appl. Mater. Interfaces*, 2009, **1**(6), 1264–1269.
22 R. R. Gagne, C. A. Koval and G. C. Lisensky, *Inorg. Chem.*, 1980, **19**, 2854–2855.
23 A. Tolkki, E. Vuorimaa, V. Chukharev, H. Lemmetyinen, P. Ihalainen, J. Peltonen, V. Dehm and F. Würthner, *Langmuir*, 2010, **26**(9), 6630–6637.

Publication II

Conjugated donor-acceptor (D-A) copolymers in inverted organic solar cells – a combined experimental and modelling study

Venla Manninen, Mika Niskanen, Terttu I. Hukka, Felix Pasker, Simon Claus, Sigurd Höger, Jinseok Baek, Tomokazu Umeyama, Hiroshi Imahori and Helge Lemmetyinen

J. Mater. Chem. A, **2013**, *1*, 7451 – 7462.

Journal of Materials Chemistry A

RSC Publishing

PAPER

Conjugated donor–acceptor (D–A) copolymers in inverted organic solar cells – a combined experimental and modelling study†

Cite this: *J. Mater. Chem. A*, 2013, **1**, 7451

Venla Manninen,*[a] Mika Niskanen,[a] Terttu I. Hukka,[a] Felix Pasker,[b] Simon Claus,[b] Sigurd Höger,[b] Jinseok Baek,[c] Tomokazu Umeyama,[c] Hiroshi Imahori[c] and Helge Lemmetyinen[a]

Received 15th February 2013
Accepted 29th April 2013

DOI: 10.1039/c3ta10686a

www.rsc.org/MaterialsA

Quantum chemical methods are useful for materials design to improve the performance of organic bulk heterojunction (BHJ) solar cells. However, more integrated studies of quantum chemical modelling and experimental results need to be performed to further improve both the materials design and understanding of the related photo-induced processes and photocurrent generation. In this work we investigated the internal relationship between the molecular structures of four donor–acceptor (D–A) copolymers (P1–P4) and their photovoltaic performances. The effects of the molecular structures on the generation of photo-induced charge carriers, exciton diffusion, dissociation and carrier transmission were compared by combining density functional theory (DFT) calculations of intrinsic geometric, electronic and optical properties with the results of electrochemical, spectroscopic, thermal, AFM and solar cell measurements of the polymers. The quantum chemical methods, which provided a tool to assess the electronic properties and conjugation length in the polymers, highly support the experimental results and therefore the usefulness of quantum chemistry for solar cell materials design.

Introduction

Copolymers with electron rich and electron deficient moieties alternating along the polymer backbone have performed well as electron donors in polymer solar cells. By adding different substituents to the polymer backbone, the redox and structural properties of the polymer can be controlled, which offers a method for preparing tailored low band gap (LBG) polymers for photovoltaic applications. Benzodithiophene derivatives as the electron rich unit have demonstrated excellent photovoltaic properties as tunable electron donors,[1–7] whereas benzotriazole with various substituents has been used as an electron acceptor[8–11] in LBG donor–acceptor (D–A) polymers. Intramolecular charge transfer (ICT) properties of tailored LBG copolymers based on alternating benzodithiophene and benzotriazole derivatives have demonstrated excellent photovoltaic properties in D–A polymers, which have been studied experimentally in the conventional indium tin oxide (ITO)|poly(3,4-ethylenedioxythiophene)–poly(styrenesulfonate) (PEDOT:PSS)|polymer:[6,6]-phenyl-C_{60}-butyric acid methyl ester ($PC_{60/70}BM$)|Ca|Al organic bulk-heterojunction (BHJ) solar cells.[12,13]

The photocurrent generation in organic BHJ solar cells takes place in both polymer and fullerene phases and is initiated by photoexcitation and formation of excitons. During their lifetime, prior to decay back to the ground state, the excitons need to diffuse to the donor–acceptor interface for dissociation. The Coulombic binding potential of excitons has to be overcome through differences in the chemical potentials of the hole transporting material (HTM) and the electron transporting material (ETM). The separated charged polarons, the electron and the hole, migrate through the HTM and ETM phases and are collected at the electrodes. Photocurrent generation is a stepwise process, where all the principal stages need to be optimized to produce photocurrent efficiently. Therefore, the essential qualifications have been established for the design and intrinsic material properties of HTM polymers. A planar structure of the polymer backbone is desired to decrease the band gap energy (E_g) around 1.77 eV,[14] to shift the polymer absorption to the red towards the maximum intensity range of the solar irradiation, and to minimize the reorganization energy upon excitation. Also, suitable energy levels are necessary for efficient charge transfer, charge separation at the HTM/ETM interface and charge collection at the electrodes.

[a]Department of Chemistry and Bioengineering, Tampere University of Technology, P. O. Box 541, FI-33101, Tampere, Finland. E-mail: venla.manninen@tut.fi; Fax: +358 3 3115 2108

[b]Kekulé-Institut für Organische Chemie und Biochemie, Rheinische Friedrich-Wilhelms-Universität Bonn, Gerhard-Domagk-Str. 1, 53121 Bonn, Germany

[c]Department of Molecular Engineering, Institute for Integrated Cell-Materials Sciences (WPI-iCeMS), Graduate School of Engineering, Kyoto University, Nishikyo-ku, Kyoto 615-8510, Japan

† Electronic supplementary information (ESI) available: ^{1}H and ^{19}F NMR spectra, CV, TCSPC, DSC, R_s, R_{sh}, N_{MCC} and HOMO–LUMO gaps. See DOI: 10.1039/c3ta10686a

In addition to experimental methods, properties of conjugated polymers as donor materials can be studied computationally. Information can be obtained about polymer chain geometries, orbitals, HOMO and LUMO energies, electron affinities, ionization potentials, effective conjugation lengths, and various excited state properties.[15–27] While many of these properties are accessible through experiments, combining the methods gives more details on the performance of the chosen polymers as donor materials. In a real bulk system, intermolecular interactions affect the polymer chain geometry and its properties. However, modeling of the polymer bulk and donor–acceptor interfaces is difficult, because the areas of interest are likely to contain thousands of atoms. Moreover, the periodic boundary conditions cannot be effectively used, as the materials are often amorphous or semicrystalline, consisting of only small crystalline domains. The systems are often too big for density functional theory (DFT) and correlated method calculations, whereas semiempirical methods are often not accurate enough for such complex systems. As a result, most commonly only isolated polymer chains are studied computationally and the models are either short oligomeric chains[15–17] or infinite polymers that are built using periodic boundary conditions.[28–33] When oligomeric models are used the polymer properties can be obtained by presenting the results as a function of inverse constitutional repeating units ($1/n$) and extrapolating.[15,34–36]

In this work, the relationship between the molecular structures of four different donor–acceptor (D–A) copolymers (P1–P4) and their photovoltaic performances is investigated. To this aim, a new polymer (P4, Fig. 1) with alternating benzodithiophene and benzotriazole moieties was synthesized, characterized and used as a donor material in inverted[37] ITO|zinc oxide (ZnO)|polymer:$PC_{60}BM$/$PC_{70}BM$|*tris*-(8-hydroxyquinoline)-aluminum (Alq_3)|Au (Fig. 2) organic solar cells. P4 was compared with three previously studied[38] D–A donor polymers containing 2-aryl-2*H*-benzotriazoles and bis(thiopheno)dialkylfluorenes (P1–P3, Fig. 1). The well-known donor material, poly(3-hexylthiophene) (P3HT, Fig. 2), was used as a reference polymer.

The intrinsic material properties of the D–A polymers were studied with DFT using oligomeric and periodic isolated chain models. The geometries, HOMO and LUMO levels, molecular orbitals and lowest energy excitations of the polymers were computed and the results were combined with the experimental data to get a better understanding of the relationship between the photovoltaic performance and molecular structures. In addition, active layer structures of the solar cells were analyzed using AFM. Eventually, the stabilities of the prepared cells were compared six months after the cell preparation. This is possible due to the long lifetime of inverted structure organic solar cells with an air-stable Au anode.

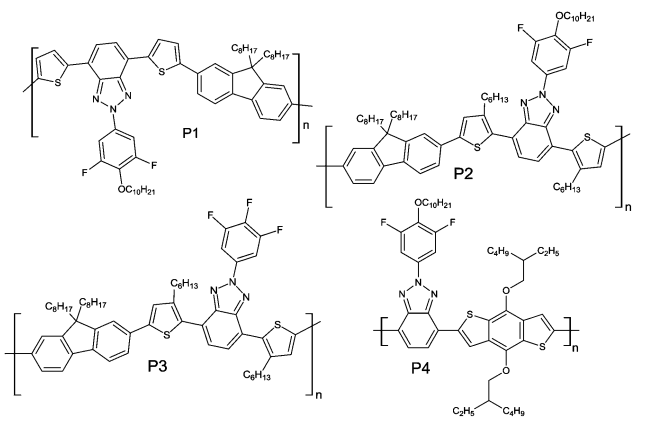

Fig. 1 Chemical structures of the polymers P1–P4.

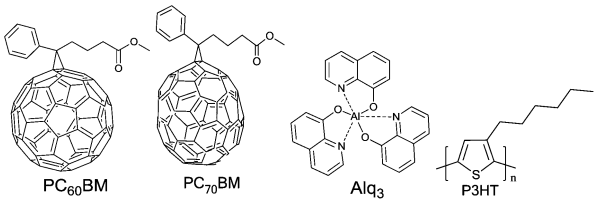

Fig. 2 Chemical structures of $PC_{60}BM$, $PC_{70}BM$, Alq_3 and reference polymer P3HT.

Photovoltaic performance

The polymers were tested as donor materials in inverted ITO|ZnO|polymer:PCBM|Alq_3|Au solar cells using the well-known P3HT:$PC_{60}BM$ as a reference cell. Energy levels of the materials of the constructed solar cells are important for the cell performance. The energy level diagram for the cell materials is shown in Fig. 3, where both the experimental (CV of P4, see ESI†) and computational values of the HOMO and LUMO energy levels are presented. Because the LUMO energy levels of the donor polymers are higher than those of the acceptor fullerene derivatives, each polymer is expected to be able to donate electrons to the acceptor molecules in the cell structure. Alq_3 as a buffer layer prevents efficiently the unwanted flux of electrons to the direction of the metal (Au) anode. In addition, the HOMO levels of the polymers do not differ remarkably from each other. Thus, the open circuit voltage (V_{OC}), which is proportional to the

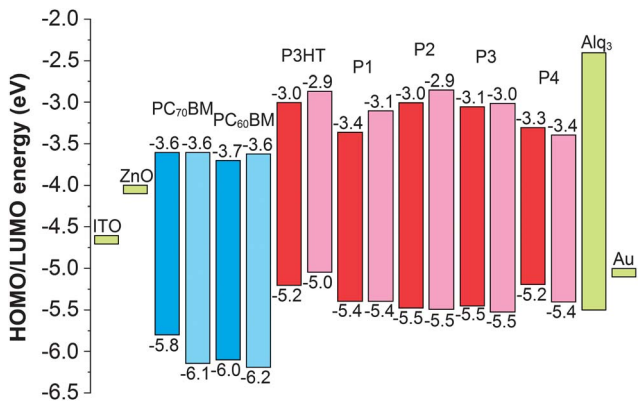

Fig. 3 Energy level diagram of the donor molecules (red), acceptor molecules (blue), buffer layer materials (green) and electrodes (green) used in the organic solar cells.[39] The experimental values are shown in dark blue/red and the modeled values in light blue/red.

energy difference between the HOMO of the donor and the LUMO of the acceptor, should not vary remarkably between different donor–acceptor combinations.

Photovoltaic parameters of the prepared solar cells using P1, P2 and P4 as donor materials, measured the following day after the cell preparation, are presented in Table 1 and the corresponding *I–V* curves are shown in Fig. 4. The cell efficiency using P3 as a donor material was negligible and therefore it is not included in the solar cell results, but P3 was kept in the calculations to allow comparison.

P1–P3 have been tested earlier in conventional ITO|PEDOT:PSS|polymer:$PC_{60}BM$|Ca|Al solar cells,[38] in which case the reported η values were higher than here in the case of inverted solar cells. The reasons for this could be that the certified measuring system could not be applied when measuring the inverted solar cells studied here. Also, different cell efficiencies for the same polymer, P3HT, have been reported depending on the cell structure. The average η for the P3HT:PCBM BHJ solar cells reported during the years 2002–2010 is around 3%.[40] In the conventional P3HT:$PC_{60}BM$ cell structure the values of η are from 3% to 4%,[41,42] whereas in the inverted cell structure the reported η values are slightly lower, *i.e.* 2% to 3%.[39b,d,e,43,44] In this article, the polymers are used in the inverted cell structure and therefore the efficiencies of different polymers as donor materials can be compared and discussed.

Table 1 Photovoltaic parameters of the solar cells containing P3HT, P1, P2 or P4 as donors and $PC_{60}BM$ or $PC_{70}BM$ as acceptors measured the following day after the cell preparation

Active layer components (film thickness, nm)	Mass ratio polymer: PCBM	J_{sc} (mA cm^{-2})	V_{oc} (V)	FF (%)	η_{best} (%)	η_{avg} (%)
P3HT:$PC_{60}BM$ (100)	1.26 : 1	−3.09	0.52	68.96	3.04	2.47
P1:$PC_{60}BM$ (65)	1 : 3.99	−1.53	0.48	42.35	0.83	0.58
P1:$PC_{70}BM$ (55)	1 : 4.63	−0.73	0.34	40.31	0.27	0.25
P2:$PC_{60}BM$ (130)	1 : 4.14	−0.65	0.43	28.86	0.21	0.12
P4:$PC_{60}BM$ (40)	1 : 2.69	−1.17	0.45	41.18	0.57	0.43
P4:$PC_{70}BM$ (30)	1 : 3.09	−1.13	0.41	58.71	0.74	0.66

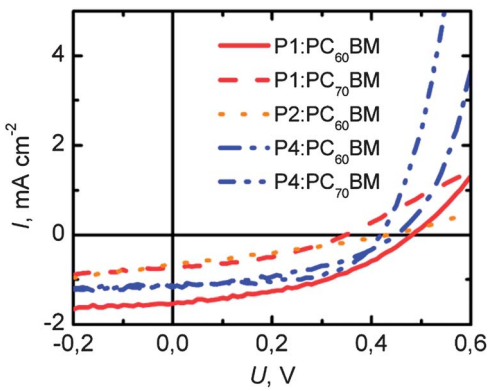

Fig. 4 *I–V* curves of the P1/P2/P4:$PC_{60}BM$/$PC_{70}BM$ cells measured the following day after the cell preparation.

The efficiencies of the solar cells differ remarkably depending on the donor–acceptor combinations, which cannot be explained in terms of the energy levels of the compounds. For example, based on the energy difference between the HOMO of the donor and the LUMO of the acceptor (Fig. 3), a higher V_{OC} could be expected for the P1:$PC_{60}BM$ cell than that for the P3HT:$PC_{60}BM$ cell. However, the former has a lower V_{OC}, 0.48 V, than the latter, 0.52 V. Similarly, the same V_{OC} values could be expected for the P3HT:$PC_{60}BM$ and P4:$PC_{60}BM$ cells, because of the same measured HOMO energies (−5.2 eV) of the donor polymers. Nevertheless, V_{OC} values are different, 0.52 V and 0.45 V for P3HT and P4, respectively. In the cases of P1 and P4 the donor polymers give very different efficiencies depending on the acceptors, $PC_{60}BM$ or $PC_{70}BM$, even though the acceptors have almost the same HOMO and LUMO energies. For understanding these discrepancies a closer quantum mechanical insight into the polymers' molecular geometry, electronic structure and donor–acceptor interaction is necessary.

Modelling of the polymer geometry and electronic structure related properties

In the computational models of P1–P4 the solubility enhancing long alkyl side chains, $-OC_{10}H_{21}$, $-OCH_2CH(C_2H_5)C_4H_9$, $-C_6H_{13}$ and $-C_8H_{17}$ were replaced by short side chains, *i.e.* $-OCH_3$ and $-CH_3$, respectively. This reduced the computational time and allowed modeling of oligomeric chains up to $n = 7$–8 and thus investigation of the convergence of the HOMO–LUMO gaps. The periodic models were built based on the optimized oligomer structures. The constitutional repeating unit (CRU) of P1 is bent due to the dithiophene 2-phenyl benzotriazole moiety so the periodic P1 model was built from two P1 CRUs which create a zigzagging, almost planar polymer backbone. The methyl substituents of the two 3-methylthiophene rings in the CRU enlarge the backbone dihedral angles in P2 and P3, which prohibits planarity. As a result, it is expected that the π-conjugation weakens or is broken at some points in the backbones of the P2 and P3 polymers. For these polymers the periodic models were constructed of three CRUs, which create a helical backbone. We note, however, that there are ways to build alternative periodic models for P2 and P3. The periodic model of P4 consists of a linear and almost planar single CRU. The fully optimized periodic models are presented in Fig. 5.

The geometries of the oligomeric and periodic models with full side chains were also fully optimized to compare the backbone dihedral angles to those of the models with short side chains. The backbone dihedral angles of P1 and P4 did not change. However, those of P2 and P3 increased due to the steric effects caused by the hexyl substituents of the two 3-hexylthiophenes.

Energy level gaps, orbitals and TD-DFT calculations

The HOMO–LUMO gaps of the short side chain oligomeric models and the gaps between the highest occupied crystal orbital and the lowest unoccupied crystal orbital (the HOCO–LUCO gap) of the short side chain periodic models were examined. The HOMO–LUMO gap energies of oligomers

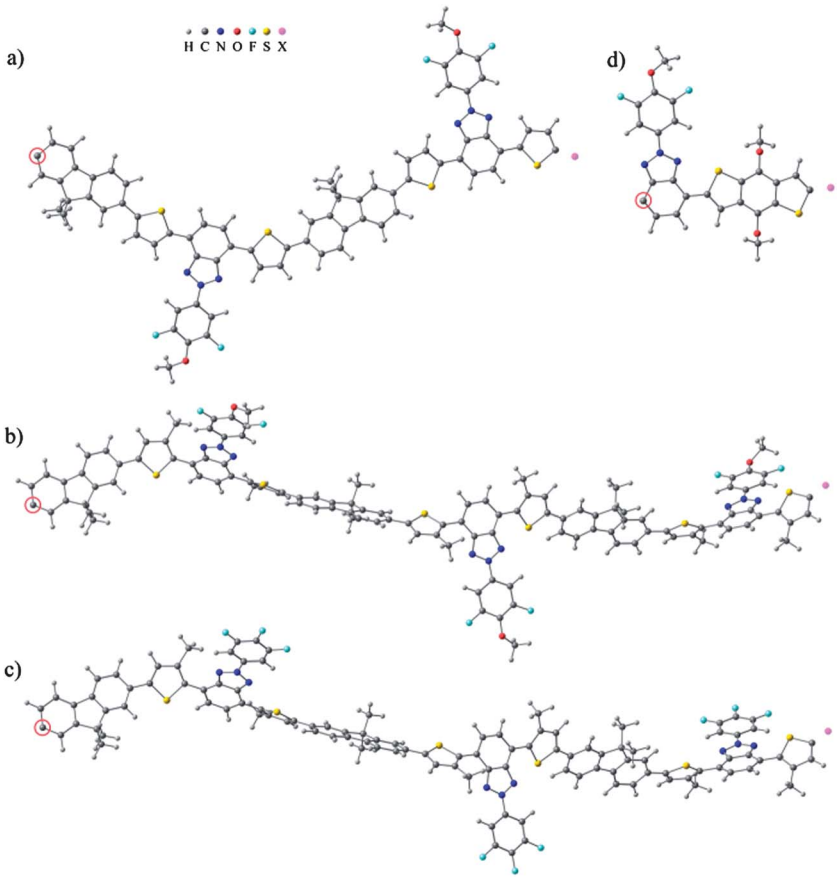

Fig. 5 Periodic models of (a) P1, (b) P2, (c) P3 and (d) P4. The repeating structure is copied and translated from the circled carbon atom to the position marked as a pink dummy-atom.

approach the HOCO–LUCO gap energies of the periodic models as the oligomer length is increased (see ESI, Table S3†), so the HOCO–LUCO gaps are taken as final computational results for the P1–P4 polymers. The HOCO–LUCO gaps were direct band gaps. The computational energies were shifted by subtracting 0.62 eV from the values so that the computational HOCO and experimental HOMO levels of P1 are equal. The shifted HOCO and LUCO energies based on the periodic calculations are presented and compared to the experimental HOMO and LUMO energies in Fig. 3. The HOCO–LUCO gaps are systematically only a bit larger (0.12 eV to 0.26 eV) than the experimental values obtained by cyclic voltammetry, and the agreement between the energy levels is qualitatively good.

The HOMO–LUMO gaps of the short oligomers and the HOCO–LUCO gaps of the periodic models with the full side chains were examined as well. Incorporating the full side chains does not change the gaps of P1 and P4 in the longest oligomers and periodic models, but the gap increases slightly in the case of P2 (0.08 eV) and P3 (0.06 eV) due to increased steric stress caused by the 3-hexylthiophene moieties that hinder the π-conjugation.

Next, the frontier molecular orbitals of P1–P4 were analysed. The D–A polymers consist of electron rich and electron deficient moieties to achieve a narrower HOMO–LUMO gap. The CRUs of P1, P2 and P3 are composed of three different building blocks, of which fluorene and thiophene derivatives are the electron rich moieties and 2-phenyl benzotriazole derivatives are the electron deficient moieties. In P4 the electron rich moiety is the benzodithiophene derivative and the electron deficient moiety is the 2-phenyl benzotriazole derivative. Periodic models are used to calculate and visualize the orbitals. This way the CRUs along the polymer backbone have the same orbital energy levels and the molecular orbitals are distributed equally in the CRUs along the infinite, non-terminating polymer chain. The orbitals are presented in Fig. 6 and the contributions to the orbitals from different backbone fragments are presented in Table 2. In P1, P2 and P3 the HOCO is evenly distributed, *i.e.* delocalized, along the polymer backbone whereas the LUCO is much more localized on the 2-phenyl benzotriazole moieties, particularly in P2 and P3. In the case of P2 and P3, localization most probably results from a weaker π-conjugation along the polymer backbone, as suggested above. In P4 both HOCO and LUCO are evenly delocalized along the polymer backbone, although the LUCO spreads further into the 2-phenyl benzotriazole derivative. The differences in localizations of the LUCOs are expected to affect the exciton diffusions in P1–P4, because the LUCO is partly occupied in excitation and participates in exciton diffusion.

The effect of the length of the oligomer on the first excitation energy and its composition was studied by time-dependent

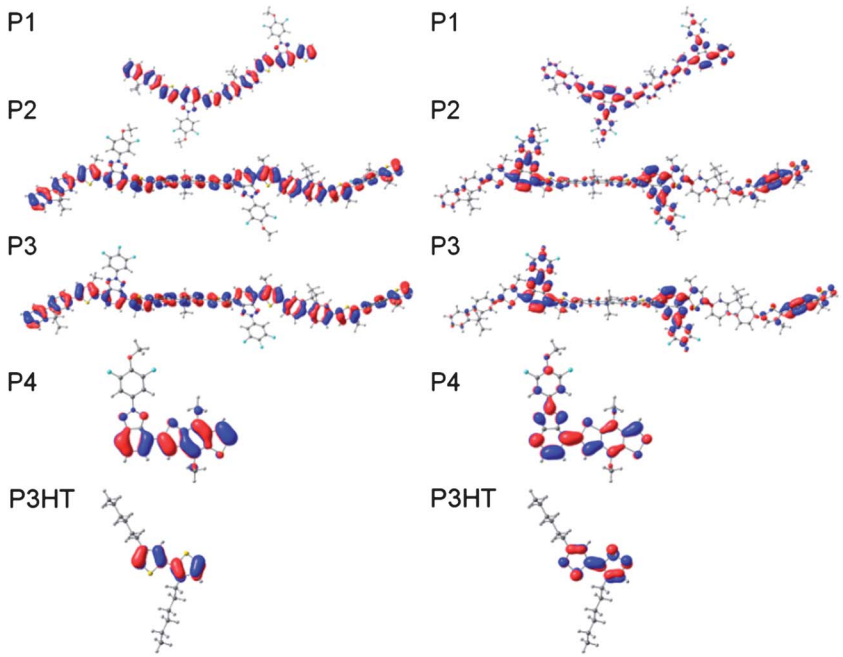

Fig. 6 The HOCO (left) and LUCO (right) of the P1–P4 polymers and P3HT.

density functional theory (TD-DFT). The calculated excitation energies are given in Table 3. As the length of the oligomer is increased, the first excitation energy gets smaller. However, with the longest calculated oligomers the TD-DFT results underestimate the excitation energy. This is rather common for B3LYP and usually, if TD-DFT results matching the experimental values are desired, PBE0 or novel functionals are used together with a solvation model. Additionally, the used basis set is rather small. Comparative calculations using the 6-311+G* basis set are presented in the ESI.† The orbital contributions of the first excitation were examined to justify the use of the HOCO–LUCO gap as the lowest excitation energy of the polymer. For all oligomers the main component of the first excitation was found to be from the HOMO to the LUMO. The HOMO to LUMO contribution remains dominant (>70% in P4, $n = 8$) in the total excitation as the length of the oligomer increases, but other contributions, such as HOMO-1 to LUMO + 1 appear as well, as they get closer to the energy of HOMO–LUMO transition. These orbitals are typical for the low energy excitations of conjugated systems, which contain π and π^* orbitals.

Table 3 Excitation energies (eV) of the first excitation of oligomers with TD-DFT

	$n = 1$	$n = 2$	$n = 3$	$n = 4$	$n = 5$	$n = 6$	$n = 7$	$n = 8$	E_g^{ec}	E_g^{opt}
P1	2.44	2.16	2.07	2.03	2.02	1.99	—	—	2.03	2.08
P2	2.63	2.42	2.37	2.34	2.33	2.31	—	—	2.47	2.34
P3	2.55	2.35	2.30	2.27	2.26	2.26	—	—	2.40	2.30
P4	2.66	2.20	2.01	1.91	1.86	1.83	1.81	1.80	1.89	1.91

Maximum conducive chain length

The maximum conducive chain length (N_{MCC})[35] was calculated using the DFT results to compare the conjugation degree of the polymers. For this method the HOMO–LUMO gaps were plotted as a function of $1/N$ (N is the number of double bonds along the shortest path of the polymer backbone). The infinite polymer HOMO–LUMO band gap was extrapolated for each polymer from the oligomer results. Polynomial fits were used for the extrapolation. The third degree polynomial fits described the plots of the HOMO–LUMO gaps of the oligomers well and

Table 2 Contributions (%) of the backbone fragments of the polymers to the HOCO and LUCO

	HOCO			LUCO		
	Electron rich		Electron deficient	Electron rich		Electron deficient
	Fluorene	Thiophene	Benzotriazole	Fluorene	Thiophene	Benzotriazole
P1	31.0	46.3	22.7	15.2	29.0	55.8
P2	34.2	48.1	17.7	11.5	23.6	64.9
P3	35.1	47.9	17.0	9.4	21.0	69.6
	Benzodithiophene			Benzodithiophene		
P4	73.8		26.2	40.4		59.6

leveled as they approached $x = 0$. The polynomial fits and extrapolated gaps are given in the ESI.† The $1/N_{MCC}$ value was obtained from the intersection of the line $y(x) = b$ drawn from the extrapolated HOMO–LUMO gap of an infinite polymer and a line drawn through the steepest descending part of the HOMO–LUMO plot (see ESI, Fig. S11†). The extrapolated HOMO–LUMO gaps were used for all polymers, because the oligomeric series did not approach the periodic values exactly for P2 and P3, though the differences were small (≤0.05 eV). A likely explanation for the differences is the flexibility of the P2 and P3 oligomeric models compared to the periodic models. The N_{MCC} can be obtained accurately for polymers with short CRUs. However, as the number of double bonds increases in the CRU, less data points are available for the fitting procedure. This can cause problems if the non-saturated region, where the HOMO–LUMO gap values drop fast, has only one or two data points. The method seems to work reliably for P1 and P4, but for P2 and P3 it is likely that the excitation energy saturates too fast (see ESI). Thus the N_{MCC} values for P2 and P3 should be considered as upper limits rather than exact values. The obtained N_{MCC} values are 62 for P1, ≤ 47 for P2, ≤ 37 for P3 and 59 for P4. We can see that P1 and P4 have higher N_{MCC} values than P2 and P3. Also, the conjugation can be expected to be more expanded in P1 and P4 because the HOMO–LUMO gap of their oligomers approaches the infinite polymer limit more slowly. Typically the N_{MCC} values are much lower, in the range of 18–22 in conjugated polymer chains.[35] Possible reasons for the high N_{MCC} values obtained are the donor–acceptor architecture as well as the large CRU sizes of the studied polymers.

Polymer–PCBM interactions

Single P1 and P4 monomers with full side chains were studied together with the molecular $PC_{60}BM$ and $PC_{70}BM$ acceptors in combined models to see how their interaction affects the energy levels. The energy levels of the combined models were compared to the energy levels of the isolated monomers and PCBMs. The PCBMs were arranged in three completely different positions: (i) close to the side chains away from the main backbone, (ii) close to the electron rich moiety of the monomer and (iii) close to the electron deficient moiety of the monomer (Fig. 7), and the models were fully optimized.

The obtained molecular orbital energies are presented in Fig. 8. Bringing either $PC_{60}BM$ or $PC_{70}BM$ close to the polymer monomer changes the HOMO and LUMO values of the PCBMs and monomers slightly, *i.e.* −0.13 eV to +0.09 eV, compared to the isolated PCBMs and monomers. The P1 monomer behaves similarly with both $PC_{60}BM$ and $PC_{70}BM$. The P4 monomer, however, behaves differently depending on the PCBMs (see Fig. 8). The largest changes in energies are observed in the model consisting of the P4 monomer and $PC_{70}BM$. Both the HOMO and LUMO energies of $PC_{70}BM$ increase and those of P4 decrease, which leads to a larger P4 monomer HOMO–$PC_{70}BM$ LUMO gap when $PC_{70}BM$ is close to either the electron rich or the electron deficient moiety of the P4 monomer. While the molecular model cannot describe the real interfaces of an active material, it can be seen that interaction of the donor and acceptor changes the energy levels of both molecules and affects the electronic properties.

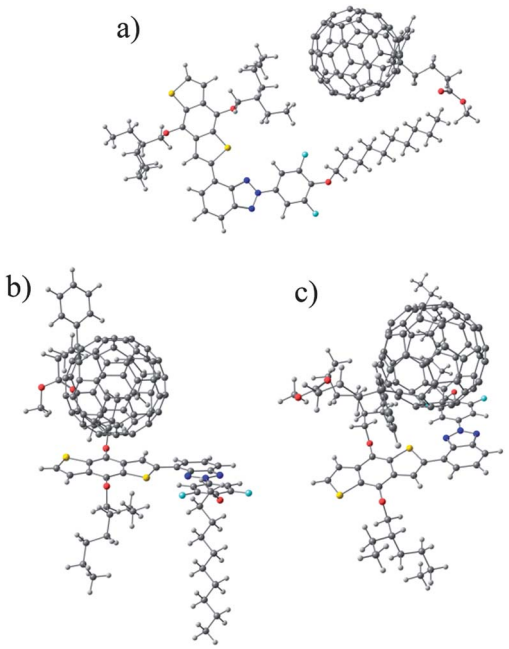

Fig. 7 Models where PCBM is close to (a) the side chains of P4, (b) the electron rich moiety of P4 and (c) the electron deficient moiety of P4.

Relationship between the photovoltaic performance and molecular structures of the donor polymers

The first prerequisite to produce photocurrent is the absorption of light to generate excitons. The overall cell absorption (Fig. 12) initiates from the absorption of the intrinsic donor and acceptor materials, which are presented in Fig. 9. The absorption maximum of P4, at 612 nm, is remarkably red-shifted compared to those of P2 and P3, at 443 nm and 448 nm respectively, and that of P1, at 537 nm. As shown in Fig. 5, the backbones of P2 and P3 are helical due to the steric hindrance of the hexyl chains attached to the thiophene rings, which weakens the π-conjugation in the polymer backbone. The structure of P1 is zigzagging, but planar, due to missing hexyl chains. Therefore π-conjugation is stronger and absorption of P1 is red-shifted compared to P2 and P3. A more planar structure of P4 compared to those of P1–P3 was achieved by exclusion of the thiophene moieties from the polymer backbone. In the nearly planar backbone of P4 the conjugation is the strongest and absorption of photons becomes possible at longer wavelengths (>600 nm) compared to P1–P3.

The absorption of $PC_{60}BM$ covers effectively the wavelengths up to 400 nm in $CHCl_3$ solution, whereas $PC_{70}BM$ absorbs at a wider wavelength range up to 700 nm. The absorptions of P1–P3 overlap widely with the absorptions of both $PC_{60}BM$ and $PC_{70}BM$. Absorption of P4 takes place at longer wavelengths and it does not overlap with the absorptions of $PC_{60}BM$ and $PC_{70}BM$ as widely as the three other polymers. Therefore, photons over a wider wavelength range up to 700 nm will be collected by the

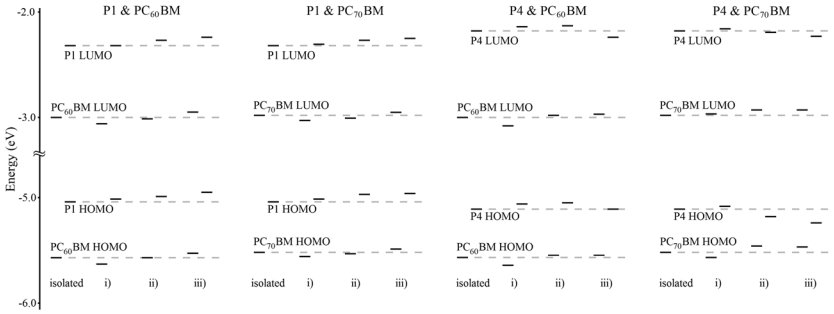

Fig. 8 Molecular orbital energies of the isolated monomers, PCBMs and combined models.

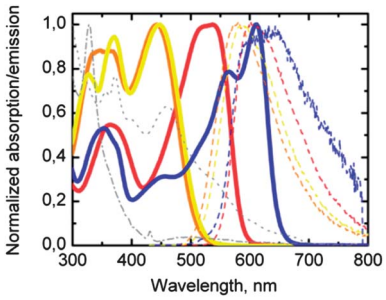

Fig. 9 Normalized absorption (solid lines) and emission (dashed lines, $\lambda_{ex} = 485$ nm) of the donor polymers P1 (red), P2 (orange), P3 (yellow) and P4 (blue) and absorption of the acceptors $PC_{60}BM$ (dash-dotted line) and $PC_{70}BM$ (dotted line) in $CHCl_3$.

solar cell with P4 compared to the other cells with P1–P3 as the donor material.

In addition to a wider range of absorption a planar and rigid backbone is desired to prevent energy losses caused by reorganization upon excitation. The molecular frontier orbitals (Fig. 6) show that the LUMO orbitals promote planar structure. Therefore, the energy losses, *i.e.* Stokes shifts (Table 4), of P2 and P3 are remarkably larger than those of P1 and P4.

After excitation the excitons need to diffuse to the donor–acceptor interface along the polymer phase. Therefore excited state properties of the polymers have a principal effect on the exciton diffusion. The lifetime of the excited state defines the diffusion duration. The exciton diffusion effectivity *i.e.* the speed of the exciton, together with the lifetime, defines the diffusion length. The lifetime of P4, 2.14 ns, is longer than those of P1–P3, 1.64 ns, 1.10 ns and 1.00 ns, respectively (see ESI, TCSPC†). The exciton diffusion effectivity in the excited state of the polymers can be compared based on the molecular frontier orbitals shown in Fig. 6. The LUMOs of P2 and P3 are strongly located in the benzotriazole moieties of the polymer backbones and the orbitals are not continuous. Therefore, the exciton diffusion length in the excited states of P2 and P3 might be decreased if the excitons are trapped in the LUMO orbital spatial gaps. The LUMO orbitals of P1 and P4 have continuous electron density throughout the polymer backbones. Also, the calculated N_{MCC} values of P1 and P4, 62 and 59 respectively, are larger than those of P2 and P3, 47 and 37 respectively. N_{MCC} values correlate with the conjugation length in the polymer backbones. Thus, excitons can be expected to diffuse further in P1 and P4 than in P2 and P3.

Table 4 Stokes shifts and band gap energy differences of P1–P4

Polymer	Stokes shift (nm)	$E_g^{ec} - E_g^{opt}$ [a] (eV)
P1	55	−0.05
P2	107	0.13
P3	114	0.1
P4	87	−0.02

[a] See ESI for P4 and ref. 38 for P1–P3.

Next, after exciton diffusion to the donor–acceptor interface, the Coulombic binding energy of excitons has to be overcome to separate the charges. Due to the red-shifted absorption the optical band gap of P4, 1.91 eV, calculated from the onset wavelength of the absorption spectrum, is smaller than those of P1–P3, 2.08 eV, 2.34 eV and 2.30 eV, respectively. The difference in the band gap energies measured by using the transport technique (CV) and optical excitation, $E_g^{ec} - E_g^{opt}$, can be directly correlated with the exciton binding energy (E_B)[45] and the conjugation length in a polymer.[46] The bigger the difference in the band gap energy, the higher the exciton binding energy and the shorter the conjugation length. The values of $E_g^{ec} - E_g^{opt}$ (Table 4) in the cases of P1 and P4 are close to zero, within the error of experiments, and smaller than those of P2 and P3. Thus, less energy is needed to separate the excitons created in P1 and P4 than in P2 and P3.

The emission spectra of the combined polymer:PCBM films, the intensity of which is corrected according to the absorbance of the films, are presented in Fig. 10. The emission of P1 from 675 nm to 775 nm is more efficiently quenched with $PC_{60}BM$ than with $PC_{70}BM$. This predicts better electron transfer from P1 to $PC_{60}BM$ than to $PC_{70}BM$, which can be also seen as an increase in the $PC_{60}BM$ acceptor emission from 550 nm to 650 nm. The emission of P4 from 600 nm to 700 nm is more efficiently quenched with $PC_{70}BM$ than with $PC_{60}BM$, which supports better electron transfer from P4 to $PC_{70}BM$ than to $PC_{60}BM$. The fluorescence decay curves of the combined films are shown in the ESI (Fig. S12).†

Eventually, the separated charge carriers are transported to the electrodes along the ETM and HTM paths in the BHJ layer. The carrier transport in the ETM and HTM together with the morphology of the phase-separated network governs the

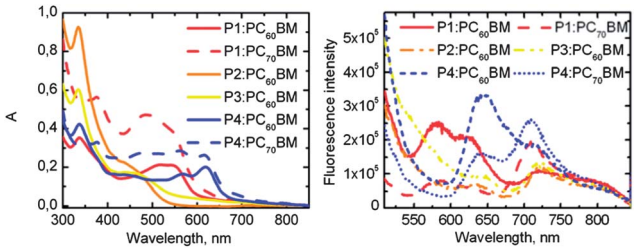

Fig. 10 Absorption and emission (corrected according to absorbance) spectra of the polymer:PCBM photoactive layers.

transport. The HOMOs of P1–P4 are relevant for the hole transport in the materials. Our models do not include thermal motion that would change the energy of CRUs with respect to each other, so the obtained HOMO electron densities are rather evenly distributed (Table 2). However, longer conjugation along the backbones leads to better hole transport in P1 and P4 than in P2 and P3, as in the latter, backbone twists are more likely and may create hole traps.

The differences in the molecular structures of the polymers lead to differences in phase separation and morphology in the interpenetrating network of the BHJ structures. A rough insight into the active layer morphology was achieved by the AFM images of the cells (Fig. 11). Usually, small roughness (RMS = root mean square) values and small grain features are correlated with enhanced crystallinity, which offers better energy conversion efficiency.[47] Based on the DSC measurements of P1–P4 (see ESI† and ref. 38), there are no remarkable differences in the crystallinity, but P4 is thermodynamically more stable than P1–P3. Therefore, RMS values are valuable for estimating the morphology of the BHJ structure formed by the polymers. The RMS value of P1:$PC_{70}BM$, 1.92 nm, is significantly larger than that of the P1:$PC_{60}BM$ film, 0.45 nm. Large aggregates with large grain features can be seen in the P1:$PC_{70}BM$ film. Aggregation may lead to current losses due to excessively long conduction paths compared to the exciton diffusion length in the P1:$PC_{70}BM$ film. Therefore, the excitons created in the P1:$PC_{70}BM$ cell recombine before reaching the donor–acceptor interface more probably than in the P1:$PC_{60}BM$ cell, and the P1:$PC_{60}BM$ cell ($\eta = 0.80\%$) worked better than the P1:$PC_{70}BM$ cell ($\eta = 0.35\%$). In the case of P2 the active layer morphology formed by P2:$PC_{60}BM$ seems fairly uniform. Thus, it seems that P2 is capable of forming a good quality BHJ layer with $PC_{60}BM$. However, as discussed before, due to the gaps in the LUMO and small N_{MCC} values, both exciton and charge transfer are inefficient in P2 and the performance of the cell remains low ($\eta = 0.12\%$). Active layer morphologies of the P4:$PC_{60}BM$ and P4:$PC_{70}BM$ cells appear very similar, and also the RMS values, 0.92 and 0.94 respectively, are practically the same. Thus, the film formation properties do not seem to cause the difference between the performances of the P4:$PC_{60}BM$ ($\eta = 0.33\%$) and P4:$PC_{70}BM$ ($\eta = 1.03\%$) cells. Because $PC_{60}BM$ absorbs efficiently only up to 400 nm, the absorption and the exciton formation of the P4:$PC_{60}BM$ solar cell device will mainly take place in the P4 donor phase, whereas in the P4:$PC_{70}BM$ device both the donor and the acceptor participate in the exciton creation. Even though the combined film of P4:$PC_{70}BM$ is thinner (30 nm) than the P4:$PC_{60}BM$ film (40 nm), the superiority of P4:$PC_{70}BM$ is caused by the higher absorption of the cell.

Lastly, the EPCEs of the cells show (see Fig. 12) how efficiently absorption of photons leads to current production. The absorption of the cells with P1 is remarkably higher than that of

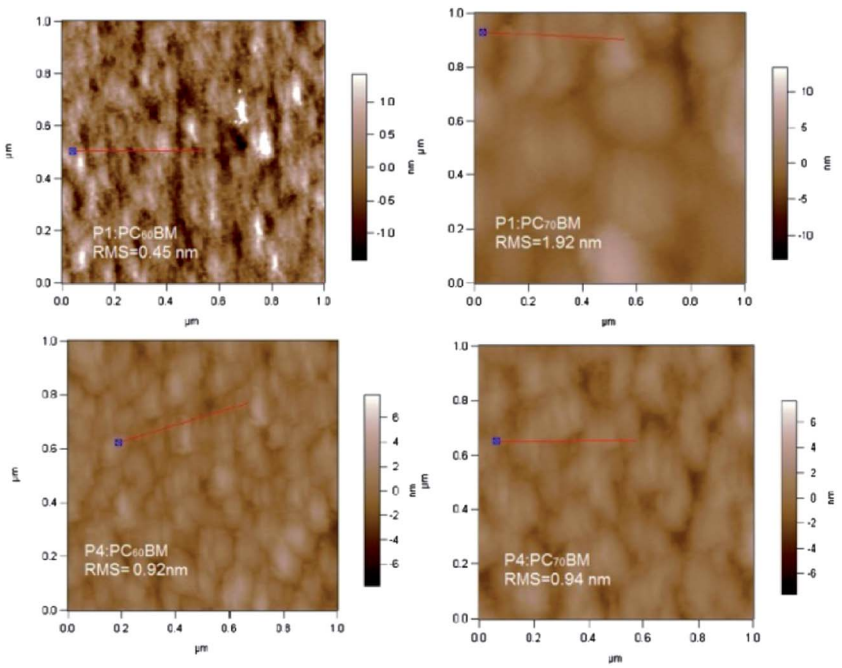

Fig. 11 AFM images of the P1:$PC_{60}BM$/$PC_{70}BM$ and P4:$PC_{60}BM$/$PC_{70}BM$ cells.

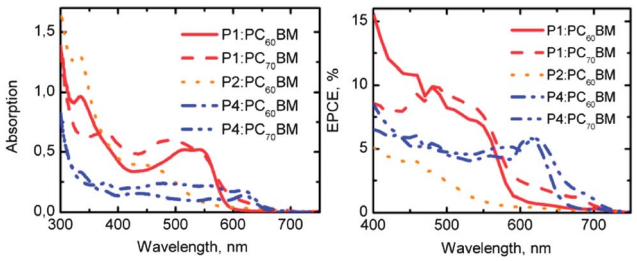

Fig. 12 Absorption and EPCE spectra of the P1:$PC_{60}BM$/$PC_{70}BM$ and P4:$PC_{60}BM$/$PC_{70}BM$ cells.

the cells with P4, which originates from the differences of the active layer thicknesses in the optimized cells (Table 1). However, the P4:$PC_{70}BM$ cell produced the highest η, although this cell has a remarkably lower absorption up to 600 nm than the cells with P1. This further validates better exciton diffusion and charge transport in P4 compared to P1. The absorbance of the P1:$PC_{70}BM$ cell is higher from 400 nm to 500 nm than that of the P1:$PC_{60}BM$ cell, but the EPCE of P1:$PC_{70}BM$ is lower in the same wavelength range. This is consistent with the assumption that the exciton transfer is better due to the smoother morphology of the P1:$PC_{60}BM$ cell.

The superiority of P3HT as a donor material compared to the copolymers tested here can be explained by structural differences, which influence both the exciton diffusion and hole transfer between adjacent polymer chains. The bulky side chains in P1–P4 decrease the π–π stacking between adjacent polymer chains and reduce the intermolecular interaction.[5,48] The photogenerated excitons are transported in the polymer phase of the BHJ blend only one-dimensionally along the backbones of the polymers,[49] and hopping between the chains is limited. Also, after exciton dissociation, holes are transferred only one-dimensionally along the polymer chains. Intermolecular exciton diffusion and hole transfer in the regioregular P3HT is possible due to H-aggregation in thin films.[42,50] The polymer self-organizes into two-dimensional π-stacked lamellar structures, which allow two-dimensional charge transport.[51]

Stability measurements

The efficiencies of the solar cells were measured again ~ six months after the cells were prepared to compare the stabilities of the cells of different donor–acceptor combinations with time. The photovoltaic parameters of the cells and the changes in the η and V_{OC} values compared to those measured on the following day after the cells were prepared are presented in Table 5 (for *I–V* curves, see ESI†). The largest increase in the efficiency, 37.7%, was measured for the P4:$PC_{70}BM$ cell after the storage of 6 months. The largest decrease in the efficiency, 42.9%, was measured for the P2:$PC_{60}BM$ cell. The V_{OC} values increased remarkably, 0.13 V, 0.13 V and 0.18 V, for the P1:$PC_{60}BM$, P2:$PC_{60}BM$ and P4:$PC_{70}BM$ cells, respectively, during the storage.

The serial resistances (R_s) and shunt resistances (R_{sh}) of the cells were calculated (see ESI, Table S2†) as explained in the literature.[52] Based on the changes in η values, the morphology of the cells is expected to change during the storage. Therefore, the resistances were calculated from both the *I–V* curves measured the following day after the cell preparation and the *I–V* curves of the aged cells. R_s is closely related to the intrinsic resistance and thickness of the semiconductor layer and it should be as small as possible. R_{sh} can be correlated with the charge recombination and leakage current in the cell and it should be as large as possible.

Table 5 Photovoltaic parameters of the solar cells composed of P3HT, P1, P2 and P4 as donors and $PC_{60}BM$ and $PC_{70}BM$ as acceptors measured 6 months after the preparation and the changes in the cell efficiency and voltage during the 6 month storage

Active layer	J_{sc} (mA cm^{-2})	V_{OC} (V)	FF (%)	η_{best} (%)	η_{avg} (%)	$\Delta\eta$ (%)	ΔV_{OC} (V)
P3HT:$PC_{60}BM$	−2.46	0.55	59	2.16	2.06	−29	+0.03
P1:$PC_{60}BM$	−1.31	0.56	40	0.80	0.70	−3.6	+0.08
P1:$PC_{70}BM$	−0.69	0.47	40	0.35	0.28	+30	+0.13
P2:$PC_{60}BM$	−0.31	0.56	25	0.12	0.09	−43	+0.13
P4:$PC_{60}BM$	−0.63	0.43	45	0.33	0.30	−42	−0.02
P4:$PC_{70}BM$	−1.01	0.59	62	1.03	0.93	+38	+0.18

Clearly the P4:$PC_{70}BM$ cell underwent the largest increase in R_{sh}, from 2759 Ω cm^2 to 7062 Ω cm^2, during the storage. This means that the amount of recombinations was decreased due to the improved morphology of the P4:$PC_{70}BM$ layer. Therefore a better fill factor was produced by the cell. In addition, the increase in the cell efficiency during the storage can be specifically assigned to the highly improved V_{OC} (+0.18 V). The changes in the active layer morphology cause changes also in the HOMO and LUMO levels of the donor and acceptor. The changes in the energy levels are dependent on the position of the donor polymers in relation to the acceptor molecules at the donor–acceptor interface, as shown before (Fig. 8). The largest changes in the HOMO and LUMO energies were observed in the computational model consisting of the P4 monomer and $PC_{70}BM$, which leads to a larger P4 monomer HOMO–$PC_{70}BM$ LUMO gap, *i.e.* higher V_{OC}, when $PC_{70}BM$ is close to either the electron rich or the electron deficient moiety of the P4 monomer. This suggests that during the 6 month storage the molecules in the active layer move in relation to each other to form a more ideal BHJ structure, which changes the energy levels of the donor polymer and acceptor molecules and improves the cell voltage remarkably.

Materials and methods used for studying the polymer structures and photovoltaic performance

The Gaussian 09 program package[53] was used to model isolated chains of the polymers presented in Fig. 1 or the corresponding oligomers. The B3LYP hybrid density functionals[54–57] combined with the 6-31G* basis set were used in the calculations. A periodic boundary condition (translation vector, T_v, in the input) was applied in one dimension in the case of polymer models. A default option was used for the number of *k*-points,

which resulted in 9, 6, 6, and 27 *k*-points due to the sizes of the P1, P2, P3, and P4 periodic models, respectively. As a test, optimization with only 11 *k*-points for the P4 model was done and the results were identical to the 27 *k*-point case. This means that the default *k*-point values are adequate for our models. The structures were optimized and frequency calculations were performed on the shortest oligomers ($n = 1$–2) to ensure that the optimized structures were at minima. Additionally, the first excitation in the UV-Vis spectra of the oligomeric chains ($n \leq 6$–8) was calculated using TD-DFT. Chemcraft[58] was used for visualization of the structures and molecular orbitals.

The solvents and Alq_3 (99.995%) were purchased from Sigma-Aldrich and used without further purification. The solar cell samples were prepared on ITO coated glass substrates (1.2 cm × 3.5 cm) purchased from Solems. Zinc–acetate ($Zn(O\text{-}COCH_3)_2 \cdot 2H_2O$) for ZnO layer preparation was purchased from Sigma-Aldrich. The reference polymer, P3HT, was purchased from Rieke Metals, and acceptors $PC_{60}BM$ (99.0%) and [6,6]-phenyl-C70-butyric acid methyl ester (99.0%, $PC_{70}BM$) from Nano-C. The P1–P3 polymers were synthesized at the Kekulé-Institut für Organische Chemie und Biochemie der Rheinischen Friedrich-Wilhelms-Universität Bonn following the Suzuki-polycondensation procedure[38] and P4 as described below.

The synthetic scheme of P4 is presented in Scheme 1. 4,7-Dibromo-2-(4-decyloxy-3,5-difluorophenyl)-2*H*-benzotriazole **1** (102 mg, 0.188 mmol), 2,6-bis(trimethyltin)-4,8-bis(2-ethylhexyloxy)benzo[1,2-*b*:3,4-*b*']dithiophene **2** (145 mg, 0.188 mmol) and $Pd(PPh_3)_4$ (12 mg, 10.4 μmol) were stirred for 68 h at 105 °C in a mixture of toluene (abs., 6 mL) and DMF (abs., 1.5 mL) under argon. The polymer was end capped by the addition of 2-(tributylstannyl)-thiophene (16 mg, 42.9 μmol) and additional stirring for 2 h. Then, 2-bromothiophene (100 mg, 0.613 mmol) was added and the mixture was stirred for another 4 h. After cooling to room temperature and filtration through celite, the polymer was precipitated by addition of the organic phase to MeOH. The polymer was extracted using a Soxhlet-apparatus with acetone for 3 h, *n*-hexane for 4 h and MTBE for 4 h. The polymer was redissolved in THF and precipitated from MeOH. The precipitate was collected by filtration and dried *in vacuo* at 70 °C to yield a blue solid (139 mg, 89%). ^{1}H NMR (500 MHz, 373 K, 1,2-dichlorobenzene-d4, δ, ppm, see ESI†): 9.19–7.39 (m, 1H), 5.13–3.23 (m, 2H), 2.31–0.88 (m, 14H). ^{19}F NMR (471 MHz, 373 K, 1,2-dichlorobenzene-d4, δ, ppm, see ESI†): −125 (br, 2F). GPC (THF, polystyrene): $M_n = 15\,200$ g mol^{-1}, PDI = 4.6.

The steady state absorption and fluorescence were measured employing a UV-3600 Shimadzu UV-VIS-NIR spectrophotometer and a Jobin Yvon-SPEX fluorolog. The fluorescence lifetimes were determined in $CHCl_3$ (99.0–99.4%) solution using a time correlated single photon counting (TCSPC) system equipped with a Picoharp 300 controller and a PDL 800-B driver for excitation and a microchannel plate photomultiplier (Hamamatsu R3809U-50) for detection in a 90° configuration. The excitation wavelength was 405 nm and the pulse frequency was 2.5 MHz. The experimental set-up of the measuring instrumentation was similar for all polymers.

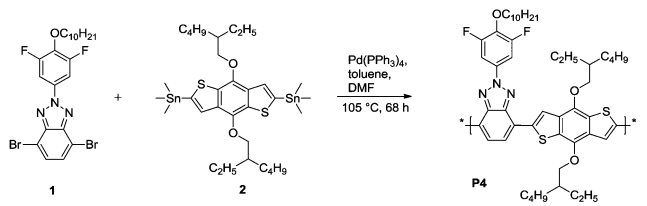

Scheme 1 Synthesis of P4.

External photon-to-current efficiency (EPCE) measurements of the solar cells were monitored using a voltage/current measuring instrument (E5272A, Agilent Technologies). The excitation light source was a Xe-arc lamp coupled with a monochromator for selecting the excitation wavelength. The excitation power density alternated between 0.12 mW cm^{-2} and 0.68 mW cm^{-2} depending on the wavelength of 400 to 800 nm where the background current from ITO is negligible.[59] Stepwise (light-on/off) currents produced by the excitations as a function of time were measured with 0 V. The EPCE spectra were calculated by averaging the measured currents.

To determine the active layer thickness of each polymer:PCBM blend, a narrow strip of the film was removed with a cotton stick dipped in $CHCl_3$ and the step was measured with a Veeco Wyko NT-1100 profilometer. The profilometry data were recorded from 230 × 300 μm^2 and analyzed in phase shift interferometry (PSI) mode. The vertical resolution of this method is close to 1 Å according to the instrument manual and the horizontal resolution of the objective (20× magnification) is 0.75 μm.

Solar cells were constructed on commercial ITO covered glass substrates. The ITO layer was taped and lacquered for *aqua regia* etching to achieve a patterned ITO. The etched plates were cleaned by sonicating in acetone, chloroform, SDS solution (20 mg sodium dodecyl sulphate in 500 mL Milli-Q H_2O), Milli-Q H_2O and 2-propanol 30 min in each, in this order, and dried in a vacuum at 150 °C for one hour. After a 10 min N_2 plasma cleaning procedure (Harrick Plasma Cleaner PDG-236), a 20 nm ZnO layer was deposited by 1 min spin-coating in a WS-400B-6NPP/LITE spin-coater from Laurell Technologies from 50 g L^{-1} zinc-acetate in 96% 2-methoxyethanol and 4% ethanolamine solution following the literature process.[37]

The photoactive layer compounds P1, P2, P3, P4 or P3HT and $PC_{60}BM$ or $PC_{70}BM$ were dissolved in 1,2-dichlorobenzene and stirred (250 rpm) overnight at 50 °C. The temperature was raised to 70 °C for 30 min prior to spin-coating of the BHJ photoactive layer from the polymer:PCBM blend for 5 minutes (600 rpm) in the spin-coater under N_2 flow. The spin-coated films were annealed in a vacuum at 110 °C for 10 min. The buffer layer and the Au anode were evaporated in the vacuum evaporator under ~3 × 10^{-6} mbar pressure. The evaporation rate and film thickness were controlled by evaporator crystals to deposit ~5 nm thick buffer and ~50 nm thick Au anode layers on top of the photoactive layer. The cells were stored in an ambient atmosphere in the dark before measurements and analysis.

The photovoltaic parameters were obtained and calculated from current–voltage (*I*–*V*) curves, which were measured in the dark and under simulated AM 1.5 sunlight illumination (50 mW cm^{-2}) using an Agilent E5272A source/monitoring unit.

A voltage of −0.20 V to 0.60 V was applied in 10 mV steps. The measurements were carried out in an ambient atmosphere at room temperature without encapsulation of the devices. The illumination was produced by a filtered Xe-lamp (Oriel Corporation & Lasertek) in the Zuzchem LZC-SSL solar simulator. The illumination power density was measured by using a Coherent Fieldmax II LM10 power meter. Because a certified measuring system could not be employed, the absolute efficiency values are not directly comparable with the other published results. However, the reported efficiencies and the relative efficiency changes are comparable within the presented devices.

The photoactive layer morphologies of the different donor-acceptor combinations in the solar cell samples were inspected with AFM at the Department of Molecular Engineering in Kyoto University. The measurements were carried out with an Asylum Technology MFP-3D-SA instrument in the AC mode.

Conclusions

We studied the internal relationship between the molecular structures of four donor–acceptor (D–A) copolymers (P1–P4) and their photovoltaic performances. Molecular geometries and the properties related to the electron structures of P1–P4 were studied by DFT using B3LYP. The copolymers were used as donor materials in inverted organic ITO|ZnO|donor:acceptor|Alq_3|Au solar cells. The DFT information on electron structure related properties was combined with the results of photovoltaic, electrochemical, spectroscopic, and thermoanalytical measurements.

The cell with P4 as a donor material performed better and was more stable than the cells with P1–P3. The optimizations of the CRUs resulted in a more planar structure for P4 than for P1–P3. Also, the computed frontier molecular orbitals show that the LUMOs of P2 and P3 are not continuous as the electron densities are concentrated on the benzotriazole moieties of the copolymers. Therefore, the better exciton transfer properties of P4 are due to a more planar molecular structure with a continuous LUMO electron density. Moreover, P4 has better charge transfer properties as HTM, which is consistent with the bigger N_{MCC} values computed for P4 and P1 than for P2 and P3.

Further calculations show that interaction between the donor and acceptor molecules affects their electronic structures, which changes the energy levels of both molecules. During the six month storage the molecules in the active layer move with respect to each other, which changes the energy levels. The biggest calculated energy level changes of the donor HOMO and the acceptor LUMO of the P4:$PC_{70}BM$ cell correlate with the increased V_{OC} of the cell. AFM studies on the active layers of the solar cells yielded insight into the morphology which allowed us to better analyze the differences between the solar cell performances of different donor:acceptor combinations.

These studies show that computational methods are a valuable tool for defining the molecular structure related properties of D–A copolymers and for predicting their performances as donor materials. The DFT calculations provided data, which supplement the experimental results. Therefore, even more research and clarification of the available computational methods are important for chemists in the evolving field of organic materials and photovoltaics.

Acknowledgements

Computing resources provided by the CSC – IT Center for Science Ltd, administrated by the Finnish Ministry of Education, and the National Doctoral Programme in Nanoscience (NGS-NANO) are gratefully acknowledged.

References

1 J. Hou, M.-H. Park, S. Zhang, Y. Yao, L.-M. Chen, J.-H. Li and Y. Yang, *Macromolecules*, 2008, **41**, 6012–6018.
2 J. Hou, H.-Y. Chen, S. Zhang, R. I. Chen, Y. Yang, Y. Wu and G. Li, *J. Am. Chem. Soc.*, 2009, **131**, 15586–15587.
3 Y. Zhang, S. K. Hau, H.-L. Yip, Y. Sun, O. Acton and A. K.-Y. Jen, *Chem. Mater.*, 2010, **22**(9), 2696–2698.
4 S. C. Price, A. C. Stuart and W. You, *Macromolecules*, 2010, **43**, 4609–4612.
5 Q. Shi, H. Fan, Y. Liu, J. Chen, L. Ma, W. Hu, Z. Shuai, Y. Li and X. Zhan, *Macromolecules*, 2011, **44**, 4230–4240.
6 L. Dou, J. Gao, E. Richards, J. You, C.-C. Chen, K. C. Cha, Y. He, G. Li and Y. Yang, *J. Am. Chem. Soc.*, 2012, **134**, 10071–10079.
7 B. Aïch, J. Lu, S. Beaupré, M. Leclerc and Y. Tao, *Org. Electron.*, 2012, **13**, 1736–1741.
8 H. Wettack, F. Pasker and S. Höger, *Macromolecules*, 2008, **41**, 9513–9515.
9 L. Zhang, C. He, J. Chen, P. Yuan, L. Huang, C. Zhang, W. Cai, Z. Liu and Y. Cao, *Macromolecules*, 2010, **43**, 9771–9778.
10 B. Peng, A. Najari, B. Liu, P. Berrouard, D. Gendron, Y. He, K. Zhou, M. Leclerc and Y. Zou, *Macromol. Chem. Phys.*, 2010, **211**, 2026–2033.
11 J. Min, Z.-G. Zhang, S. Zhang, M. Zhang, J. Zhang and Y. Li, *Macromolecules*, 2011, **44**, 7632–7638.
12 S. C. Price, A. C. Stuart, L. Yang, H. Zhou and W. You, *J. Am. Chem. Soc.*, 2011, **133**, 4625–4631.
13 Z. Zhang, B. Peng, B. Liu, C. Pan, Y. Li, Y. He, K. Zhou and Y. Zou, *Polym. Chem.*, 2010, **1**, 1441–1447.
14 J. Roncali, *Macromol. Rapid Commun.*, 2007, **28**, 1761–1775.
15 G. R. Hutchison, Y.-J. Zhao, B. Delley, A. J. Freeman, M. A. Ratner and T. J. Marks, *Phys. Rev. B: Condens. Matter Mater. Phys.*, 2003, **68**, 035204.
16 S. Xiao, A. C. Stuart, S. Liu, H. Zhou and W. You, *Adv. Funct. Mater.*, 2010, **20**, 635–643.
17 Z. El Malki, S. M. Bouzzine, L. Bejjit, M. Haddad, M. Hamidi and M. Bouachrine, *J. Appl. Polym. Sci.*, 2011, **122**, 3351–3360.
18 S. Habuchi, H. Fujita, T. Michinobu and M. Vacha, *J. Phys. Chem. B*, 2011, **115**, 14404–14415.
19 Y. Wang, Q. Peng, Q. Hou, K. Zhao, Y. Liang and B. Li, *Theor. Chem. Acc.*, 2011, **129**, 257–270.
20 V. Lukeš, P. Rapta, K. R. Idzik, R. Beckert and L. Dunsch, *J. Phys. Chem. B*, 2011, **115**, 3344–3353.

21 Q. Li, C. Zhong, J. Huang, Z. Huang, Z. Pei, J. Liu, J. Qin and Z. Li, *J. Phys. Chem. B*, 2011, **115**, 8679–8685.

22 C. Risko, M. D. McGehee and J.-L. Brédas, *Chem. Sci.*, 2011, **2**, 1200–1218.

23 P. M. Beaujuge, S. V. Vasilyeva, D. Y. Liu, S. Ellinger, T. D. McCarley and J. R. Reynolds, *Chem. Mater.*, 2012, **24**, 255–268.

24 H. Toufik, S. M. Bouzzine, F. Lamchouri, M. Nawdali, M. Hamidi and M. Bouachrine, *J. Mater. Environ. Sci.*, 2012, **3**, 286–293.

25 G. L. Gibson, T. M. McCormick and D. S. Seferos, *J. Am. Chem. Soc.*, 2012, **134**, 539–547.

26 Z. Lin, J. Bjorgaard, A. G. Yavuz, A. Iyer and M. E. Köse, *RSC Adv.*, 2012, **2**, 642–651.

27 A. Abbotto, M. Seri, M. S. Dangate, F. De Angelis, N. Manfredi, E. Mosconi, M. Bolognesi, R. Ruffo, M. M. Salamone and M. Muccini, *J. Polym. Sci., Part A: Polym. Chem.*, 2012, **50**, 2829–2840.

28 L. Ling and J. B. Lagowski, *J. Mol. Struct.: THEOCHEM*, 2010, **944**, 146–155.

29 B. G. Janesko, *J. Chem. Phys.*, 2011, **134**, 184105.

30 J. M. Granadino-Roldán, A. Garzón, G. García, M. Moral, A. Navarro, M. P. Fernández-Liencres, T. Peña-Ruiz and M. Fernández-Gómez, *J. Phys. Chem. C*, 2011, **115**, 2865–2873.

31 Y. Li and I. Dabo, *Phys. Rev. B: Condens. Matter Mater. Phys.*, 2011, **84**, 155127.

32 A. Ferretti, G. Mallia, L. Martin-Samos, G. Bussi, A. Ruini, B. Montanari and N. M. Harrison, *Phys. Rev. B: Condens. Matter Mater. Phys.*, 2012, **85**, 235105.

33 L. Deng, W. Shen, X. Xie, L. Jiang, B. Liu and M. Li, *Struct. Chem.*, 2012, **23**, 97–106.

34 S. S. Zade and M. Bendikov, *Org. Lett.*, 2006, **8**, 5243–5246.

35 J. Gierschner, J. Cornil and H.-J. Egelhaaf, *Adv. Mater.*, 2007, **19**, 173–191.

36 S. S. Zade, N. Zamoshchik and M. Bendikov, *Acc. Chem. Res.*, 2011, **44**, 14–24.

37 M. S. White, D. C. Olson, S. E. Shaheen, N. Kopidakis and D. S. Ginley, *Appl. Phys. Lett.*, 2006, **89**, 143517.

38 F. M. Pasker, M. F. G. Klein, M. Sanyal, E. Barrena, U. Lemmer, A. Colsmann and S. Höger, *J. Polym. Sci., Part A: Polym. Chem.*, 2011, **49**, 5001–5011.

39 (*a*) HOMO and LUMO levels of P1, P2 and P3, see: ref. 38; (*b*) HOMO and LUMO levels of P3HT and $PC_{60}BM$, see: A. K. K. Kyaw, X. W. Sun, C. Y. Jiang, G. Q. Lo and D. W. Zhao, *Appl. Phys. Lett.*, 2008, **93**, 221107; (*c*) HOMO and LUMO levels of $PC_{70}BM$, see: E. L. Ratcliff, J. Meyer, K. X. Steirer, N. R. Armstrong, D. Olson and A. Kahn, *Org. Electron.*, 2012, **13**, 744–749; (*d*) Conduction band of ZnO, see: ref. 37; (*e*) HOMO and LUMO levels of Alq_3, see: A. Tolkki, K. Kaunisto, J. P. Heiskanen, W. A. E. Omar, K. Huttunen, S. Lehtimäki, O. E. O. Hormi and H. Lemmetyinen, *Thin Solid Films*, 2012, **520**, 4475–4481.

40 M. T. Dang, L. Hirsch and G. Wantz, *Adv. Mater.*, 2011, **23**, 3597–3602.

41 F. Zhang, Z. Zhuo, J. Zhang, X. Wang, X. Xu, Z. Wang, Y. Xin, J. Wang, J. Wang, W. Tang, Z. Xu and Y. Wang, *Sol. Energy Mater. Sol. Cells*, 2012, **97**, 71–77.

42 G. Hukic-Markosian, T. Basel, S. Singh, Z. Valy Vardeny, S. Li and D. Laird, *Appl. Phys. Lett.*, 2012, **100**, 213903.

43 V. Manninen, W. Omar, J. Heiskanen, H. Lemmetyinen and O. Hormi, *J. Mater. Chem.*, 2012, **22**(43), 22971–22982.

44 S. Dey, P. Vivo, A. Efimov and H. Lemmetyinen, *J. Mater. Chem.*, 2011, **21**, 15587–15592.

45 I. G. Hill, A. Kahn, Z. G. Soos and R. A. Pascal, Jr, *Chem. Phys. Lett.*, 2000, **327**, 181–188.

46 M. Knupfer, *Appl. Phys. A: Mater. Sci. Process.*, 2003, **77**, 623–626.

47 P. Boland, S. S. Sunkavalli, S. Chennuri, K. Foe, T. Abdel-Fattah and G. Namkoong, *Thin Solid Films*, 2010, **518**, 1728–1731.

48 Y. Huang, X. Guo, F. Liu, L. Huo, Y. Chen, T. Russel, C. Han, Y. Li and J. Hou, *Adv. Mater.*, 2012, **24**, 3383–3389.

49 L. Yang, H. Zhou and W. You, *J. Phys. Chem. C*, 2010, **114**, 16793–16800.

50 Y. Yamagata and F. C. Spano, *J. Chem. Phys.*, 2012, **136**, 184901.

51 J. Clark, C. Silva, R. Friend and F. Spano, *Phys. Rev. Lett.*, 2007, **98**, 206406.

52 M.-S. Kim, B.-G. Kim and J. Kim, *ACS Appl. Mater. Interfaces*, 2009, **1**(6), 1264–1269.

53 M. J. Frisch, G. W. Trucks, H. B. Schlegel, G. E. Scuseria, M. A. Robb, J. R. Cheeseman, G. Scalmani, V. Barone, B. Mennucci, G. A. Petersson, H. Nakatsuji, M. Caricato, X. Li, H. P. Hratchian, A. F. Izmaylov, J. Bloino, G. Zheng, J. L. Sonnenberg, M. Hada, M. Ehara, K. Toyota, R. Fukuda, J. Hasegawa, M. Ishida, T. Nakajima, Y. Honda, O. Kitao, H. Nakai, T. Vreven, J. A. Montgomery, Jr, J. E. Peralta, F. Ogliaro, M. Bearpark, J. J. Heyd, E. Brothers, K. N. Kudin, V. N. Staroverov, T. Keith, R. Kobayashi, J. Normand, K. Raghavachari, A. Rendell, J. C. Burant, S. S. Iyengar, J. Tomasi, M. Cossi, N. Rega, J. M. Millam, M. Klene, J. E. Knox, J. B. Cross, V. Bakken, C. Adamo, J. Jaramillo, R. Gomperts, R. E. Stratmann, O. Yazyev, A. J. Austin, R. Cammi, C. Pomelli, J. W. Ochterski, R. L. Martin, K. Morokuma, V. G. Zakrzewski, G. A. Voth, P. Salvador, J. J. Dannenberg, S. Dapprich, A. D. Daniels, O. Farkas, J. B. Foresman, J. V. Ortiz, J. Cioslowski and D. J. Fox, *Gaussian 09, Revision C.01*, Gaussian, Inc., Wallingford CT, 2010.

54 A. D. Becke, *J. Chem. Phys.*, 1998, **98**, 5648–5652.

55 C. Lee, W. Yang and R. G. Parr, *Phys. Rev. B: Condens. Matter Mater. Phys.*, 1988, **37**, 785–789.

56 S. H. Vosko, L. Wilk and M. Nusair, *Can. J. Phys.*, 1980, **58**, 1200–1211.

57 P. J. Stephens, F. J. Devlin, C. F. Chabalowski and M. J. Frisch, *J. Phys. Chem.*, 1994, **98**, 11623–11627.

58 G. A. Zhurko, Chemcraft Version 1.60, http://www.chemcraftprog.com.

59 S. Yang, L. Fan and S. Yang, *J. Phys. Chem. B*, 2004, **108**, 4394–4404.

Publication III

Spectroscopic study of a synthesized Alq_3 end-capped oligothiophene applied in organic solar cells

Venla M. Manninen, Juha P. Heiskanen, Kimmo M. Kaunisto, Osmo E. O. Hormi and Helge J. Lemmetyinen

RSC Adv., **2014**, *4*, 8846 – 8855.

RSC Advances

PAPER

Spectroscopic study of a synthesized Alq_3 end-capped oligothiophene applied in organic solar cells†

Cite this: *RSC Adv.*, 2014, **4**, 8846

Venla M. Manninen,*[a] Juha P. Heiskanen,[b] Kimmo M. Kaunisto,[a] Osmo E. O. Hormi[b] and Helge J. Lemmetyinen[a]

Received 6th December 2013
Accepted 13th January 2014

DOI: 10.1039/c3ra47367h

www.rsc.org/advances

In this paper, we report the spectroscopic properties of a synthetically tailored Alq_3 end-capped oligothiophene ($(Alq_3)_2$-OT) studied by steady state and time resolved spectroscopic methods in chloroform and solid films. In chloroform a photo-induced intramolecular electron transfer from the oligothiophene backbone to the Alq_3 moiety was observed. When $(Alq_3)_2$-OT was mixed with a fullerene derivative (PCBM) in chloroform, we demonstrate that $(Alq_3)_2$-OT donates an electron to PCBM. With that in mind, $(Alq_3)_2$-OT was applied as a dopant molecule to improve the efficiency of P3HT:PCBM bulk hetero junction (BHJ) solar cells.

Introduction

Growing interest in organic electronics, such as organic solar cells (OSCs) and organic light emitting diodes (OLEDs), has increased the need to synthesize new organic materials that can be applied in producing low-cost and light weight devices. Detailed understanding of molecular properties and inter- or intramolecular interactions is a prerequisite for developing new photoactive and functional materials. In recent years, solution-processable small molecule donor materials have gained increasing amounts of attention in solar cell research. Small molecule materials have several advantages over polymers including well-defined structures and easier purification.

A large number of small-molecule compounds used in organic electronic devices utilize thiophene units as components of their chemical structure. Thiophene containing compounds have been used as photoactive donor molecules and hole transporting materials in OSCs that show good photovoltaic performance.[1] Thiophene also plays an important role in many organic dyes used in dye-sensitized solar cells by acting as a π-conjugation bridge.[2]

Tris-(8-hydroxyquinoline)aluminum (Alq_3) complex has widely been used as light-emitting and electron transporting material in OLEDs, since its electroluminescence properties were discovered by Tang and VanSlyke.[3] After that, the electron mobility of Alq_3 has been extensively studied[4] and it has been used as an electron transporting buffer layer in conventional organic solar cells to increase the stability and lifetime of the cells.[5]

Recently, various Alq_3 derivatives with tailored energy levels exhibited up to a 30% increase in the efficiency of the inverted cell compared to those with the parent Alq_3 as a hole-transporting anode buffer layer.[6] Furthermore, Alq_3 and its derivatives have been used as dopants in the photoactive layer of OSCs, which increased the efficiency of the cells remarkably.[6a]

In this paper, we present the synthesis of Alq_3 end-capped oligothiophene ($(Alq_3)_2$-OT) and extensively study its spectroscopic properties. Fluorescence properties of $(Alq_3)_2$-OT differ drastically from those of the parent Alq_3 complex and the thiophene oligomer. We concentrate on understanding the properties of the synthesized molecule by steady state and time-resolved spectroscopic methods. The spectroscopic measurements strongly support an intramolecular electron transfer from the oligothiophene backbone to the Alq_3 complex.

Interaction of $(Alq_3)_2$-OT with PCBM was also studied. Based on those results, we propose that $(Alq_3)_2$-OT can donate an electron to PCBM. With that in mind, $(Alq_3)_2$-OT was tested as a dopant molecule in the P3HT:PCBM bulk hetero junction (BHJ) layer for improving cell efficiency. Previous reports have suggested that the cell efficiency was increased due to improved morphology, crystallization, and charge transport caused by doping with Alq_3 molecules.[6a] Here we propose that $(Alq_3)_2$-OT can function in the BHJ active layer as an additional light-absorber and donate electrons to PCBM, thereby improving the cell efficiency.

[a]*Department of Chemistry and Bioengineering, Tampere University of Technology, P.O. Box 541, FI-33101, Tampere, Finland. E-mail: venla.manninen@tut.fi*

[b]*Department of Chemistry, University of Oulu, P.O. Box 3000, FI-90014, Finland*

† Electronic supplementary information (ESI) available: ^{1}H NMR spectra of compounds **2–4**, ^{1}H and ^{13}C NMR spectra of compounds **5** and **6**, ^{1}H NMR spectrum of $(Alq_3)_2$-OT, quenching of compound **5**, Alq_3 and $(Alq_3)_2$-OT in the presence of PCBM, TCSPC decay curves of $(Alq_3)_2$-OT and PCBM film samples and DAS spectra of $(Alq_3)_2$-OT and PCBM in $CHCl_3$, table of the solar cell results with compound **5**, absorption and emission spectra of the evaporated films of $(Alq_3)_2$-OT, DSC curve of $(Alq_3)_2$-OT, transient absorption and decay component spectra of $(Alq_3)_2$-OT mixed with PCBM, DPV curves of $(Alq_3)_2$-OT and compound **5**. See DOI: 10.1039/c3ra47367h

The hole transporting properties of $(Alq_3)_2$-OT were also tested by using it as a buffer layer in inverted OSCs. The improved cell efficiencies and stabilities measured several weeks after the cell preparation demonstrate that the compatibility of the parent Alq_3 with BHJ materials and its charge transporting properties can be improved by combining the complexes with the oligothiophene structure.

Results and discussion

Synthesis of $(Alq_3)_2$-OT

Commercially available starting material, compound **1**, was brominated with *N*-bromosuccinimide (NBS) to afford 5,5‴-dibromo-3,3‴-dihexyl-2,2′:5′,2″:5″,2‴-quaterthiophene (**2**) (Scheme 1). Compound **2** has been previously prepared by time intensive methods with various yields (50–92%).[7] Our method applies the recent observation that thiophenes can be brominated neatly with NBS by using ultrasound irradiation and a suitable solvent.[8] After 1 h of reaction time and chromatographic purification, compound **2** could be collected in high yield (91%). Ultrasound has previously been utilized together with NBS in bromination reactions of phenyl and naphthalene backbones.[9] In the best case, ultrasound irradiation offers a way to produce the desired bromination product efficiently: fast and facilely with a high yield and selectivity in mild conditions.

The literature provides one preparation method to produce 3,3⁗,3⁗′,4′-tetrahexyl-2,2′:5′,2″:5″,2‴:5‴,2⁗:5⁗,2⁗′:5⁗′,2⁗′′-sexithiophene (**3**).[7c] Nickel catalyzed coupling with Grignard reagent produced compound **3** in low yield (31%). In our hands, compound **3** was prepared and isolated in high yield (97%) by applying Suzuki–Miayura cross-coupling approach.

Ultrasound assisted bromination could be also used to synthesize 5,5⁗′-dibromo-3,3⁗,3⁗′,4′-tetrahexyl-2,2′:5′,2″:5″,2‴:5‴,2⁗:5⁗,2⁗′:5⁗′,2⁗′′-sexithiophene (**4**). Compound **4** was

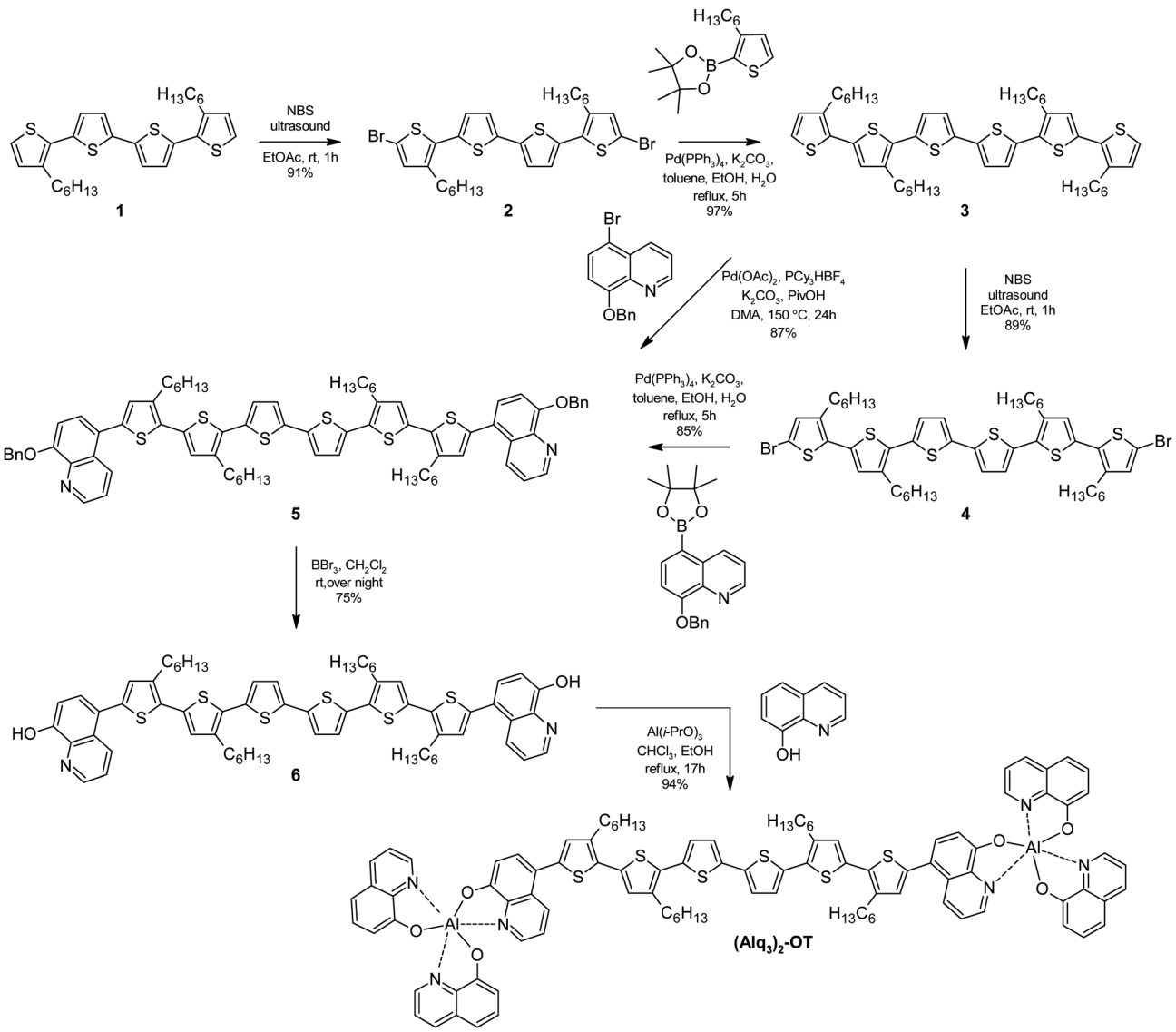

Scheme 1 Synthetic scheme of $(Alq_3)_2$-OT.

isolated in good yield (89%). The traditional method has previously given compound **4** in lower yield (77%).[7c]

Compound **5**,5,5′-(3,3‴,3⁗,4′-tetrahexyl-2,2′:5′,2″:5″,2‴:5‴,2⁗:5⁗,2⁗⁗:5⁗⁗,2⁗⁗⁗-sexithiene-5,5⁗⁗⁗-diyl)bis[8-(benzyloxy)quinoline], can be synthesized by using two different methods. A traditional cross-coupling method, like Suzuki–Miayura used here, needs halogenated starting material (compound **4**) and a boronic acid derivative, (8-(benzyloxy)-5-(4,4,5,5-tetramethyl-1,3,2-dioxaborolan-2-yl)quinolone), to undergo coupling. The Suzuki–Miayura reaction gave compound **5** in good yield (85%). An alternative way to prepare compound **5** is to use the direct arylation method. Palladium catalyzed direct arylation of thiophenes has recently shown potential as an efficient coupling reaction.[10] Indeed, the direct arylation method was shown to be a more convenient approach to produce compound **5**. Compound **3** underwent direct arylation smoothly with 8-(benzyloxy)-5-bromoquinoline to afford compound **5** in good yield (87%). In this way, two additional reaction steps of Suzuki–Miyaura reaction, bromination of compound **3** and borylation of 8-(benzyloxy)-5-bromoquinoline, can be avoided and the desired product **5** can be isolated using a simple filtration and washing procedure.

Removal of the benzyl protecting group was done with BBr_3 to afford 5,5′-(3,3‴,3⁗,4′-tetrahexyl-2,2′:5′,2″:5″,2‴:5‴,2⁗:5⁗,2⁗⁗:5⁗⁗,2⁗⁗⁗-sexithiene-5,5⁗⁗⁗-diyl)diquinolin-8-ol (**6**) in good yield (75%). Complexation of compound **6** and fixed amount of 8-hydroxyquinoline ligands (4 equiv.) with Al^{3+} was performed by using Al(*i*-PrO)$_3$ (2 equiv.) as an aluminum source. Finally, the target compound $(Alq_3)_2$-OT was isolated in high yield (94%).

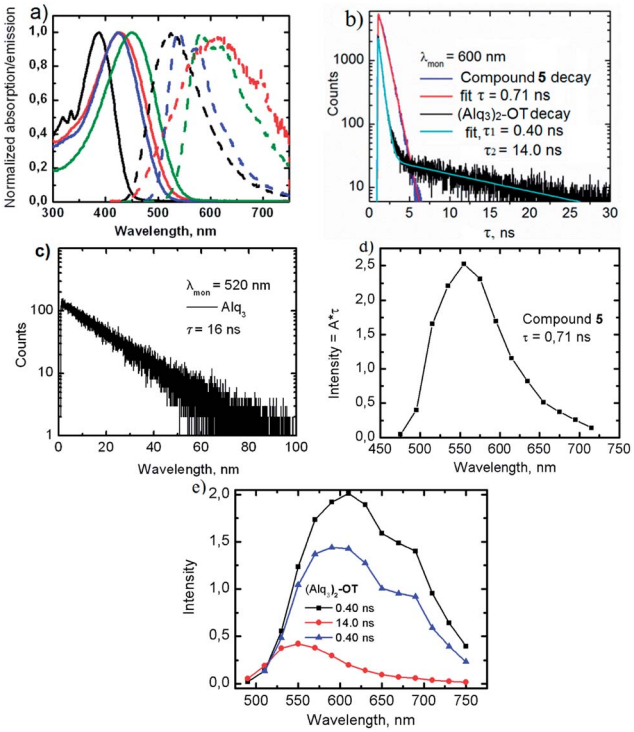

Fig. 1 (a) Normalized absorption (solid lines) and emission (dashed lines) spectra of compound **5** (blue), $(Alq_3)_2$-OT (red), Alq_3 (black) and P3HT (green). (b) Fluorescence decay curves of compound **5** and $(Alq_3)_2$-OT (λ_{ex} = 405 nm). (c) Fluorescence decay curve of Alq_3 (λ_{ex} = 405 nm). (d) Fluorescence DAS of compound **5** (λ_{ex} = 405 nm). (e) Fluorescence DAS of $(Alq_3)_2$-OT, (λ_{ex} = 405 nm: black and red curves, λ_{ex} = 483 nm: blue curve). All measured in $CHCl_3$.

Spectroscopic and electrochemical analysis

Steady state and time-resolved absorption and fluorescence emission measurements were carried out in order to compare the properties of the $(Alq_3)_2$-OT, Alq_3, and the oligothiophene compound (**5**). Compound **5** and $(Alq_3)_2$-OT were studied in 0.22 mM $CHCl_3$ solutions, while Alq_3 in 0.44 mM $CHCl_3$ solution. These concentrations were used to allow easier comparison between the free Alq_3 complex and $(Alq_3)_2$-OT, where two complexes are bound to one oligothiophene backbone. Results of the spectroscopic measurements are collected in Table 1.

Normalized steady state absorption and fluorescence emission spectra of compound **5**, $(Alq_3)_2$-OT, P3HT, and Alq_3 are presented in Fig. 1a. The absorption of the $(Alq_3)_2$-OT is slightly red-shifted compared to that of compound **5**. The fluorescence properties of the compounds differ significantly. The emission band of the $(Alq_3)_2$-OT is remarkably broadened, red-shifted and significantly lower in intensity compared to that of compound **5**. Time correlated single photon counting (TCSPC) measurements showed that the decays of compound **5** and Alq_3 are clearly monoexponential, but $(Alq_3)_2$-OT has a biexponential decay (Fig. 1b and c). The decay associated spectra (DAS) show that compound **5** has one component with a lifetime of 0.71 ns and the $(Alq_3)_2$-OT has two components with lifetimes of 0.40 ns and 14.0 ns (Fig. 1d and e). Obviously, the longer lived component corresponds to the lifetime of Alq_3 moiety and the shorter one to the oligothiophene backbone of the $(Alq_3)_2$-OT.

The fluorescence intensity of $(Alq_3)_2$-OT is significantly lower compared to those of the free Alq_3 and compound **5** (Table 1). The reason for the decreased fluorescence is most likely an intramolecular charge transfer from the oligothiophene backbone to the Alq_3 moieties. To better understand the possible charge transfer in the molecule, the energy levels of the compounds shown in Fig. 2 were measured by differential pulse voltammetry (DPV curves: see ESI, Fig. S6†). The LUMO level of $(Alq_3)_2$-OT corresponds to that of Alq_3 and the HOMO level of $(Alq_3)_2$-OT is the same as that of compound **5**. This demonstrates that the redox properties of $(Alq_3)_2$-OT originate from its components Alq_3 and compound **5**. The LUMO energy level of the compound **5** (−2.2 eV) is higher than that of Alq_3 (−2.4 eV).

Table 1 Summary of the spectroscopic properties of compound **5**, $(Alq_3)_2$-OT and Alq_3. $A_{405\ nm}$ and I_{PL} refer to absorbance at 405 nm and fluorescence intensity maxima, respectively

Compound (conc. mM)	$\lambda_{abs,max}$ (nm)	$\lambda_{PL,max}$ (nm)	$A_{405\ nm}$	$I_{PL,max}$ (pure)	$I_{PL,max}$ (mixture)
5 (0.22)	423	545	1.46	4.9×10^7	3.4×10^7
$(Alq_3)_2$-OT (0.22)	427	604	0.98	2.7×10^6	1.7×10^6
Alq_3 (0.44)	388	528	0.42	1.9×10^7	6.1×10^6

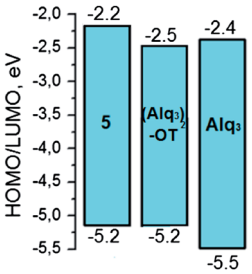

Fig. 2 HOMO and LUMO energy levels of compound **5**, $(Alq_3)_2$-OT and Alq_3.[6a]

Therefore, it is reasonable that the intramolecular electron transfer in $(Alq_3)_2$-OT from the excited oligothiophene backbone to the charge transfer state (CTS) of the end-capped Alq_3 complexes occurs and it is a competing process with oligothiophene fluorescence relaxation. In addition, the maximum of $(Alq_3)_2$-OT excitation spectra blue shifts compared to its absorption maxima (see ESI, Fig. S5†) due to the intramolecular electron transfer.

For TCSPC measurements of $(Alq_3)_2$-OT, the excitation wavelength of 483 nm was used to solely excite the oligothiophene backbone of $(Alq_3)_2$-OT. As shown in Fig. 1e, excitation at 483 nm results in only one component, similar to the short living component in the 405 nm excitation. Energy transfer from the oligothiophene backbone to the Alq_3 moieties can be excluded, because the 14 ns component does not exist when exciting at 483 nm.

The behaviour of the molecules in the presence of a quencher molecule, PCBM, was investigated in additional steady state measurements. The compounds were measured without PCBM and then immediately after with PCBM. Therefore, the intensities of the absorption and emission spectra are comparable. Absorption and emission spectra of compound **5**, $(Alq_3)_2$-OT and Alq_3 in the presence and absence of PCBM in $CHCl_3$ are shown in Fig. 3a and b.

As the lifetimes of the oligothiophene backbones are 0.7 and 0.4 ns for compound **5** and $(Alq_3)_2$-OT, respectively, and the concentration of PCBM is as low as 0.84 mM, the 40–60% decrease in the fluorescence intensities (Fig. 3b) would not be possible by diffusion. Thus the observed quenching is due to static quenching (see also ESI, p. 17†).

The films prepared from $(Alq_3)_2$-OT, PCBM and mixtures of the three different mass ratios, (Fig. 3c) were studied using steady state emission (Fig. 3d) and TCSPC methods. The emission of $(Alq_3)_2$-OT is quenched (Fig. 3d) as a function of PCBM content in the solid films. The emission intensity also decreases in TCSPC measurements when the PCBM content is increased and same photon collection time is used (see ESI, Fig. S1†).

Because PCBM efficiently quenches the emission of $(Alq_3)_2$-OT, it seems that $(Alq_3)_2$-OT is able to donate an electron to PCBM. Therefore, to further study the intra- and intermolecular electron transfer, time resolved absorptions of $(Alq_3)_2$-OT in the presence and absence of PCBM were measured with a pump-probe set-up in chloroform. The transient absorption and decay component spectra are shown in Fig. 4. The measurements were

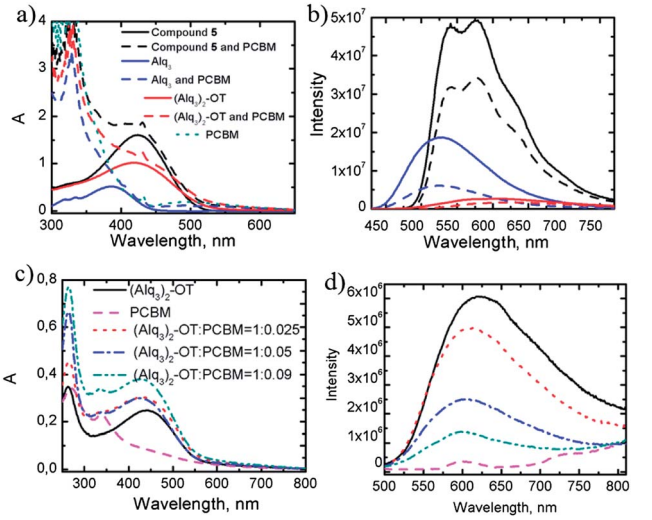

Fig. 3 (a) Absorption and (b) emission spectra (λ_{ex} = 405 nm) of the compound **5** (0.22 mM), $(Alq_3)_2$-OT (0.22 mM), and Alq_3 (0.44 mM) in the absence (solid lines) and presence of PCBM (0.84 mM) (dashed lines) in $CHCl_3$. (c) Absorption and (d) emission (λ_{ex} = 405 nm) spectra of $(Alq_3)_2$-OT, PCBM and their mixtures of three different mass ratios in films.

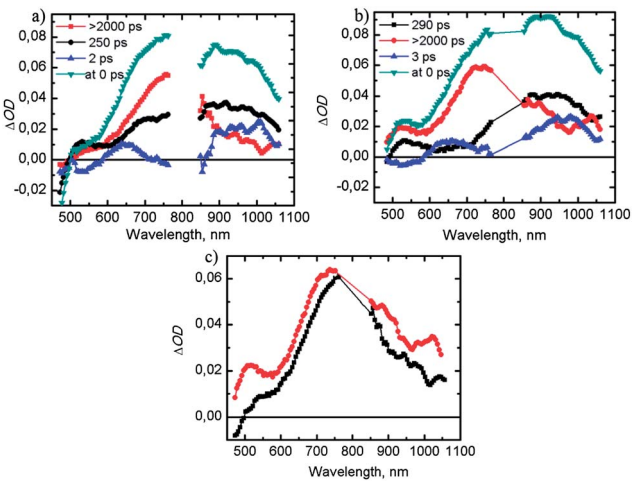

Fig. 4 Decay component spectra and calculated transient spectrum at 0 ps delay time of $(Alq_3)_2$-OT (0.22 mM) (a) in the absence and (b) in the presence of PCBM. (c) Calculated transient absorption spectra of $(Alq_3)_2$-OT (0.22 mM) in the absence (black squares) and presence (red circles) of PCBM (0.84 mM) after 300 ps of the excitation (λ_{ex} = 390 nm).

carried out until a 2000 ps delay. Therefore the components with lifetimes longer than that are extrapolations and given as τ > 2000 ps, the upper limit of the time-resolution of the instrument.

Fig. 4a, which presents the decay component spectra (blue, black, and red curves) and the transient absorption spectrum at delay time 0 ps (green curve) for $(Alq_3)_2$-OT, describes together with Fig. 5a the processes following the photoexcitation. With the 390 nm excitation, both the oligothiophene backbone and Alq_3 moieties are excited. The first component (blue triangles),

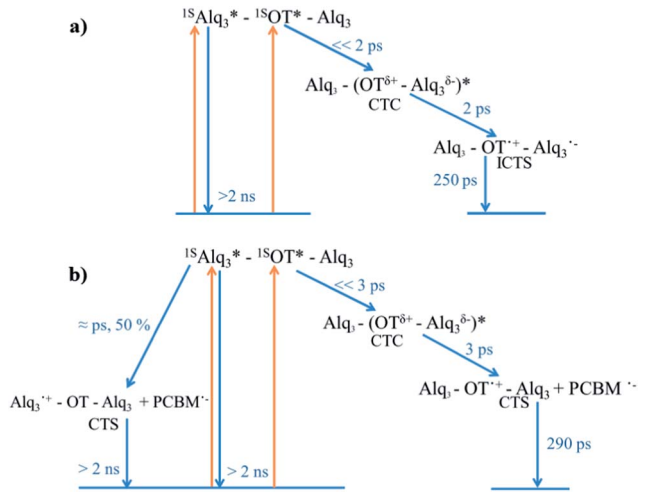

Fig. 5 Reaction scheme of the phenomena in $(Alq_3)_2$-OT (blue arrows) after photoexcitation (yellow arrows) (a) in the absence and (b) in the presence of PCBM.

is formed very fast (≪2 ps) indicated by negative bands at the wavelength areas, where hexathiophene cation radical, around 800 nm,[11] and Alq_3 anion radical, around 550 nm,[12] have their absorptions. We describe this state as excited charge transfer complex (CTC), covering the positive bands from 600 to 1050 nm. CTC decays in 2 ps to an intramolecular charge transfer state (ICTS, black circles). The broad absorption of ICTS, 600–1000 nm, consists of the broadened and red shifted intramolecular absorptions of the Alq_3 anion (550 nm and longer) and hexathiophene cation radicals (800 nm and longer). The charge transfer state recombines to the ground states with lifetime of 250 ps. The third component with τ > 2000 ps (red squares) is associated to the broad and long-lived ($\tau = 14$ ns by TCSPC) singlet excited state of the Alq_3 moiety.[13]

Mixing $(Alq_3)_2$-OT with PCBM causes changes both in the decay component spectra (Fig. 4b and 5b) and in the time-resolved absorption spectra (Fig. 4c and S4†). The first component, 3 ps (blue triangles), corresponds the CTC state similar as in Fig. 4a, in the absence of PCBM. The essential changes are observed in the second component, 290 ps (black squares), in which the short wavelength (600 nm–750 nm) component of the absorption, corresponding to the Alq_3 anion radical band in Fig. 4a, is absent. Evidently, PCBM has captured the electron from the formed ICTS and only the absorption of the hexathiophene cation radical is left. Its lifetime is increased, because the recombination with the counter anion radical is delayed. Instead it recombines with the PCBM radical anion in time of about 290 ps.

There are, however, PCBM anion radicals present after 300 ps (Fig. 4b and c) and 1000 ps (Fig. S4†) after excitation, as indicated by the absorption bands at 1050 nm.[11] Thus there is another way for its formation. As can be seen from Fig. 3b and Table 1, the fluorescence of Alq_3 moiety in $(Alq_3)_2$-OT was quenched about 40% in the presence of PCBM. Thus an alternative path for formation of PCBM radical anion is the electron transfer from Alq_3 singlet excited state to PCBM. This can also be seen as Alq_3 cation radical band at 550 nm (ref. 12) in Fig. 4b and c, as well as in Fig. S4.† The most probable reactions paths in the presence of PCBM are presented in Fig. 5b.

Photovoltaic performance

Compound **5**, $(Alq_3)_2$-OT and Alq_3 were applied as dopants in the photoactive BHJ layer of inverted ITO|ZnO|P3HT:PCBM|Alq_3|Au organic solar cells. The schematic structure of the cell and the chemical structures of the donor molecule P3HT, acceptor molecule PCBM, and buffer layer material Alq_3 are presented in Fig. 6. The use of compound **5** as the dopant molecule decreased the cell efficiency when compared to the undoped reference cell (see ESI, Table S1†). Instead, the best cell doped with $(Alq_3)_2$-OT had an efficiency of 2.63%, which is higher than that of the reference cell (Table 2). After a four week storage period, efficiencies of all doped devices were better than that of the reference cell. Moreover, the efficiency of the best cell doped with $(Alq_3)_2$-OT had increased to 2.85%, which demonstrates high stability of cells doped with $(Alq_3)_2$-OT.

The effect of doping with large concentrations of free Alq_3 complex and the equivalent amount of Alq_3 bound to the

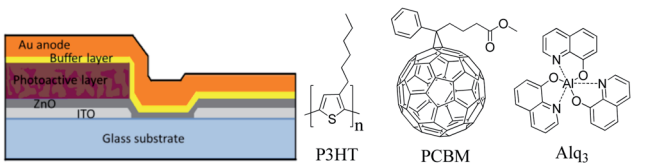

Fig. 6 Structure of the inverted solar cell and chemical structures of P3HT donor, PCBM acceptor and Alq_3 buffer layer material.

Table 2 Photovoltaic parameters of the cells doped with $(Alq_3)_2$-OT

$c((Alq_3)_2$-OT)[a] (mM)	Storage time	$J_{sc,best}$ (mA cm^{-2})	$V_{oc,best}$ (V)	FF_{best} (%)	η_{best} (%)	η_{avg} (%)
0	1 day	−2.86	0.50	59	2.33	2.06
0.15	"	−2.97	0.52	61	2.63	2.50
0.60	"	−3.04	0.52	60	2.62	2.31
0.90	"	−2.52	0.53	55	2.07	1.90
0	4 weeks	−2.74	0.53	57	2.31	2.06
0.15	"	−2.99	0.55	62	2.85	2.55
0.60	"	−2.66	0.56	60	2.49	2.22
0.90	"	−2.59	0.55	60	2.36	2.13

[a] Concentration of $(Alq_3)_2$-OT in the spin-coated P3HT:PCBM solution.

Table 3 Photovoltaic parameters of the cells doped with $(Alq_3)_2$-OT and Alq_3

Dopant	c_{dopant} (mM)	$J_{sc,best}$ (mA cm^{-2})	$V_{oc,best}$ (V)	FF_{best} (%)	η_{best} (%)	η_{avg} (%)
—	—	−2.67	0.53	63	2.51	2.33
$(Alq_3)_2$-OT	0.57	−2.84	0.56	60	2.69	2.40
Alq_3	1.14	−2.74	0.51	49	2.41	2.12

oligothiophene backbone in $(Alq_3)_2$-OT was compared in solar cells. As shown in Table 3, the use of a relatively high content of free Alq_3 dopant decreases FF and cell efficiency compared to cells doped with equivalent amounts of the complexes bound to $(Alq_3)_2$-OT or without doping. The cell containing $(Alq_3)_2$-OT as a dopant showed highest J_{sc}, V_{oc}, and efficiency. The results clearly demonstrate that the oligothiophene backbone of $(Alq_3)_2$-OT increases the compatibility of Alq_3 with the P3HT:PCBM blend, and $(Alq_3)_2$-OT can be inserted in the BHJ layer as a third component without destroying the layer morphology.

The use $(Alq_3)_2$-OT as a buffer layer was also investigated. $(Alq_3)_2$-OT was thermally vacuum evaporated (185–285 °C) between the photoactive layer and Au anode. Absorption and emission spectra of the evaporated films and the differential scanning calorimetry (DSC) curve of $(Alq_3)_2$-OT are shown in the ESI (S2 and S3†). $(Alq_3)_2$-OT is thermally stable until 400 °C based on the DSC measurement.

The cell parameters were measured one day and four weeks after the cell preparation (Table 4). Meanwhile, the cells were stored in the dark and the ambient atmosphere. The cells with the parent Alq_3 as a buffer layer showed a slight decrease in current and efficiency over the time, whereas the cells equipped with $(Alq_3)_2$-OT as a buffer layer showed improved cell parameters.

Based on the results, it is evident that the used cell structure has a relatively high shelf-lifetime and that $(Alq_3)_2$-OT seems to function better as a hole transporting buffer layer than Alq_3. Also, the remarkable decrease in the series resistance (R_s) implies that $(Alq_3)_2$-OT decreases the intrinsic resistance of the cell when compared to Alq_3.[15]

Energy levels of $(Alq_3)_2$-OT are suitably aligned with those of the other materials used in the cell. The HOMO and LUMO levels of $(Alq_3)_2$-OT are shown together with the energy levels of the inverted cell structure in Fig. 7. The 0.3 eV higher HOMO level of $(Alq_3)_2$-OT compared to that Alq_3 produces smaller extraction barrier for the photogenerated holes to escape the device[6b] when $(Alq_3)_2$-OT is used as a buffer material instead of Alq_3. This may explain the observed reduction of R_s values of the cells with $(Alq_3)_2$-OT as a hole transporting buffer material compared to cells with an Alq_3 buffer layer (Table 4).

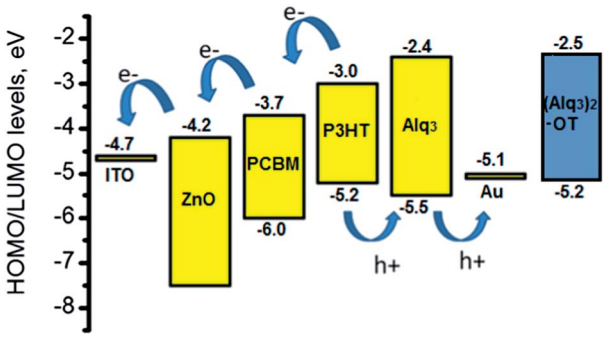

Fig. 7 Energy levels[6,14] of the solar cell structure and HOMO and LUMO levels of $(Alq_3)_2$-OT.

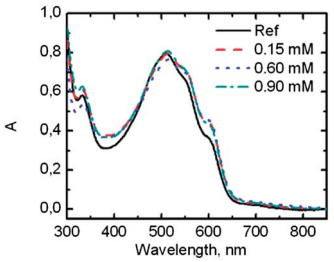

Fig. 8 Absorption spectra of the reference cell without doping and cells with $(Alq_3)_2$-OT as a dopant in the BHJ layer.

The cell absorption spectra in Fig. 8 show that the absorption of the cells is increased in the area around 400 nm, where the absorption of $(Alq_3)_2$-OT takes place. Therefore, more photons are absorbed when $(Alq_3)_2$-OT is used as a dopant. LUMO levels of $(Alq_3)_2$-OT and Alq_3 are nearly the same and higher than the LUMO of PCBM. Therefore, they can donate electron to PCBM. Because $(Alq_3)_2$-OT is capable of donating electrons to PCBM, as shown also by spectroscopic studies, it functions as an additional light-absorber and donates electrons to PCBM which increases the current of the cells. Also, some increase in the cell absorption can be seen as shoulders around 550 nm and 600 nm. This is possibly caused by the improved crystallinity of P3HT due to the inserted dopant molecules, which further supports the high compatibility of $(Alq_3)_2$-OT in the BHJ layer.

Table 4 Photovoltaic parameters and resistances of the cells with Alq_3 or $(Alq_3)_2$-OT buffer layers

Buffer layer (thickness)	Storage time	$J_{sc,best}$ (mA cm^{-2})	$V_{oc,best}$ (V)	FF_{best} (%)	η_{best} (%)	η_{avg} (%)	R_s (Ω cm^2)	R_{sh} (Ω cm^2)
Alq_3 (~5 nm)	One day	−2.62	0.55	60	2.42	2.25	39.64	1499
$(Alq_3)_2$-OT (~6.5 nm)	"	−2.71	0.50	58	2.18	1.93	28.72	1385
$(Alq_3)_2$-OT (~9 nm)	"	−2.84	0.46	54	1.99	1.86	29.19	931
Alq_3 (~5 nm)	4 weeks	−2.54	0.54	61	2.33	2.05	45.12	1998
$(Alq_3)_2$-OT (~6.5 nm)	"	−2.85	0.53	58	2.45	2.22	29.62	1310
$(Alq_3)_2$-OT (~9 nm)	"	−3.11	0.51	56	2.47	2.06	33.43	1494
Alq_3 (~5 nm)	12 weeks	−2.32	0.55	61	2.28	2.03	46.20	2098
$(Alq_3)_2$-OT (~6.5 nm)	"	−2.76	0.52	61	2.54	2.10	29.44	1545
$(Alq_3)_2$-OT (~9 nm)	"	−2.81	0.54	56	2.45	2.13	35.84	2453

Conclusion

Detailed understanding of inter- and intramolecular properties and molecular interactions is a prerequisite for developing new photoactive and functional materials with desired properties. We synthesized an Alq_3 end-capped oligothiophene, $(Alq_3)_2$-OT, and concentrated on understanding its photophysical properties utilizing steady state and time resolved optical spectroscopic methods. When $(Alq_3)_2$-OT was photoexcited, an intramolecular electron transfer from the oligothiophene backbone to the Alq_3 moiety was observed. In the presence of PCBM $(Alq_3)_2$-OT donates electron to PCBM. After these observations $(Alq_3)_2$-OT was applied as a dopant molecule in the P3HT:PCBM active layer of BHJ based organic solar cell, which increased the cell efficiency. Previous reports suggested that the cell efficiency is increased due to improved morphology of the BHJ photoactive layer caused by doping. The current studies strongly support the idea that $(Alq_3)_2$-OT can also function in the BHJ active layer as an additional light-absorber which donates electrons to PCBM and improves the cell efficiency. Moreover, the suitable energy levels allow the use of $(Alq_3)_2$-OT as an interfacial layer between the active layer and gold anode improving the cell performance and shelf-lifetime. These findings provide new insights useful in designing more effective photoactive materials for photovoltaic applications.

Experimental section

Synthesis of the compounds

(8-(Benzyloxy)-5-(4,4,5,5-tetramethyl-1,3,2-dioxaborolan-2-yl)quinolone) and 8-(benzyloxy)-5-bromoquinoline were synthesized using previously published methods.[16]

Compound 2. Commercial starting material **1** (200 mg, 0.40 mmol), NBS (151 mg, 0.85 mmol) and ethyl acetate (7 mL) were placed in a reaction flask. The reaction mixture was irradiated by ultrasound for 1 h.[17] The solvent was evaporated and the product was purified by flash-chromatography (SiO_2, *n*-hexane). Compound **2** was collected as yellow powder (239 mg, 91%). ^{1}H NMR ($CDCl_3$, 300 MHz): δ ppm 0.89 (t, J = 6.60 Hz, 6H), 1.28–1.42 (m, 12H), 1.59–1.67 (m, 4H), 2.72 (t, J = 7.50 Hz, 4H), 6.91 (s, 2H), 6.97 (d, J = 3.93 Hz, 2H), 7.12 (d, J = 3.93 Hz, 2H).

Compound 3. Compound **2** (201 mg, 0.31 mmol), toluene (9 mL), ethanol (3 mL) and distilled water (3 mL) were bubbled with argon for 15 min. K_2CO_3 (181 mg, 1.31 mmol), $Pd(PPh_3)_4$ (44.8 mg, 0.039 mmol) and 3-hexylthiophene-2-boronic acid pinacol ester (0.20 mL, 0.63 mmol) were added and the reaction mixture was refluxed under argon for 5 h. The solvents were evaporated and ethyl acetate (20 mL) was added. The solution was extracted two times with distilled water (6 mL) and the organic layer was dried with $MgSO_4$. The solution was filtered and evaporated to dryness. Flash-chromatography (SiO_2, *n*-hexane) afforded the compound **3** as a yellow reddish oil (246 mg, 97%). ^{1}H NMR ($CDCl_3$, 300 MHz): δ ppm 0.89–0.94 (m, 12H), 1.30–1.45 (m, 24H), 1.62–1.76 (m, 8H), 2.78–2.83 (m, 8H), 6.95 (d, J = 5.20 Hz, 2H), 6.97 (s, 2H), 7.07 (d, J = 3.74 Hz, 2H), 7.16 (d, J = 3.74 Hz, 2H), 7.18 (d, J = 5.20 Hz, 2H).

Compound 4. Compound **4** was prepared using the same method as compound **2**. The specific amounts of chemicals used: compound **3** (170 mg, 0.20 mmol), NBS (76.9 mg, 0.43 mmol) and 4 mL ethyl acetate. Flash-chromatography (SiO_2, *n*-hexane) afforded the compound **4** as a red powder (180 mg, 89%). ^{1}H NMR ($CDCl_3$, 300 MHz): δ ppm 0.88–0.93 (m, 12H), 1.30–1.40 (m, 24H), 1.57–1.73 (m, 8H), 2.70–2.81 (m, 8H), 6.90 (br. s, 4H), 7.05 (d, J = 3.74 Hz, 2H), 7.15 (d, J = 3.74 Hz, 2H).

Compound 5. Method A: Suzuki–Miyaura coupling. Toluene (4.5 mL), ethanol (1.5 mL) and distilled water (1.5 mL) were bubbled with argon for 15 min. Compound **4** (150 mg, 0.15 mmol), 8-(benzyloxy)-5-(4,4,5,5-tetramethyl-1,3,2-dioxaborolan-2-yl)quinoline (109 mg, 0.30 mmol), K_2CO_3 (93.7 mg, 0.68 mmol) and $Pd(PPh_3)_4$ (21.3 mg, 0.018 mmol) were added and the reaction mixture was refluxed under argon for 5 h. The solvents were evaporated and the crude product was dissolved in toluene (15 mL). The solution was transferred to a flash-chromatography column (SiO_2) and eluated with the mixture of EtOAc–*n*-hexane (2 : 1). The solid crude product obtained from column purification was stirred with acetone (3 mL), filtered and washed with acetone (9 mL). The procedure afforded the compound **5** as an orange powder (167 mg, 85%). Method B: direct arylation. Compound **3** (246 mg, 0.30 mmol) was dissolved in DMA (3 mL). The solution was bubbled with argon for 15 min. K_2CO_3 (206 mg, 1.50 mmol), $Pd(OAc)_2$ (6.8 mg, 0.03 mmol), $PCy_3 \cdot HBF_4$ (22.7 mg, 0.06 mmol), pivalic acid (19.4 mg, 0.19 mmol) and 8-(benzyloxy)-5-bromoquinoline (187 mg, 0.60 mmol) were added and the reaction mixture was heated (150 °C) under argon for 24 h. The reaction mixture was filtered through a thin pad of silica gel, the filter washed with chloroform, (*ca.* 20 mL) and the solvents evaporated. The crude product was stirred with acetone (3 mL), filtered and washed with acetone (10 mL) and ethanol (5 mL). The procedure afforded the compound **5** as orange powder (334 mg, 87%). ^{1}H NMR ($CDCl_3$, 300 MHz): δ ppm 0.89–0.94 (m, 12H), 1.34–1.45 (m, 24H), 1.66–1.78 (m, 8H), 2.79–2.88 (m, 8H), 5.51 (s, 4H), 6.98 (s, 2H), 7.01 (s, 2H), 7.05–7.09 (m, 4H), 7.17 (d, J = 3.74 Hz, 2H), 7.32–7.42 (m, 6H), 7.48–7.56 (m, 8H), 8.64 (dd, J = 8.56, 1.71 Hz, 2H), 9.03 (dd, J = 4.20, 1.71 Hz, 2H). ^{13}C NMR ($CDCl_3$, 75 MHz): δ ppm 14.1, 22.6, 22.6, 29.2, 29.3, 29.4, 29.5, 30.5, 30.6, 31.7, 70.7, 109.3, 121.9, 123.9, 124.3, 126.3, 127.0, 127.8, 127.9, 128.2, 128.6, 128.7, 130.2, 130.3, 130.8, 134.0, 134.1, 135.0, 136.7, 136.7, 138.5, 140.0, 140.1, 140.5, 149.4, 154.2. HRMS: calcd for $C_{80}H_{84}N_2O_2S_6Na$ ($[M + Na]^+$) 1319.4755, found 1319.4812.

Compound 6. Compound **5** (100 mg, 0.077 mmol) was dissolved in CH_2Cl_2 (7.5 mL). The reaction system was charged with argon and cooled on ice bath. A 1 M BBr_3 in CH_2Cl_2 solution (1.6 mL, 1.60 mmol) was slowly added. The reaction mixture was stirred at room temperature overnight. The reaction mixture was cooled on ice bath and saturated $NaHCO_3$(aq.) (8 mL) was slowly added. The mixture was evaporated to dryness. Toluene (15 mL) and distilled water (5 mL) were added. The organic layer was dried with Na_2SO_4 and filtered. The filter was washed with a small amount of chloroform and the filtrate was evaporated to dryness. The crude product was stirred with

acetone (1.5 mL), filtered and washed with acetone (6.5 mL). The procedure afforded the compound **6** as dark red powder (65.0 mg, 75%). ^{1}H NMR ($CDCl_3$, 300 MHz): δ ppm 0.89–0.94 (m, 12H), 1.35–1.47 (m, 24H), 1.67–1.77 (m, 8H), 2.80–2.89 (m, 8H), 7.01 (s, 2H), 7.03 (s, 2H), 7.09 (d, J = 3.74 Hz, 2H), 7.18 (d, J = 3.74 Hz, 2H), 7.22 (d, J = 7.90 Hz, 2H), 7.52 (dd, J = 8.60, 4.20 Hz, 2H), 7.61 (d, J = 7.90 Hz, 2H), 8.68 (dd, J = 8.60, 1.56 Hz, 2H), 8.83 (dd, J = 4.20, 1.56 Hz, 2H). ^{13}C NMR ($CDCl_3$, 50 MHz): δ ppm 14.1, 22.6, 22.7, 29.2, 29.3, 29.5, 29.6, 29.7, 30.5, 30.7, 31.7, 109.5, 122.2, 122.7, 123.9, 126.3, 126.8, 128.7, 129.3, 130.0, 130.2, 130.7, 134.0, 134.6, 135.0, 136.7, 138.3, 138.6, 140.0, 140.1, 147.9, 152.3. HRMS: calcd for $C_{66}H_{73}N_2O_2S_6$ ($[M + H]^+$) 1117.3996, found 1117.3999.

$(Alq_3)_2$-OT. Compound **6** (20.0 mg, 0.018 mmol), 8-hydroxyquinoline (10.4 mg, 0.072 mmol), Al(*i*-PrO)$_3$ (7.3 mg, 0.036 mmol), $CHCl_3$ (2 mL) and ethanol (1 mL) were placed in a reaction flask which was charged with argon. The reaction mixture was stirred and refluxed for 17 h. The solvents were evaporated and methanol (5 mL) was added. The precipitate was filtered and washed with acetone (10 mL). The procedure afforded the $(Alq_3)_2$-OT as orange powder (29.3 mg, 94%). ^{1}H NMR ($CDCl_3$, 300 MHz): δ ppm 0.91 (br. s., 12H), 1.33–1.42 (m, 24H), 1.71 (br. s., 8H), 2.78–2.86 (m, 8H), 6.92–6.99 (m, 5H), 7.07–7.17 (m, 13H), 7.34–7.54 (m, 11H), 7.62–7.66 (m, 3H), 8.24–8.32 (m, 4H), 8.76–8.94 (m, 6H). HRMS: calcd for $C_{102}H_{95}N_6O_6Al_2S_6$ ($[M + H]^+$) 1745.5268, found 1745.5266.

$(Alq_3)_2$-OT and PCBM film preparation. All film samples were prepared on quartz plates. The PCBM film was spin-coated for 5 min (600 rpm) from a 14.1 mg mL^{-1} DCB solution. The film of $(Alq_3)_2$-OT was drop-cast from 400 μL of 0.40 mg mL^{-1} $(Alq_3)_2$-OT chloroform solution. The film of $(Alq_3)_2$-OT with 2.5 m% PCBM was drop cast from 400 μL of a mixed 0.40 mg mL^{-1} $(Alq_3)_2$-OT and 0.01 mg mL^{-1} PCBM chloroform solution. The film of $(Alq_3)_2$-OT with 5 m% PCBM was drop cast from 400 μL of a mixed 0.40 mg mL^{-1} $(Alq_3)_2$-OT and 0.02 mg mL^{-1} PCBM chloroform solution. The film of $(Alq_3)_2$-OT with 9 m-% of PCBM was drop cast from a 0.40 mg mL^{-1} $(Alq_3)_2$-OT and 0.04 mg mL^{-1} PCBM chloroform solution.

Spectroscopic measurements. The steady state absorption and fluorescence were measured employing a UV-3600 Shimadzu UV-VIS-NIR spectrophotometer and a Jobin Yvon-SPEX fluorolog. The fluorescence lifetimes were measured using a time correlated single photon counting (TCSPC) system equipped with a Picoharp 300 controller and a PDL 800-B driver for excitation and a microchannel plate photomultiplier (Hamamatsu R3809U-50) for detection in 90° configuration. The excitation wavelengths were 405 nm and 483 nm and pulse frequency 2.5 MHz. Pump-probe technique for time resolved absorption was used to detect the fast processes with a time resolution shorter than 0.2 ps. The instrument and the used data analysis procedure have been reported earlier.[18]

Solar cell preparation. The solvents and Alq_3 (99.995%) were purchased from Sigma-Aldrich and used without further purification. The solar cell samples were prepared on ITO coated glass substrates (1.2 cm × 3.5 cm) purchased from Solems. The zinc-acetate ($Zn(OCOCH_3)_2 \cdot 2H_2O$) for ZnO layer preparation was purchased from Sigma-Aldrich. Reference polymer, P3HT, was purchased from Rieke Metals and acceptor $PC_{60}BM$ (99.0%) from Nano-C.

Solar cells were constructed on commercial ITO covered glass substrates. The ITO layer was taped and lacquered for *aqua regia* etching to achieve a patterned ITO. The etched plates were cleaned by sonicating in acetone, chloroform, SDS solution (20 mg sodium dodecyl sulphate in 500 mL Milli-Q H_2O), Milli-Q H_2O and 2-propanol (30 min in each), in the previously stated order, and dried under vacuum at 150 °C for one hour. After a 10 min N_2 plasma cleaning procedure (Harrick Plasma Cleaner PDG-236), a 20 nm ZnO layer was deposited by 1 min spin-coating in WS-400B-6NPP/LITE spin-coater from Laurell Technologies from 50 g L^{-1} zinc-acetate in 96% 2-methoxyethanol and 4% ethanolamine solution following the literature process.[19]

The photoactive layer compounds, P3HT, $PC_{60}BM$ and dopant, were dissolved in 1,2-dichlorobenzene : chloroform (2 : 1 V%) mixture and stirred (250 rpm) overnight at 50 °C. Spin-coating of the BHJ photoactive layer from the P3HT:PCBM:dopant blend took 5 minutes (600 rpm) in the spin-coater under N_2 flow. The spin-coated films were annealed under vacuum at 110 °C for 10 min. Buffer layer and Au anode were evaporated in the vacuum evaporator under ~3 × 10^{-6} mbar pressure. The evaporation rate and film thickness were controlled with evaporator crystals to deposit the desired thickness of the buffer and ~50 nm thick Au anode layers on top of the photoactive layer. The cells were stored in the ambient atmosphere in the dark before measurements and analysis.

The photovoltaic parameters were obtained and calculated from current–voltage (*I–V*) curves, which were measured in the dark and under simulated AM 1.5 sunlight illumination (50 mW cm^{-2}) using an Agilent E5272A source/monitoring unit. A voltage of −0.20 V–0.60 V was applied in 10 mV steps. The measurements were carried out in ambient atmosphere at room temperature without encapsulation of the devices. The illumination was produced by a filtered Xe-lamp (Oriel Corporation & Lasertek) in the Zuzchem LZC-SSL solar simulator. The illumination power density was measured using a Coherent Fieldmax II LM10 power meter. Because a certified measuring system could not be employed, the absolute efficiency values are not directly comparable with the other published results. However, the reported efficiencies and the relative efficiency changes are comparable within the presented devices.

To determine the thickness of the evaporated buffer layers, reference quartz plates were placed into the evaporator chamber for each buffer evaporation. A narrow strip of the reference film was removed with a cotton stick dipped in $CHCl_3$ and the step was measured with a Veeco Wyko NT-1100 profilometer. The profilometer data were recorded from (230 × 300) μm^2 and analyzed by phase shift interferometry (PSI) mode. The vertical resolution of this method is close to 1 Å according to the instrument manual and the horizontal resolution of the objective (20 × magnification) is 0.75 μm.

Electrochemical measurements. Differential pulse voltammetry (DPV) measurements were carried out by employing an Iviumstat (Compactstat IEC 61326 Standard) potentiostat and a three-electrode cell configuration to determine HOMO and

LUMO energy levels for compound **5** and $(Alq_3)_2$-OT. The measurements were carried out using 0.1 M $TBAPF_6$ in dichloromethane (DCM) as supporting electrolyte, glass platinum electrode as working electrode, graphite rod as counter electrode and platinum wire as pseudo reference electrode. For each sample, the background was measured for 2.5 mL of the electrolyte solution after 20 min deoxygenation purging N_2. 100 μL of 0.5 mM sample in DCM was inserted and the system was stabilized again purging N_2. Each sample was measured between −2.5 V and 2.0 V scanning in both directions with 2.5 mV steps. Ferrocene (Acros Organics, 98%) was used as internal standard reference to scale the measured potentials against vacuum level.[20] HOMO and LUMO level calculations were based on the formal oxidation and reduction potentials observed in the DPV curves according to the following equations:

$$E_{\mathrm{HOMO}} = -(4.8 + E_{\mathrm{dif,ox}})\mathrm{eV}$$

$$E_{\mathrm{LUMO}} = -(-E_{\mathrm{dif,red}} + 4.8)\mathrm{eV}$$

where 4.8 eV is the oxidation energy of ferrocene. $E_{\mathrm{dif,ox}}$ is the difference in volts between the formal oxidation potentials of ferrocene and the measured sample. $E_{\mathrm{dif,red}}$ is the difference in volts between the formal oxidation potential of ferrocene and the formal reduction potential of the sample. See the HOMO and LUMO level calculations in ESI p. 19 and 20.†

Author contributions

O.E.O.H. and H.J.L. act as group leaders. J.P.H. synthesized and characterized all the compounds. V.M.M. carried out spectroscopic and electrochemical studies and solar cell experiments. K.M.K. helped with the fittings and analysis of the pump-probe measurements. All authors took part in the writing of the manuscript.

Acknowledgements

The National Doctoral Programme in Nanoscience (NGS-NANO) is greatly acknowledged for funding. Tero-Petri Ruoko is acknowledged for helping with the pump-probe measurements.

Notes and references

1 (*a*) B. Walker, A. B. Tamayo, X.-D. Dang, P. Zalar, J. H. Seo, A. Garcia, M. Tantiwiwat and T.-Q. Nguyen, *Adv. Funct. Mater.*, 2009, **19**, 3063; (*b*) A. B. Tamayo, X.-D. Dang, B. Walker, J. Seo, T. Kent and T.-Q. Nguyen, *Appl. Phys. Lett.*, 2009, **94**, 103301; (*c*) M. S. Wrackmeyer, M. Hein, A. Petrich, J. Meiss, M. Hummert, M. K. Riede and K. Leo, *Sol. Energy Mater. Sol. Cells*, 2011, **95**, 3171; (*d*) R. Fitzner, C. Elschner, M. Weil, C. Uhrich, C. Körner, M. Riede, K. Leo, M. Pfeiffer, E. Reinold, E. Mena-Osteritz and P. Bäuerle, *Adv. Mater.*, 2012, **24**, 675.

2 Y. Ooyama and Y. Harima, *Eur. J. Org. Chem.*, 2009, 2903.

3 C. W. Tang and S. A. VanSlyke, *Appl. Phys. Lett.*, 1987, **51**, 913.

4 (*a*) A. Fuchs, D. Steinbrecher, M. S. Mommer, Y. Nagata, M. Elstner and C. Lennarts, *Phys. Chem. Chem. Phys.*, 2012, **14**, 4259; (*b*) S. Barth, P. Müller, H. Riel, P. F. Seidler, W. Riess, H. Vestweber and H. Bässler, *J. Appl. Phys.*, 2001, **89**, 3711.

5 Q. L. Song, F. Y. Li, H. Yang, H. R. Wu, X. Z. Wang, W. Zhou, J. M. Zhao, X. M. Ding, C. H. Huang and X. Y. Hou, *Chem. Phys. Lett.*, 2005, **416**, 42.

6 (*a*) A. Tolkki, K. Kaunisto, J. P. Heiskanen, W. A. E. Omar, K. Huttunen, S. Lehtimäki, O. E. O. Hormi and H. Lemmetyinen, *Thin Solid Films*, 2012, **520**, 4475; (*b*) V. M. Manninen, W. A. E. Omar, J. P. Heiskanen, H. Lemmetyinen and O. E. O. Hormi, *J. Mater. Chem.*, 2012, **22**, 22971.

7 (*a*) H. Kanato, K. Takimiya, T. Otsubo, Y. Aso, T. Nakamura, Y. Araki and O. Ito, *J. Org. Chem.*, 2004, **69**, 7183; (*b*) N. Kiriy, A. Kiriy, V. Bocharova, M. Stamm, S. Richter, M. Plötner, W.-J. Fischer, F. C. Krebs, I. Senkovska and H.-J. Adler, *Chem. Mater.*, 2004, **16**, 4757; (*c*) C.-H. Chen, K.-Y. Liu, S. Sudhakar, T.-S. Lim, W. Fann, C.-P. Hsu and T.-Y. Luh, *J. Phys. Chem. B*, 2005, **109**, 17887; (*d*) A. Saeki, T. Fukumatsu and S. Seki, *Macromolecules*, 2011, **44**, 3416; (*e*) R. Stalder, D. Xie, R. Zhou, J. Xue, J. R. Reynolds and K. S. Schanze, *Chem. Mater.*, 2012, **24**, 3143.

8 P. Arsenyan, E. Paegle and S. Belyakov, *Tetrahedron Lett.*, 2010, **51**, 205.

9 (*a*) G. D. Zhu, D.-H. Chen, J.-H. Huang and C.-S. Chi, *J. Org. Chem.*, 1992, **57**, 2316; (*b*) M. V. Adhikari and S. D. Samant, *Ultrason. Sonochem.*, 2002, **9**, 107; (*c*) G. A. Heropoulos, G. Cravotto, C. G. Screttas and B. R. Steele, *Tetrahedron Lett.*, 2007, **48**, 3247.

10 (*a*) D. J. Schipper and K. Fagnou, *Chem. Mater.*, 2011, **23**, 1594; (*b*) C. B. Bheeter, J. K. Bera and H. Doucet, *RSC Adv.*, 2012, **2**, 7197; (*c*) F. Derridj, K. S. Larbi, J. Roger, S. Djebbar and H. Doucet, *Tetrahedron*, 2012, **68**, 7463; (*d*) S. Bensaid and H. Doucet, *Tetrahedron*, 2012, **68**, 7655; (*e*) H. Zhao, C. Y. Liu, S. C. Luo, B. Zhu, T.-H. Wang, H.-F. Hsu and H.-H. Yu, *Macromolecules*, 2012, **45**, 7783; (*f*) K. Yamazaki, J. Kuwabara and T. Kanbara, *Macromol. Rapid Commun.*, 2013, **34**, 69; (*g*) G. Trippé-Allard and J.-C. Lacroix, *Tetrahedron*, 2013, **69**, 861.

11 R. A. J. Janssen, M. P. T. Christiaans, K. Pakbaz, D. Moses, J. C. Hummelen and N. S. Saricifti, *J. Chem. Phys.*, 1995, **102**, 2628.

12 C. Ganzorig and M. Fujihira, *Appl. Phys. Lett.*, 2002, **81**, 3137.

13 (*a*) S. Watanabe, A. Furube and R. Katoh, *J. Phys. Chem. A*, 2006, **110**, 10173; (*b*) S. Watanabe, M. Murai, Y. Tamaki, A. Furube and R. Katoh, *Prog. Int. Symp. Super-Functionality Organic Devises: IPAP Conf. Series*, 2005, vol. 6, p. 121.

14 (*a*) HOMO and LUMO levels of P3HT and $PC_{60}BM$: A. K. K. Kyaw, *et al.*, *Appl. Phys. Lett.*, 2008, **93**, 221107; (*b*) Energy levels of ZnO: S. S. Zade, *et al.*, *Acc. Chem. Res.*, 2011, **44**, 14.

15 M.-S. Kim, B.-G. Kim and J. Kim, *ACS Appl. Mater. Interfaces*, 2009, **1**, 1264.

16 V. A. Montes, R. Pohl, J. Shinar and P. Anzenbacher Jr, *Chem. – Eur. J.*, 2006, **12**, 4523.

17 Branson 2510 ultrasonic bath was used as an irradiation source.
18 N. V. Tkachenko, L. Rantala, A. Y. Tauber, J. Helaja, P. H. Hynninen and H. J. Lemmetyinen, *J. Am. Chem. Soc.*, 1999, **121**, 9378.
19 M. S. White, D. C. Olson, S. E. Shaheen, N. Kopidakis and D. S. Ginley, *Appl. Phys. Lett.*, 2006, **89**, 143517.
20 R. R. Gagne, C. A. Koval and G. C. Lisensky, *Inorg. Chem.*, 1980, **19**, 2854.

Tampereen teknillinen yliopisto
PL 527
33101 Tampere

Tampere University of Technology
P.O.B. 527
FI-33101 Tampere, Finland

ISBN 978-952-15-3293-1
ISSN 1459-2045